NON-REACTING SPRAY CHARACTERISTICS OF ALTERNATIVE AVIATION FUELS AT GAS TURBINE ENGINE CONDITIONS

by

Dongyun Shin

A Dissertation

Submitted to the Faculty of Purdue University

In Partial Fulfillment of the Requirements for the degree of

Doctor of Philosophy

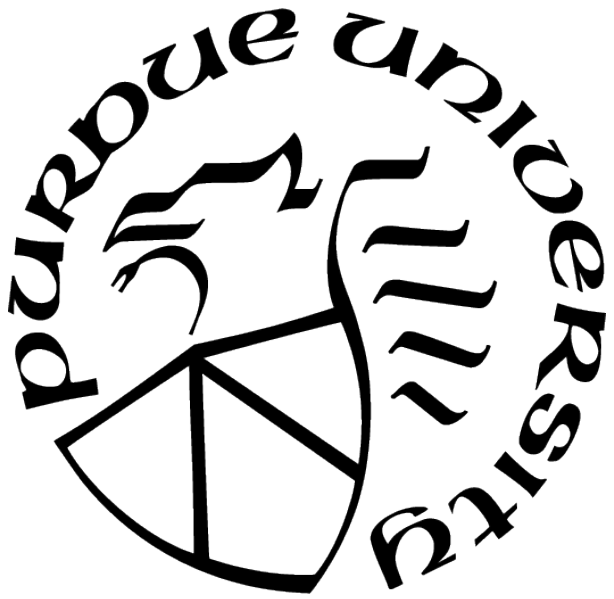

School of Aeronautics and Astronautics

West Lafayette, Indiana

May 2021

THE PURDUE UNIVERSITY GRADUATE SCHOOL
STATEMENT OF COMMITTEE APPROVAL

Dr. Robert P. Lucht, Co-Chair

School of Mechanical Engineering

Dr. Veeraraghava R. Hasti, Co-Chair

School of Mechanical Engineering

Dr. Jay P. Gore, Committee

School of Mechanical Engineering

Dr. Paul E. Sojka, Committee

School of Mechanical Engineering

Dr. Carson D. Slabaugh, Committee

School of Aeronautics and Astronautics

Approved by:

Dr. William A. Crossley

Head of the School Graduate Program

ACKNOWLEDGMENTS

This research was funded by the U.S. Federal Aviation Administration Office of Environment and Energy through ASCENT, the FAA Center of Excellence for Alternative Jet Fuels and the Environment, Project 29A through FAA Award Number 13-C-AJFE-PU-011 under the supervision of Dr. Cecilia Shaw and Dr. Anna Oldani. Any opinions, findings, conclusions or recommendations expressed in this material are those of the author and do not necessarily reflect the views of the FAA. The test matrix used for lean blowout conditions and engine cold start conditions were provided courtesy of project consultant Dr. Nader Rizk. I would like to thank Dr. Tim Edwards for providing the fuels and information about their physical properties.

I like to thank all Zucrow staff members, Scott Meyer, Rob McGuire, Toby Lamb, Michelle Moody, Chad Meltzer, and Dr. Rohan Gejji. And I also thank all HPL colleagues.

Contents

LIST OF TABLES

LIST OF FIGURES

ABSTRACT

The aviation industry is continuously growing amid tight restrictions on global emission reductions. Alternative aviation fuels have gained attention and developed to replace the conventional petroleum-derived aviation fuels. The replacement of conventional fuels with alternative fuels, which are composed solely of hydrocarbons (non-petroleum), can mitigate impacts on the environment and diversify the energy supply, potentially reducing fuel costs. To ensure the performance of alternative fuels, extensive laboratory and full-scale engine testings are required, thereby a lengthy and expensive process. The National Jet Fuel Combustion Program (NJFCP) proposed a plan to reduce this certification process time and the cost dramatically by implementing a computational model in the process, which can be replaced with some of the testings. This requires an understanding of the influence of chemical/physical properties of alternative fuels on combustion performance. The main objective of this work is to investigate the spray characteristics of alternative aviation fuels compared to that of conventional aviation fuels, which have been characterized by different physical liquid properties at different gas turbine-relevant conditions.

The experimental work focuses on the spray characteristics of standard and alternative aviation fuels at three operating conditions such as near lean blowout (LBO), cold engine start, and high ambient pressure conditions. The spray generated by a hybrid pressure-swirl airblast atomizer was investigated by measuring the drop size and drop velocity at a different axial distance downstream of the injector using a phase Doppler anemometry (PDA) measurement system. This provided an approximate trajectory of the largest droplet as it traveled down from the injector. At LBO conditions, the trend of decreasing drop size and increasing drop velocity with an increase in gas pressure drop was observed for both conventional (A-2) and alternative aviation fuels (C-1, C-5, C-7, and C-8), while the effect of fuel injection pressure on the mean drop size and drop velocity was observed to be limited. Moreover, the high-speed shadowgraph images were also taken to investigate the effect of the pressure drop and fuel injection pressures on the cone angles. Their effects were found to be limited on the cone angle.

The spray characteristics of standard (A-2 and A-3) and alternative (C-3) fuels were investigated at engine cold-start conditions. At such a crucial condition, sufficient atomization needs to be maintained to operate the engine properly. The effect of fuel properties, especially the viscosity, was investigated on spray drop size and drop velocity using both conventional and alternative aviation fuels. The effect of fuel viscosity was found to be minimal and dominated by the effect of the surface tension, even though it showed a weak trend of increasing drop size with increasing surface tension. The higher swirler pressure drop reduced the drop size and increased drop velocity due to greater inertial force of the gas for both conventional and alternative aviation fuels at the cold start condition. However, the effect of pressure drop was observed to be reduced at cold start condition compared to the results from the LBO condition.

The final aspect of experimental work focuses on the effect of ambient pressures on the spray characteristics for both conventional (A-2) and alternative (C-5) aviation fuels. Advanced aviation technology, especially in turbomachinery, has resulted in a greater pressure ratio in the compressor; therefore, greater pressure in combustors for better thermal efficiency. The effect of ambient pressure on drop size, drop velocity, and spray cone angle was investigated using the PDA system and simultaneous Planar Laser-Induced Fluorescence (PLIF) and Mie scattering measurement. A significant reduction in mean drop size was observed with increasing ambient pressure, up to 5 bar. However, the reduction in the mean drop size was found to be limited with a further increase in the ambient pressure. The effect of the pressure drop across the swirler was observed to be significant at ambient pressure of 5 bar. The spray cone angle estimation at near the swirler exit and at 25.4 mm downstream from the swirler exit plane using instantaneous Mie images was found to be independent of ambient pressure. However, the cone angle at measurement plane of 18 mm in the spray was observed to increase with increasing ambient pressure due to entrainment of smaller droplets at higher ambient pressure. Furthermore, the fuel droplet and vapor distribution in the spray were imaged and identified by comparing instantaneous PLIF and Mie images.

Lastly, a semi-empirical model was also developed using a phenomenological three-step approach for the atomization process of the hybrid pressure-swirl airblast atomizer. This model includes three sub-models: pressure-swirl spray droplet formation, droplet impinge-

ment, and film formation, and aerodynamic breakup. The model predicted drop sizes as a function of ALR, atomizing gas velocity, surface tension, density, and ligament length and diameter and successfully demonstrated the drop size trend observed with fuel viscosity, surface tension, pressure drop, and ambient pressure. The model provided insights into the effect of fuel properties and engine operating parameters on the drop size. More experimental work is required to validate the model over a wider range of operating conditions and physical fuel properties.

Overall, this work provides valuable information to increase understanding of the spray characteristics of conventional and alternative aviation fuels at various engine operating conditions. This work can provide valuable data for developing an advanced computational combustor model, ultimately expediting the certification of new alternative aviation fuels.

1. INTRODUCTION

1.1 Background and Motivation

Control and reduction of global pollutant emissions from the aircraft have been a topic of significant interest over the last few decades. The Federal Aviation Administration (FAA) Air Traffic Organization announced that more than 44,000 flights and 2.7 million airline passengers are crossing the United States airspace every day. This number was continuously growing at approximately 4.7 % annually, until the pandemic of 2020 (COVID-19), as shown in Fig. 1.1. Although the number of worldwide air passenger dropped down to 60 % in 2020 compared to those numbers in 2019 [**icao2020**] due to COVID-19, International Air Transport Association has projected that the number of air passenger to grow up to 8.2 billion by 2037 [**garcia2018**]. This number is twice larger than the number in 2019. Therefore, the dependence of the aviation industry solely on petroleum-derived fuels can exacerbate global emissions, which causes climate change and poor air quality. Aviation industry has committed to carbon- growth in international commercial aviation beginning in 2020, as shown in Fig. 1.2 [**icao2019**]. The amount of net CO_2 that can be reduced by using alternative aviation fuels is significant and indispensable to accomplish the carbon-neutral growth.

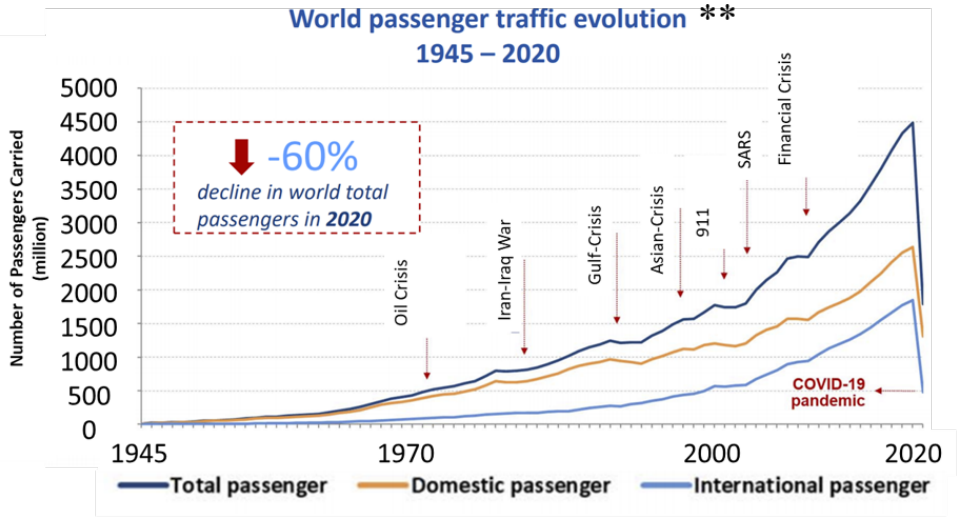

Figure1.1. World passenger traffic evolution 1945-2020 [**icao2020**].

Benefits of alternative aviation fuels include mitigating impacts on the environment and diversifying the energy supply, thereby improving market flexibility [**hileman2014**]. To maximize these benefits, critical requirements for such alternative fuels include seamless integration without engine redesign and incorporation without new infrastructure on the ground or in flight. More importantly, the performance of alternative fuels must be comparable to conventional aviation fuels for commercial use. Furthermore, their physical and chemical properties and performance in combustion need to be carefully examined.

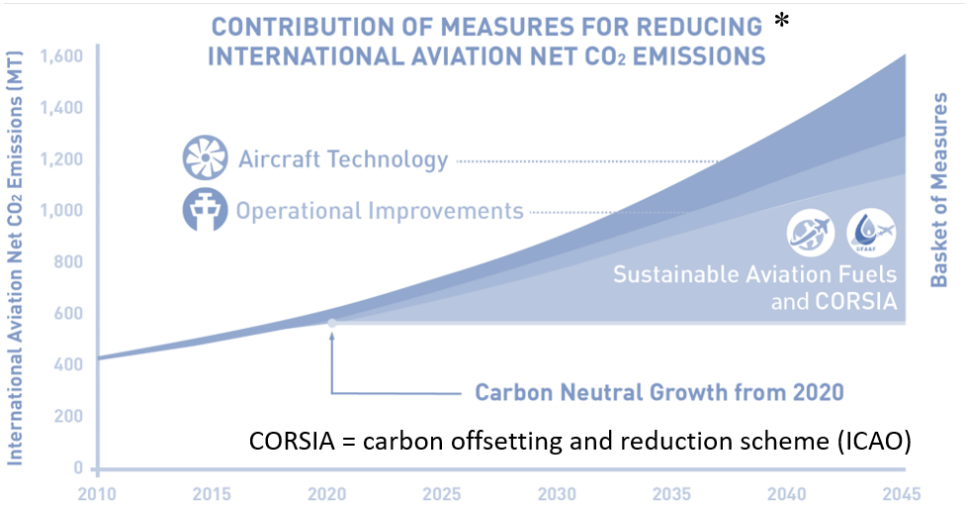

Figure1.2. Contribution of measures for reducing international aviation net CO_2 emissions [**icao2019**].

1.1.1 National Jet Fuel Combustion Program

The National Jet Fuel Combustion Program (NJFCP) was initiated to investigate the influence of alternative aviation fuel properties on combustion performance, aiming to develop an advanced combustion model that can be implemented in the fuel qualification process and to dramatically reduce the approval time and the cost. The present work is highly coordinated within the NJFCP and funded by the Federal Aviation Administration (FAA) under the Aviation Sustainability Center (ASCENT) of Excellence for Alternative Jet Fuels and Environment. The major focus of this work is to characterize the spray of the conventional and alternative fuels experimentally at relevant gas turbine engine conditions. These

experimental data are essential in the qualification process for the alternative aviation fuels and valuable for model validation in the program.

Commercial deployment of any specific alternative jet fuel relies on the approval and issuance of a specification by ASTM International and every candidate fuel needs to go through the D4054 qualification process [**colket2017**]. The ASTM D4054 is an iterative and rigorous process, and extensive testing of fuel samples is required to measure their physical properties, chemical composition, and performance. As shown in Fig. 1.3, newly developed fuels must satisfy the basic specification properties with regards to engine safety in Tier 1 In Tier 2, some laboratory tests are required to obtain their chemical and physical properties, ground handling safety, and compatibility with other fuels. The candidate fuels that satisfy the requirements from Tier 1 and 2 will go through combustor rig and component testing, and if necessary, full-scale engine testing in Tier 3 and 4. These testing results will be reported and reviewed by the original equipment manufacturer (OEM) and the FAA. If additional tests and measurements are required, then the processes of Tier 3 and 4 need to be iterated. The total testing costs for the D4054 qualification process have not been published, but it is estimated to be in $3 - 4 million range over a 3 - 5 year period [**colket2017**]. This estimate does not account for the cost of supplying a large amount of test fuel that could range from 76,000 L up to 380,000 L [**colket2017**].

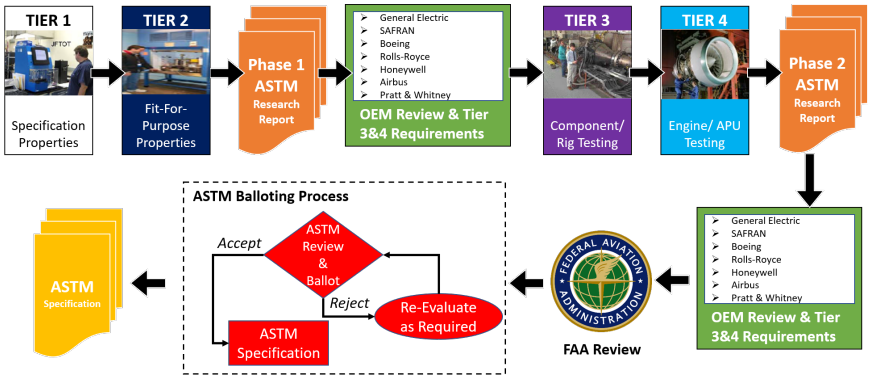

Figure1.3. Schematic describing the ASTM D4054 qualification process [**colket2017**].

Figure 1.4 shows the vision of the NJFCP and the interaction between research groups and OEMs in the qualification process. The six major research areas interact with each

other, and the results from each area are essential to developing an advanced combustion model in Area 4. As shown in Fig. 1.4, the six major areas include chemical kinetics combustion experiments, chemical kinetics model development, advanced combustion experiments, combustion model development, atomization experiments and modeling, and combustor rig evaluation. High fidelity testing of alternative fuels is required for each research area. Especially for Area 5 and 6, it is important to evaluate the performance of alternative fuels at relevant gas turbine engine conditions such as near lean blowout, cold start, and high altitude re-light.

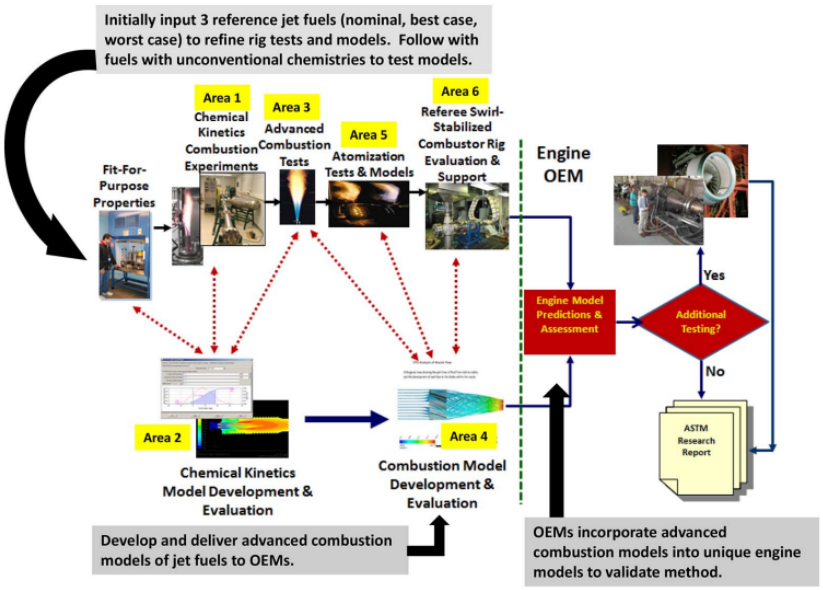

Figure1.4. Schematic of the interaction between research groups and original equipment engine manufacturers (OEMs) [**colket2017**].

The present work is part of Area 5 and focuses on the evaluation of the spray characteristics at these conditions. Atomization is an important factor in the combustion process because the atomization quality strongly affects the performance of the combustor. Insufficient atomization produces larger droplets, leading to the formation of soot and nitric oxides due to fuel-rich combustion [**lefebvre1989**]. On the other hand, sufficient atomization produces many small droplets, leading to a greater volumetric heat release rate, easier light-up, a wider burning range, and lower pollutant emissions [**lefebvre1989**].

1.2 Research Objectives

This work aims to investigate the spray characteristics of conventional and alternative aviation fuels at realistic gas turbine engine conditions and the effect of physical fuel properties and operating conditions on the spray. The sprays generated by a hybrid pressure-swirl airblast atomizer are investigated under three relevant gas turbine engine conditions: near lean blowout, cold start, and high ambient pressure.

The modern aircraft is operated at fuel lean conditions to reduce the amount of pollutant emission, leading to a near lean blowout (LBO). Under this condition, a perturbation of flow through the engine may cause flame extinction, and the ability to restart the engine becomes a major safety concern. At LBO, the spray characteristics such as mean drop size, drop velocity, and cone angle are investigated using a phase Doppler anemometry (PDA) system for candidate alternative (C-1, C-5, C-7, C-8) fuels and compared to a conventional (Jet-A) fuel spray. Details of the alternative aviation fuels can be found in Chapter 3. The effects of fuel properties, pressure drops, and fuel injection pressures on spray characteristics such as mean drop size and axial drop velocity are investigated. These spray characterizations are essential in developing a combustion model and validation.

At cold start conditions, the viscosity, and surface tension of the fuel become important factors in determining spray quality. The spray of alternative fuel C-3, which is characterized as a high viscosity fuel, is investigated and compared to the sprays of Jet-A and JP-5, measuring their mean drop sizes and drop velocities using PDA. The mean drop sizes and drop velocities of each fuel spray are compared to determine the effects of fuel properties such as viscosity and surface tension. In addition, the effect of pressure drop across the gas swirler on the mean drop sizes and velocities is investigated.

The ambient gas in the combustor can be varied widely in pressure and temperature depending on engine operability and can strongly affect the fuel atomization. The pressure in combustors has been raised continuously in recent years due to advanced technology in a search for better thermal efficiency, even exceeding the critical pressure of the liquid fuel **boyce2011**. Higher pressure in combustion results in increasing thermal efficiency by improving the specific fuel consumption. The effect of ambient pressure on spray characteristics

is investigated using PDA, Planar Laser Induced Fluorescence (PLIF) and Mie imaging for conventional (Jet-A) and alternative (C-5) fuels. The PDA, a point measurement technique, is used to measure the mean drop sizes and mean axial drop velocities at various ambient pressures, while the fuel-PLIF/Mie imaging is used to obtain the 2-D images of the spray.

A phenomenological three-step atomization model (semi-empirical) for the hybrid pressure-swirl airblast atomizer was developed and used to provide some insights into the effect of fuel properties and the engine operating parameters on the drop size by comparing the predicted and measured D_{32}. The dependence of D_{32} on fuel properties, air-to-liquid ratio, and ambient pressure are demonstrated by the model and compared to the observed trends in experimental results.

1.3 Summary of Thesis Dissertation

This thesis dissertation is divided into eight chapters. The first chapter introduces the background and motivation of this research and defines overall objectives. The second chapter includes a review of various spray applications in different areas, mainly focusing on the gas turbine engine combustion application. The importance of the spray in combustion applications and atomization mechanisms for different atomizer types are introduced. The fundamentals of the spray characteristic parameters and various diagnostic techniques in characterizing the spray are also discussed in the second chapter. The third chapter provides a methodology of semi-empirical model for HSPA atomizer. Chapter Four provides the investigation of the spray characteristics at near lean blowout conditions for Jet-A and four different alternative fuel candidates (C-1, C-5, C-7, C-8) using PDA. The effect of fuel properties, pressure drops, and fuel injection pressures on the mean drop sizes and drop velocities are discussed along with the results of a numerical model. Chapter Five focuses on the spray characteristics at cold start engine conditions for Jet-A, JP-5, and C-3, alternative fuel. The effect of fuel properties and pressure drops on the mean drop size and drop velocity measured by PDA is investigated. The sixth chapter discusses the effect of high ambient pressures on the spray characteristics at similar fuel and gas temperatures for near LBO conditions for Jet-A and C-5 fuels. Two-dimensional representations of the spray measured

by simultaneous PLIF and Mie imaging are presented and discussed in Chapter Six. Chapter Seven briefly discusses some of potential work that can be done in near future. Finally, the eighth chapter summarizes the key findings from Chapters 3 through 6.

2. SPRAY AND ATOMIZATION

This chapter provides a brief introduction to the spray in gas turbine engine combustion applications, with a primary focus on the spray process for a hybrid pressure-swirl airblast atomizer. The important measurement parameters in characterizing the spray and some of the measurement techniques are also discussed.

2.1 Background

2.1.1 Spray Application

Spray phenomena in fluid dynamics is a complicated and challenging subject. Nevertheless, sprays can be encountered everywhere in modern life due to their practical importance. The applications of sprays can be diverse depending on the specific need. For instance, the spray drying technique is being widely used in the pharmaceutical industry to produce polymer nanoparticles, which are being used as responsive drug delivery systems. The spray drying technique involves the atomization of a solvent into very fine droplets within a hot drying gas leading the solvent droplets to evaporate and precipitate into solid particles. In agriculture, sprayers are widely used on farms to sprays herbicides, pesticides, water, fungicides, and defoliants for means of crop quality control.

The spray combustion in internal combustion engines and gas turbine engines are also one of the largest applications of liquid sprays. Spray combustion is being widely used in engines of automobiles, ships, and aircraft. In such cases, the liquid fuel is injected at high pressure through a narrow orifice into a combustion chamber, where turbulent, swirling, and recirculating streams of reacting gases are present at high temperature and pressure conditions. The injected fuel is then disintegrated into fine droplets, which can be quickly evaporated, and eventually burned. In such combustion application, according to Lefebvre [**lefebvre1989**], the combustion of liquid fuel in gas turbines is dependent on effective atomization to increase the specific surface area of the fuel and thereby achieve high rates of mixing and evaporation. In addition, the reduction in the fuel drop size leads to a higher volumetric heat release rate, easier light-up, a wider burning range, and lower

exhaust concentrations of pollutant emissions. On the other hand, insufficient atomization produces larger droplets, which can lead to the formation of soot and nitric oxides due to fuel-rich combustion [**lefebvre1989**].

Hence, it is important to investigate the spray characteristics to understand the combustion process, which can be greatly affected by the atomization quality. Because of the random nature of the atomization process, many different factors can be considered to control the atomization quality, such as atomizer geometry, operating conditions for the combustor, and liquid physical properties,

2.2 Atomizer Designs

The spray can be produced in various ways with different atomization processes. The methods of atomization are generally determined by the type of atomizer for each application. For gas turbine combustion applications, airblast, pressure swirl, and hybrid atomizers are being widely used due to their atomization capabilities for gas turbine combustion. A conventional airblast atomizer uses an air stream at high velocity to atomize the liquid injected through the orifice [**lefebvre1989**]. Airblast atomizers provide a good atomization quality and wide spray angles with high-velocity air flowing, resulting in less soot formation in combustion. The disadvantages of airblast atomizers are their narrow stability limits and poor atomization at engine start-up due to lower air velocity. These drawbacks of airblast atomizer can be overcome by combining it with a pressure swirl atomizer, which has a swirl chamber that directs liquid through a single orifice at high pressure and provides sufficient atomization over a wide range of liquid flow rates. It is well known for easy engine start-up, although its spray angle is sensitive to the fuel injection pressure and the surrounding gas pressure. The hybrid airblast atomizer has some of the advantages of both atomizers and allows more flexible operability at start-up, cruise, maximum power conditions, etc. [**mansour2003**]. A detailed discussion for each type of atomizer is provided in this section.

2.2.1 Pressure Swirl Atomizer

Pressure-swirl atomizers are one of the simplest mechanical pressure atomizers. They produce a hollow cone spray and are widely used in rocket and gas turbine applications [**lefebvre1989**]. The pressure-swirl atomizer injects the fuel through tangential passages into a swirl chamber, as shown in Fig 2.1. The number of fuel ports can be varied depending on the design variation of the atomizer. The injected fuel develops a thin and rapid swirling fuel film along the inner surface of the chamber, which contracts towards the single orifice. Due to angular momentum conservation, the tangential and axial flow velocity of the fuel film increase as it flows towards the nozzle exit. These velocity components emerge into a thin conical sheet at the nozzle exit and disintegrate the conical sheet into ligaments to form drops due to instability. These atomizers have advantages at start-up and have a large operation stability range [**lefebvre1989**].

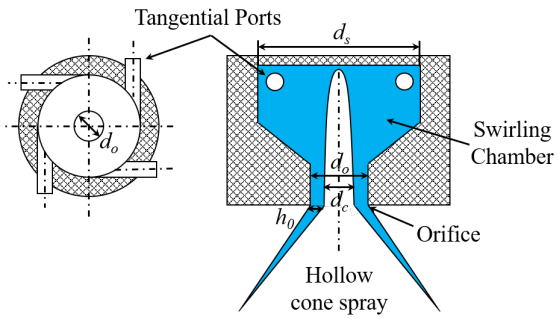

Figure2.1. Flow path in pressure swirler [**lefebvre1989**]

2.2.2 Airblast Atomizer

The airblast atomizers employ two separate airflows to disintegrate the fuel sheet into ligaments, and then drops. Figure 2.2 shows the design of the prefilming airblast atomizer. The central circular passage contains a swirler, which causes the airflow to be deflected radially outward to strike the inner surface of the fuel flow. Another airstream flows through an annular passage containing a swirler. The swirling motion of the airflow interacts with the outer surface of the fuel sheet and leads to atomization. The airblast atomizer usually

employ a large amount of air, and thus, it is ideal in continuous-flow combustion systems [**lefebvre1989**]. Furthermore, low soot formation and a blue flame of low luminosity can be achieved because of the thorough fuel and air mixing process from the airblast atomizers. The primary disadvantages of the airblast atomizers are their narrow stability limits and poor atomization quality at start-up due to the low velocity of the air streams.

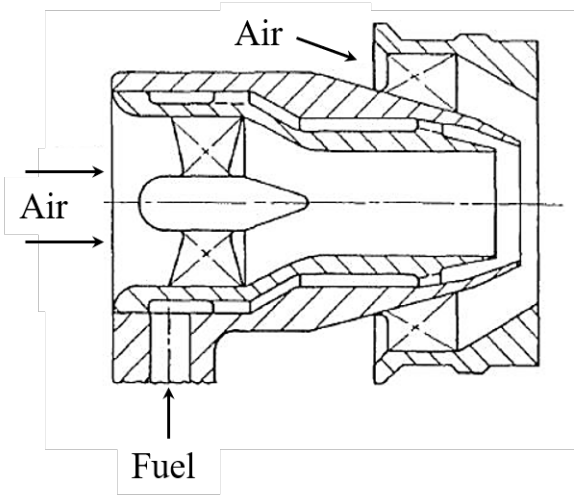

Figure2.2. Prefilming airblast atomizer design (Courtesy of Parker Hannifin Corp.)[**lefebvre1989**]

2.2.3 Hybrid Pressure-Swirl Airblast Atomizer (HPSA)

The advantages of both airblast and pressure-swirl atomizers are combined into one to overcome drawbacks from each type of atomizer. This is called a hybrid airblast atomizer, which was used in this research to produce the spray. The hybrid airblast atomizer has two fuel injection circuits: the main and the pilot. The pilot injector uses the pressure-swirl atomizer mechanism, in which fuel is directed out through the central orifice, resulting in a hollow cone spray. The fuel spray then interacts with two air swirl flows provided from the air swirler assembly surrounding the primary nozzle portion. The air co-flow through each swirler, which has a number of helical or angled vanes, results in co-rotating air flows. These air swirl flows promote the breakup of the fuel into ligaments then quickly into droplets. The mechanism that is introduced in the swirler assembly defines the airblast [**mansour2003**].

Although the hybrid atomizers can overcome the drawbacks from the airblast and pressure-swirl atomizers, the complexity of the design becomes a concern. Also, the weight of the atomizer increases. Figure 2.3 shows a diagram of the hybrid pressure-swirl airblast atomizer manufactured by Parker Hannifin. The atomizer consisted of a prime injector and a gas swirler that housed the injector. The prime injector has two different orifice sets: the pilot and the main. The pilot consisted of a single pressure-swirl orifice on the centerline of the injector. On the other hand, the main consisted of five orifices oriented radially outward from the injector centerline, which employs the airblast atomization mechanism. For the present work, only the pilot fuel nozzle was utilized.

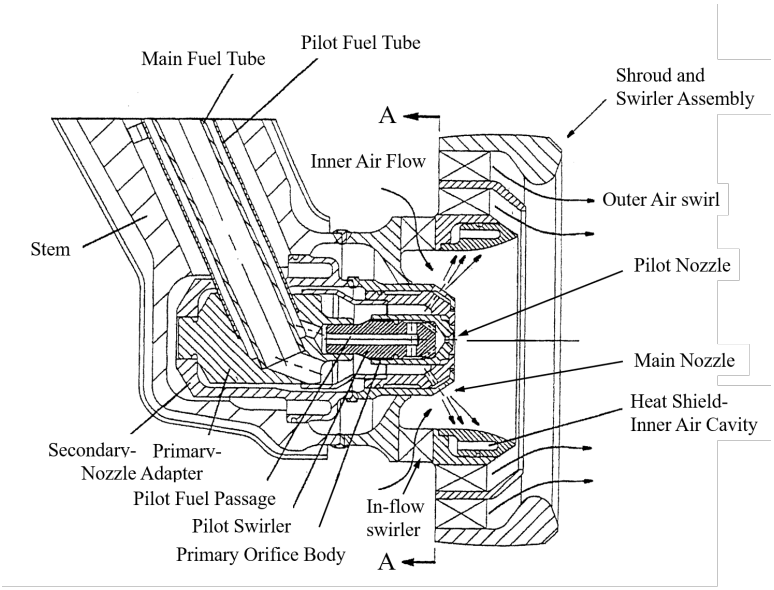

Figure2.3. Breakup mechanism for hybrid atomizer [**mansour2003**]

2.3 Spray Characteristics

2.3.1 Representative Diameters and Drop velocity

Droplet sizes usually determine the atomization quality. Sufficient atomization quality produces many small droplets, leading to a greater volumetric heat release rate, easier light-up, a wider burning range, and lower pollutant emission [**lefebvre1989**]. On the other hand, insufficient atomization produces larger droplets, leading to formation of soot and

nitric oxides due to fuel-rich combustion [**lefebvre1989**]. Therefore, the drop size is one of the key parameters that need to be quantified in spray characterization.

Representative diameters typically used to characterize sprays in gas turbine engine application are the arithmetic mean diameter (D_{10}), Sauter mean diameter (D_{32}), and mass median diameter (MMD). The arithmetic mean diameter is a first-order mean drop diameter in the spray and is commonly used for general comparison. The Sauter mean diameter represents the ratio of the volume to the surface area and is used in mass transfer and gas turbine combustion applications. The mass median diameter is defined as the diameter that represents 50% of total liquid volume within the smaller drop diameters. MMD is commonly used to describe the spray for combustion applications where mass transfer and drop volumes are significant. The parameter f_0 in Eq.5.1 represents the number probability density function, and the parameter f_3 is the volume probability density of a drop that has a volume of $\frac{\pi D^3}{6}$ [**lefebvre1989**]. The mathematical expressions for these mean diameters and probability density functions are:

$$D_{10} = \frac{\Sigma N_\mathrm{i} D_\mathrm{i}}{\Sigma N_\mathrm{i}} \tag{2.1}$$

$$D_{32} = \frac{\Sigma N_\mathrm{i} D_\mathrm{i}^3}{\Sigma N_\mathrm{i} D_\mathrm{i}^2} \tag{2.2}$$

$$f_0(D) = \frac{N_\mathrm{i}}{\Sigma N_\mathrm{i} \Delta D_\mathrm{i}} \tag{2.3}$$

$$f_3(D) = \frac{f_0(D) D^3}{\int_0^\infty f_0(D) D^3 dD} \tag{2.4}$$

$$0.5 = \int_0^{MMD} f_3(D) dD \tag{2.5}$$

In Eq.3.1 - 5.3, N_i is the number of drops, and D_i is the drop diameter.

The measured D_{32} values at several radial locations for z = 25.4 mm were used to calculate a single value of line-of-sight drop size (D_{32}o) at that measurement plane. The line-of-sight drop size (D_{32o}) can be obtained via:

$$D_{32o} = \frac{\sum_1^n D_{32}(r)q(r)}{\sum q(r)} \tag{2.6}$$

Here, r is the radial location from the spray center, and n is the number of radial locations. $D_{32}(r)$ and $q(r)$ are the measured D_{32} and fuel mass flux at each radial location respectively. The PDA system provides a local fuel volume flux at each measurement point by measuring the number of droplets passing through the probe volume. This line-of-sight drop size was calculated and used to demonstrate an overall drop size trend with fuel properties and operating conditions.

Drop velocity is an important parameter that needs to be quantified in sprays along with drop size since it affects the mass dispersion within the combustor and the droplet evaporation. Furthermore, the growth of droplet instability, which is directly related to secondary breakup and atomization quality, is also affected by drop velocity [**lefebvre1989**]. In the present study, only the axial component of droplet velocity (U_z) was measured by the 1-D PDA system. Thus, the mean axial drop velocity was used in spray characterization.

2.3.2 Influence of Engine Operating Parameters on Spray Characteristics

Different atomization quality can be obtained depending on engine operating parameters such as air-to-liquid ratio (ALR), fuel injection pressure, and ambient pressure and temperature. For airblast atomizers, Batarseh *et al.* [**batarseh2010**] reported that the mean drop size decreased with increasing airflow rates through the swirler of the atomizer, while the effect of varying liquid flow rates was observed to be limited. Chin *et al.* [**chin2000**], on the other hand, observed that the mean drop size increased when liquid injection pressure was increased using a prefilming airblast atomizer. This is believed to be due to the accumulation of the liquid film on the prefilming surface caused by the higher fuel flow rate. The effect of liquid injection pressure on the spray angle was reported to be insignificant [**ma2014**].

The air-to-liquid ratio (ALR) is an important operating parameter for the airblast atomizer since it is highly related to the combustion process [**lefebvre1989**]. The pressure drop across the swirler is the key parameter of interest in the present study since it changes the ALR by controlling the air flow rate through the swirler. Batarseh *et al.* [**batarseh2010**] observed smaller drop sizes with increasing airflow rates through the swirler using a prefiliming airblast atomizer. Higher swirler pressure drop resulted in higher kinetic energy in the gas flow, which can transfer to the droplets and cause further disintegration. This trend of decreasing drop size with increasing ALR, controlled through the pressure drop across the swirler, was also observed by Chin *et al.* [**chin2000**], Custer *et al.* [**custer1988**], and Rizkalla *et al.* [**rizkalla1975**]. Also, these studies noted that the effect of swirler pressure drop on drop size was diminished with a further increase in the swirler pressure drop.

The ambient pressure of the combustor is another parameter that usually varies depending on the engine operability. Batarseh *et al.* [**batarseh2010**] and Chrigui *et al.* [**chrigui2010**] observed that the mean drop size was reduced significantly with increasing ambient pressure from 1 to 5 bar. However, further increases in ambient pressure increased the mean drop size. A similar trend was observed by Zheng *et al.* [**zheng1996**] with increasing the ambient pressure, but the variation in drop size was found to be small. Zheng *et al.* [**zheng1996**] noted that the atomization process in a counter swirling airblast atomizer is dominated by the liquid sheet breakup mechanism and is independent of ambient pressure. In contrast, other studies [**becker2004**, **cober2018**, **chaussonnet2019**, **jasuja1981**] observed that the mean drop size decreased continuously with increasing ambient pressures. However, further increasing the ambient pressure diminished the variation in mean drop size. Zheng *et al.* [**zheng1996**] reported a widening spray cone angle near the nozzle with increasing ambient pressure from 1 bar to 12 bar; however, the cone angle further downstream of the spray remained fairly constant.

The drop velocity was found to be insensitive to the liquid injection pressure [**ma2014**]. Instead, the pressure drop across the swirler had a significant effect on the drop velocity. Higher pressure drop increased the amount of momentum in a gas flow that can transfer to the droplets, and this resulted in increased drop velocity [**chin1999**,**ma2014**]. The drop

axial velocity was reported to be decreased continuously with increasing ambient pressure [**zheng1996**, **batarseh2010**,**chrigui2010**].

2.3.3 Influence of Liquid Properties on Spray Characteristics

Flow and spray characteristics are strongly affected by liquid physical properties such as viscosity, surface tension, and density. Rizkalla *et al.* [**rizkalla1975**] , Custer *et al.* [**custer1988**] , and Tareq *et al.* [**tareq2020**] observed larger droplet formation with increasing liquid-gas surface tension and liquid viscosity using an airblast atomizer. Rizk *et al.* [**rizk1980**, **rizk1984**] also observed an increase in drop size and liquid film thickness on the prefilming surface with increasing viscosity. However, Custer *et al.* [**custer1988**] found that the effect of viscosity on drop size was observed to be less significant at higher ALRs for the airblast atomizer. Wang and Lefebvre [**wang1987**] concluded that the primary liquid physical properties that affect the drop size are surface tension and viscosity from extensive measurements performed with both pressure-swirl and airblast atomizers.

A narrower cone angle was reported with higher liquid viscosity for the airblast atomizer due to the viscous forces reducing the swirling motion of the liquid sheet [**custer1988**, **chen1992**]. Chen *et al.* [**chen1992**] noted that this viscous effect was most pronounced at the highest liquid viscosity. An increase in surface tension was also found to produce narrower cone angles by Tareq *et al.* [**tareq2020**].

2.3.4 Dimensionless Numbers for Spray Characterization

Two dimensionless parameters become significant when characterizing the spray in terms of aerodynamic forces and liquid properties: the Weber number (We) and the Ohnesorger number (Oh). The Weber number We represents the ratio of the inertia forces to surface tension forces and can be expressed as [**lefebvre1989**]:

$$We = \frac{\rho_g U_{rel}^2 D_0}{\sigma} \tag{2.7}$$

Here, ρ_g indicates the gas density, U_{rel} indicates the relative velocity between gas and liquid, and σ is the surface tension. The parameter D_0 is a length-scale such as an orifice diameter of the pilot nozzle in the present study. The Weber number equation includes the dynamic pressure term in nominator and the surface tension in the denominator. A higher We indicates that the kinetic energy tends to dominate over the surface tension force for a bulk liquid or drop. A lower We indicates that the surface tension force (or restorative force) dominates on a bulk liquid or drop. The surface tension force multiplied by the liquid surface area is the minimum energy required for atomization. Therefore, the Weber number becomes a useful dimensionless parameter when the surface tension forces are important.

The Ohnesorger number Oh represents the ratio of viscous forces to inertial and surface tension forces and can be expressed as [**lefebvre1989**]:

$$Oh = \frac{\mu_l}{\sqrt{\rho_l D_0 \sigma}} \tag{2.8}$$

where μ_l is the liquid dynamic viscosity, and ρ_l indicates the liquid density. It can be seen that the Oh number includes only the liquid properties and independent of any aerodynamic parameters. A greater Oh indicates that a bulk liquid or drop has a lower tendency towards fragmentation due to higher viscous forces, while lower Oh indicates a lower friction loss caused by the viscous forces.

2.3.5 Alternative Aviation Fuels

The "drop-in fuels" are composed solely of hydrocarbons but produced from alternative sources such as biomass [**edwards2017**]. Based on an earlier program [**edwards2010**], the NJFCP has developed the test fuels to span the range of jet fuel composition and properties that could be encountered with conventional and alternative jet fuels. The developed fuels were being acquired and distributed by the Air Force Research Laboratory's (AFRL) Fuels Branch in Dayton, Ohio. Many of the alternative jet fuels developed in the program have been approved by ASTM D7566 for use as 50% blends (or less) with conventional fuels [**edwards2017**]. The NJFCP had defined categories of fuels to be used to characterize the fuel effect on combustion. The fuels categorized by A indicate conventional fuels derived

from petroleum, encompassing a typical range of properties such as viscosity, flash point, aromatic content, etc. [**colket2017**] . The fuels categorized by C indicate test fuels designed to explore the "edges" of the jet fuel composition-property, which their property specification limit and composition were outside of typical experience. Some of these C fuels satisfy the specification for a jet-fuel and can be considered fuels. However, they are unusual and outside the range of experience [**colket2017**].

3. THEORETICAL APPROACH

A theoretical model was developed for this hybrid pressure-swirl airblast (HPSA) atomizer spray to explore the influence of fuel properties and operating conditions on the drop diameter. The model captures the atomization process through three different sub-models: pressure-swirl spray droplet formation, droplet impingement and film formation, and aerodynamic breakup. Figure 3.1 shows the schematic diagram of the atomization process of the hybrid pressure-swirl airblast atomizer. The spray from the pressure-swirl component impinges on the prefilming surface to form a fuel film, which flows along the surface and extends from the prefilmer tip to form ligaments. The ligaments are exposed to the swirling gas flow and disintegrated into droplets.

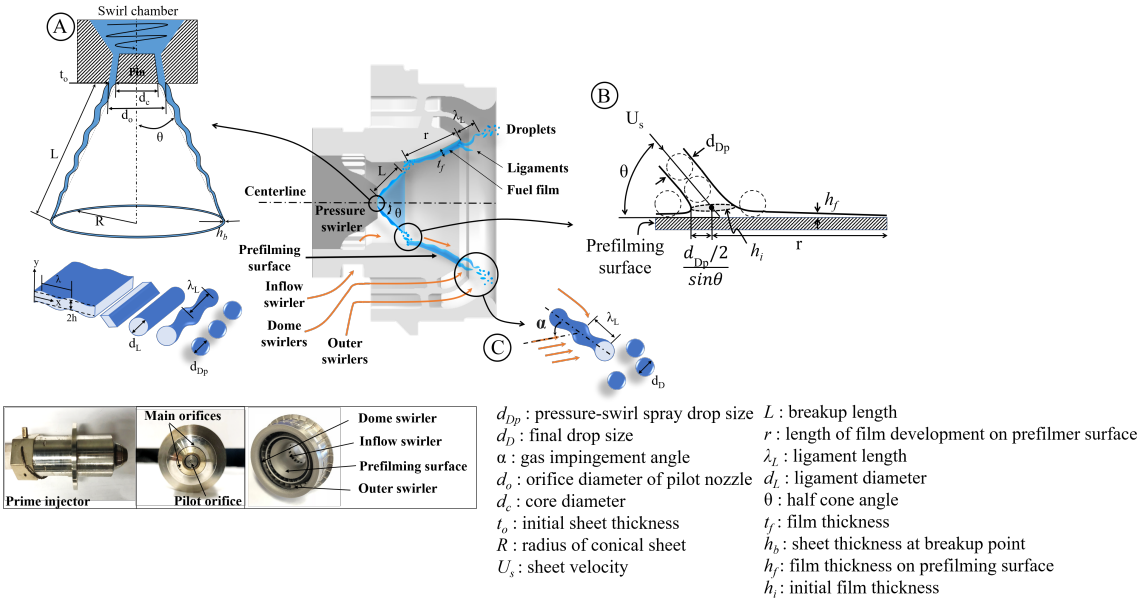

Figure3.1. Schematic diagram of atomization process and photograph for the hybrid pressure-swirl airblast atomizer

3.1 Atomization Process of HSPA Atomizer

Atomization is a process of converting bulk liquids into small droplets. Essentially, atomization results from a disruption of the influence of surface tension by the internal and external forces. Surface tension acts as a restorative force and tends to pull the liquid into

the spherical droplet in the absence of any disruptive forces. Viscosity resists agitation in the liquid and tends to prevent its breakup, resulting in larger droplet sizes. The aerodynamic forces acting on the liquid surface promote the disruption process in the bulk liquid. When this disruptive force exceeds the restorative and resistive forces of the liquid due to the surface tension and viscosity, the bulk liquids start to break into large droplets or ligaments. This initial breakup is referred to as primary atomization. Many larger droplets or ligaments resulting from the primary atomization are unstable, thereby undergoing further breakup into smaller droplets. This process is referred to as secondary atomization.

The atomization process using only the pilot nozzle for the HSPA atomizer in this study can be described as the following steps: (1) the hollow cone spray generated from the pilot nozzle, which uses the pressure-swirler mechanism, impinges on the prefilming surface, (2) the impinged spray then forms a liquid film as it spreads out on the surface by the inner swirl gas flow, and the film flows towards the prefilimer tip, (3) ligaments are formed as the fuel film extends from the prefilmer tip, (4) ligaments then interact with the outer swirling gas flows and are disintegrated into droplets, (5) some of unstable larger droplets and droplets shattered by the swirling gas flow undergo secondary breakup and form smaller droplets. At each step, different breakup mechanisms for the liquid jet, sheet, and droplets can be considered. This section of the chapter primarily focuses on different breakup mechanisms involved in each step of the atomization process for the HSPA atomizer.

3.1.1 Pressure-Swirl Spray Drop Formation

A sub-model for the pressure-swirl spray drop formation from the pilot nozzle was developed to predict the liquid sheet thickness and initial drop size resulting from sheet breakup. For the pilot nozzle used in the present study, the atomization process begins inside the swirling chamber of the injector, where the swirling motion of the liquid is generated against the chamber wall. The fuel then exits through the annular passage made between the center core diameter (d_c) and orifice diameter (d_o) to form a fuel film as shown in the Fig. 3.1A. As the fuel film exits the pilot nozzle, it extends into a thin conical sheet that rapidly attenuates as it spreads radially outward. For the pilot nozzle in the present study, the width of the

fuel passage in the nozzle port is assumed to be constant [**das2008**], since the core diameter (d_c) is geometrically fixed. If the fuel passage is assumed to be completely filled, the film thickness at the exit of the pilot nozzle (t_0) can be calculated as

$$t_0 = \frac{d_o}{2} - \frac{d_c}{2} \tag{3.1}$$

The correlation of cone angle for the pressure-swirl spray suggested by Dodge and Biaglow [**dodge1986**] was adopted to implement the cone angle variation caused by high ambient pressure. If the cone angle decreases due to high ambient pressure, the spray impact point on the prefiming surface will be further away from the pilot nozzle. This will reduced the length of film development on the surface (r), as defined in Fig. 3.1, and may result in forming relatively thicker film at the prefilmer tip. The correlation for the cone angle suggested by Dodge and Biaglow [**dodge1986**] can be expressed as

$$2\theta = 79.8 - 0.918\frac{\rho_g}{\rho_{go}} \tag{3.2}$$

where ρ_g is the gas density, and ρ_{go} is the gas density at 298 K and 1 bar. The parameter θ indicates the half cone angle. In this correlation, the gas density is the controlling parameter for cone angle.

A linear sheet instability analysis was performed to predict the breakup process of the conical sheet produced by the pressure-swirler. The liquid physical properties such as liquid viscosity, surface tension, and density are accounted for in the analysis, as well as the effect of surrounding gas, which is assumed to be incompressible and inviscid. Detailed information regarding the theoretical approach for the sheet instability model can be found in Senecal *et al.* [**senecal1999**] and is only briefly discussed in the present study. The dispersion relation between the growth rate ω_s of disturbance on the sheet and the sheet wavenumber k_s was developed and simplified by Senecal *et al.* [**senecal1999**] and can be expressed as

$$\omega_s = -2\nu_l k_s^2 + \sqrt{4\nu_l^2 k_s^4 + QU_R^2 k_s^2 - \frac{\sigma k_s^3}{\rho_l}} \tag{3.3}$$

The parameter U_R is the relative velocity between the liquid and gas, and Q is the ratio of gas density to liquid density (ρ_g/ρ_l). The maximum growth rate of the disturbance on the conical liquid sheet ($\omega_{s_1,max}$) generated by the pilot nozzle and the sheet wavenumber ($k_{s_1,max}$) at the maximum growth rate can be calculated by solving Eq.5.1 numerically. The relative velocity can be obtained between the conical sheet and the inner swirling gas flow (U_{R_1}). The conical sheet generated by the pilot nozzle was assumed to be a short sinuous wave since the density ratio (Q) is significantly less than unity [**senecal1999**], and a critical gas Weber number ($We_g = \rho_g U_{R_1}^2 h/\sigma$) is larger than 27/16, where h is the half sheet thickness [**senecal1999**, **squire1953**]. The parameter ν_l is the kinematic viscosity of liquid and is accounted in order to accurately predict the growth rate for the short wave case [**senecal1999**].

The liquid sheet disintegration occurs when the amplitude of wave on the surface becomes its maximum [**senecal1999**, **dombrowski1963**]. When the disturbance on the sheet reaches its maximum, the sheet starts to break off into fragments, and the fragments contract to form cylindrical ligaments [**dombrowski1963**]. The ligament then breaks into drops as it reaches its critical amplitude of unstable waves caused by the capillary forces. For the ligament formation prediction, it is necessary to calculate the sheet breakup time and length. The analogy of sheet breakup length prediction for cylindrical jets [**reitz1982**] can be used to obtain the sheet breakup time. If the initial amplitude of surface disturbance reaches the wave amplitude at breakup, a sheet breakup time can be determined using the maximum growth rate of the sheet ($\omega_{s_1,max}$) obtained from Eq.5.1 [**senecal1999**, **dombrowskihooper1962**]. The sheet breakup length (L) can then be calculated using the breakup time and absolute liquid sheet velocity (U_{s1}) and expressed as

$$L = |U_{s1}|\tau = \frac{|U_{s1}|}{\omega_{s_1,max}} \ln\left(\frac{\eta_b}{\eta_0}\right) \tag{3.4}$$

where η_0 and η_b are the wave amplitude at initial and at breakup respectively. The quantity $\ln(\eta_b/\eta_0)$, which can be experimentally determined, was given the value of 12 by Dombrowski and Hooper [**dombrowskihooper1962**]. Using the breakup length (L), the sheet thickness

at the breakup point (h_b) can be evaluated based on a conservation of mass by following similar approach used in Moon *et al.* [**moon2010**].

$$h_b = \frac{t_0(d_0 - t_0)}{d_0 - t_0 + 2L\sin(\theta)} \tag{3.5}$$

Here, d_0 is the orifice diameter, and θ is the drop impingement angle of the conical sheet at the pilot nozzle. For the case of short wave growth, ligaments are assumed to be formed from tears in the sheet once per wavelength [**senecal1999**]. Based on the mass balance, the resulting ligament diameter (d_{L_1}) can be obtained by

$$d_{L_1} = \sqrt{\frac{16h_b}{k_{s_1,max}}} \tag{3.6}$$

The ligaments resulted from the sheet breakup are assumed to be oriented transversely to the sheet flow direction. By assuming the inner swirling gas is in mostly axial direction and ignoring radial direction of the flow, the Weber's instability analysis was adopted to predict the growth rate of the disturbance on the ligament and corresponding wavenumber. The dispersion relation for the Weber's instability can be expressed as [**weber1931**]

$$\omega_{ss}^2 + \frac{3\mu_l}{\rho_l}k_L^2\omega_{ss} = \frac{\sigma}{2\rho_l r_L}(1 - k^2 r_L^2)k^2 \tag{3.7}$$

where ω_{ss} is the growth rate of the disturbance on the ligament, r_L is the ligament radius ($d_{L_1}/2$), and k_L is the ligament wavenumber. μ_l, ρ_l, and σ indicate the liquid dynamic viscosity, liquid density, and surface tension, respectively. By solving the Eq.3.7 numerically, the maximum growth rate of the ligament ($\omega_{ss_1,max}$) and the ligament wavenumber ($k_{L_{1,max}}$) that occurs at that maximum growth rate of the ligament can be obtained.

One droplet is assumed to be formed for each wavelength of the ligament when the amplitude of the most unstable wave reaches the ligament radius [**dombrowski1963**]. The resulted droplet diameter (d_{Dp}) from the ligament breakup can be determined using a mass balance:

$$d_{Dp}^3 = \frac{3\pi d_{L_1}^2}{k_{L_1,max}} \tag{3.8}$$

3.1.2 Droplet Impingement and Liquid Film Formation

The droplet resulting from the pressure-swirl spray (d_{Dp}) impinges on the prefilming surface. In this sub-model, the continuous stream of closely-spaced droplets is assumed to behave like a liquid jet for the impingement process. Hence, the empirical jet impingement models developed by Naber *et al.* [**naber1988**] and Ibrahim *et al.* [**ibrahim1991**] were adopted for this sub-model.

During the impingement process, the droplet may undergo spread, rebound, and splash regimes [**stanton1996**]. However, only the spread mechanism was considered by neglecting others for the simplicity of the analysis. In this present work, only the final expression for the film thickness resulted on the prefilming surface is provided. Detailed derivations can be found in Naber *et al.* [**naber1988**] and Ibrahim *et al.* [**ibrahim1991**].

Figure 3.2 shows the impinging model of closely-spaced droplets on the surface, which is adapted and modified the models from Naber *et al.* [**naber1988**] and Hasson *et al.* [**hasson1964**]. The inviscid impinging jet model by Ibrahim *et al.* [**ibrahim1991**] provides an expression for the sheet thickness generated by two impinging liquid jets. One half of this calculated sheet thickness can be assumed to be the film thickness resulted from the droplet impingement. Hence, by following an approach used Ibrahim *et al.* [**ibrahim1991**], the initial film thickness at the impingement point can be expressed as

$$h_{\mathrm{i}} = \left(\frac{d_{Dp}}{2} \frac{\beta \sin\theta}{2(\mathrm{e}^{\beta} - 1)} \right) \mathrm{e}^{\beta(1-\phi/\pi)} \tag{3.9}$$

Assuming inviscid flow, the liquid flowing out between ϕ and $\phi + d\phi$ is proportional to the film thickness since the liquid velocity does not change along streamline [**naber1988**]. Therefore, the film velocity is assumed to be the same as the velocity of the droplets impinging on the surface. Applying these assumptions, the parameter β can be determined based on the conservation of mass and momentum as discussed in Naber *et al.* [**naber1988**]. Equation 3.9 took account factor of 1/2 in the formula.

The film thickness (h_f) at any radial position r and angular position ϕ can be obtained via [**ibrahim1991**]:

$$h_f = h_{\mathrm{i}} \left(\frac{(d_{Dp}/2)}{\sin\theta} \right) \frac{1}{r}, \qquad \text{where } r \geq \frac{d_{Dp}/2}{\sin\theta} \tag{3.10}$$

This expression assumes that the initial film thickness formed at the stagnation point decreases as it flows towards the prefilmer tip. The value of h_f is used as the film thickness formed at location r on the prefilming surface. It should be noted that the shortest distance for r is the radius of ellipse in major axis ($(d_{Dp}/2)/\sin\theta$) at where the initial film thickness h_{i} is defined as shown in Fig. 3.2. The distance r can be obtained from the prefilmer geometry and the spray cone angle θ calculated from Eq.3.2. The film thickness when $\phi = 0$ was considered in this sub-model.

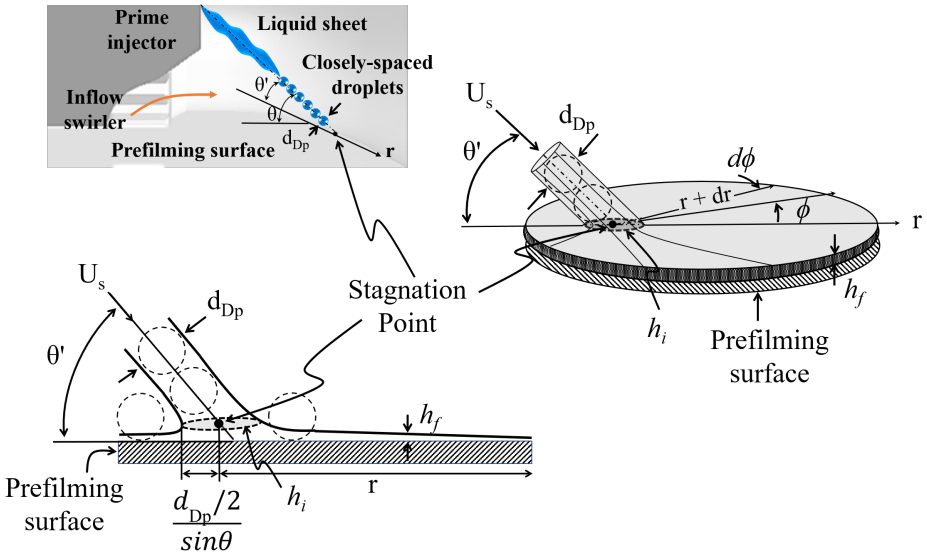

Figure3.2. Sheet formation by impinging droplets on prefilming surface. Adapted and modified models from work of Naber *et al.* [**naber1988**] and Hasson *et al.* [**hasson1964**]

3.1.3 Aerodynamic Breakup

The liquid film developed on the prefilming surface extends from the prefilmer tip and is torn to form ligaments. Using the film thickness h_f obtained from Eq.3.10, it can be

determined whether the film is in the short wave or long wave regime by evaluating the gas Weber number ($We_g > 27/16$) [**senecal1999**]. For the short wave growth, the maximum growth rate of the film ($\omega_{s_2,max}$) and the disturbance wavenumber ($k_{s_2,max}$) on the film at the maximum growth rate can be calculated by solving Eq.5.1 numerically. The relative velocity in this case would be the velocity difference between the film flowing on the surface and inner swirling gas flow along the prefilmer surface (U_{R_2}). The diameter of the ligament (d_{L_2}) resulted from the film breakup at the prefilmer tip can be calculated by

$$d_{L_2} = \sqrt{\frac{16h_f}{k_{s_2,max}}} \tag{3.11}$$

These ligaments were observed to be oriented in the gas flow direction as soon as they were torn off from the film [**sforzo2019**]. Therefore, the Sterling and Sleicher instability analysis [**sterling1975**] was considered in order to account the aerodynamic effect on the ligament breakup. The dispersion relation by Sterling and Sleicher [**sterling1975**] predicts the wavelength of the fastest growing disturbance in a capillary jet and accounts for aerodynamic interaction between the liquid jet and surrounding gas. The Sterling and Sleicher dispersion relation can be expressed as

$$\omega_{ss}^2 + \frac{3\mu_l\xi^2}{\rho_l r_L^2}\omega_{ss} = \frac{\sigma}{2\rho_l r_L^3}(1-\xi^2)\xi^2 + \frac{U_R\rho_g\xi^3 K_0(\xi)}{2r_L^2\rho_l K_1(\xi)}, \quad \text{where } \xi = k_L r_L \tag{3.12}$$

where ω_{ss} is the growth rate of the disturbance on the ligament, r_L is the ligament radius ($d_{L_2}/2$), and k_L is the ligament wavenumber. μ_l, ρ_l, σ, and ρ_g indicate the liquid dynamic viscosity, liquid density, surface tension, and gas density, respectively. By solving the Eq.3.12 numerically, the maximum growth rate of the ligament ($\omega_{ss_2,max}$) and the ligament wavenumber ($k_{L_{2,max}}$) that occurs at that maximum growth rate of the ligament can be obtained. $K_0(\xi)$ and $K_1(\xi)$ are the modified Bessel functions of the first kind and the second kind respectively.

The resulting ligaments then interact directly with the atomizing gas flow from the dome and outer swirlers of the HSPA atomizer. The impingement angle of the atomizing gas flow to the ligament axis was not parallel but rather at a certain angle (α) due to the geometry

of swirler passage in the atomizer. This gas impingement angle (α) was estimated to be approximately 65° from observations made by X-ray imaging [**sforzo2019**]. Due to such a high impinging angle of the gas flow, the prompt atomization mechanism suggested by Lefebvre [**lefebvre1992**] and Beck *et al.* [**beck1991**] was adopted to predict the drop size from the ligament disintegration by the atomizing gas flow. Similar energy consideration as discussed by Lefebvre [**lefebvre1992**] was adopted assuming that the energy required to atomize a ligament is equal to some fraction of the kinetic energy of the atomizing gas. Thus, the energy balance can be expressed as

$$\frac{C\dot{m}_g U_g^2}{2} = \frac{6\sigma\dot{m}_l}{\rho_l d_D} - \frac{4\sigma\dot{m}_l}{\rho_l}\left(\frac{1}{d_{L_2}} + \frac{1}{2\lambda_{L_2}}\right) \tag{3.13}$$

Here, $\dot{m}_g$ and $\dot{m}_l$ indicate the mass flow rates for the gas and liquid respectively. U_g is the swirling gas velocity, and λ_{L_2} is the ligament length which can be calculated from the ligament wavenumber ($\lambda_{L_2} = 2\pi/k_{L_2,max}$). The parameter d_D would be the drop diameter resulted from the ligament breakup. By rearranging Eq.3.12, the final drop diameter can be expressed as

$$d_D = \frac{12}{[1+1/ALR]^{-1}\left(\frac{CU_g^2\rho_l}{\sigma}\right) + 4\left(\frac{1}{d_{L_2}} + \frac{2}{\lambda_{L_2}}\right)} \tag{3.14}$$

where $ALR = \dot{m}_g/\dot{m}_l$. The ALR term was replaced by the form of $(1+1/ALR)^{-1}$ in order to account the fact that the effect of ALR on the drop size diminishes with further increase in ALR. This is a general trend observed in number of earlier studies for both plain and prefilming airblast atomizers [**lefebvre1989**, **rizkalla1975**]. In this aerodynamic breakup sub-model, only primary breakup from the ligament was considered, and droplet evaporation was ignored.

Lefebvre and Beck [**lefebvre1992**, **beck1991**] related the parameter C on the left hand side of the Eq.3.13 to the energy transfer efficiency from the atomizing gas to the liquid as a function of the impinging gas angle. However, neither a detailed derivation nor an expression for the parameter C was provided by Lefebvre and Beck [**lefebvre1992**, **beck1991**]. Knoll and Sojka [**knoll1992**] expressed the parameter C in terms of the air to liquid ratio, atomizing gas velocity, and liquid viscosity based on the experimental observation of the

effect of each parameter on the mean drop size. Similarly, the parameter C in this present study was correlated to ALR and U_g, and expressed as

$$C = \frac{a}{U_g^b ALR^c}. \tag{3.15}$$

The constants a', b', and c' were determined by iterating the parameter C value for the best agreement with the experimental data and found to be a=3, b=1.65, and c=0.2, respectively. It is hypothesized that the parameter C decreases with increasing U_g. As the atomizing gas velocity increases, the local static pressure decreases and causes the low-velocity surrounding gas to be entrained into the atomizing gas stream [**knoll1992**]. This low-velocity entrained gas must be accelerated, and this resulted in reducing the kinetic energy for atomization [**knoll1992**]. The parameter C also decreases with increasing ALR. At higher ALR, the rate of radial expansion by the exiting gas stream increases. This causes the atomizing gas to transfer a fraction of its kinetic energy to the surrounding instead of the liquid [**knoll1992**]. Moreover, the interference between the atomizing gas streams from the dome and outer swirlers increases as the radial expansion increases at higher ALR; thereby, the fraction of the atomizing energy will be reduced.

4. SPRAY CHARACTERISTICS OF STANDARD AND ALTERNATIVE AVIATION FUELS AT NEAR LEAN BLOWOUT ENGINE CONDITIONS

4.1 Introduction

Alternative fuels have gained significant interest from the aviation industry due to increased concern for the air quality and the diversification of aviation fuel supplies. One current desire in the aviation industry is to develop non-petroleum alternative aviation fuels that provide performance identical to those of standard aviation fuels. The development of such new fuels would provide market flexibility and would not require engine redesign nor new fuel systems. However, information regarding the chemical and physical properties of the fuels, their atomization characteristics, and their combustion performance is currently lacking [**colket2017**].

The combustion of liquid fuel is strongly coupled to the atomization and air/fuel mixing processes. Insufficient atomization produces larger droplets, which can lead to formation of soot and nitric oxides due to fuel-rich combustion [**lefebvre1989**]. On the other hand, sufficient atomization quality produces many small droplets, which can lead to a greater volumetric heat release rate, easier light-up, a wider burning range, and lower pollutant emission [**lefebvre1989**]. Airblast, pressure swirl, and hybrid atomizers are widely used in gas turbine applications due to their sufficient atomization quality for gas turbine combustion.

A conventional airblast atomizer uses a large amount of air flowing at high velocity to atomize the liquid injected through the orifice [**lefebvre1989**]. Airblast atomizers provide good atomization quality and wide spray angles, resulting in less soot formation during combustion. The disadvantages of airblast atomizers are their narrow stability limits and poor atomization at engine start-up due to lower air velocity. These drawbacks of the airblast atomizer can be overcome by combining with a pressure swirl atomizer. The pressure swirl atomizer has a swirl chamber that directs liquid through a single orifice at relatively higher pressure than the airblast atomizer and provides sufficient atomization over a range of liquid flow rates, depending on the fuel supply pressure range. The pressure swirl atomizer is also

well known for easy engine start-up. The combination of these two atomizers, refered to as a hybrid airblast atomizer, allows for more flexible operability at conditions such as start-up, cruise, and maximum power conditions [**mansour2003**].

Many studies on spray characteristics of airblast and pressure swirl atomizers can be found, especially those that report the drop size, drop velocity, and cone angle. These characteristics can be strongly affected by various factors such as atomizing air velocity, liquid mass flow rate, liquid physical properties, and nozzle geometry. Wang and Lefebvre [**wang1988**] reported that an increase in the fuel injection pressure decreased the mean drop size for JP-4 and DF-2 fuels when using a pressure swirl atomizer at ambient pressure. A similar trend of decreasing mean drop size with fuel injection pressures of 3 to 9 bar was observed by Kannaiyan *et al.* [**kannaiyan2014**] using synthetic jet fuels with a pressure swirl atomizer at ambient pressure. The influence of the liquid viscosity and surface tension on droplet size was also investigated by Wang and Lefebvre [**wang1987**] using a pressure swirl atomizer. Their study found that the mean drop size increased when the liquid viscosity and surface tension were increased. Wang and Lefebvre [**wang1987**] commented that extensive measurements performed with both pressure swirl and airblast atomizers have shown that the effect of liquid density on drop size was quite small. Thus, the primary liquid physical properties that affects atomization are surface tension and viscosity.

For airblast atomizers, Batarseh *et al.* [**batarseh2010**] investigated the effect of air and liquid flow rates on mean drop size using water at ambient pressure. Their study found that the mean drop size decreased with increasing air flow rates through the swirler of the atomizer, while the effect of varying liquid flow rates was observed to be limited. Chin *et al.* [**chin2000**], Custer *et al.* [**custer1988**], and Rizkalla *et al.* [**rizkalla1975**] also observed similar trends of decreasing mean drop size with increasing air pressure drop across the swirler, but further increases in pressure drop diminished this effect. Chin *et al.* [**chin2000**] also reported that the mean drop size increased when liquid injection pressure was increased from 1 to 27 bar using a hybrid airblast atomizer, which has counter rotating inner/outer airflows in the swirler respect to rotation of injected liquid. Rizkalla *et al.* [**rizkalla1975**] investigated the effect of surface tension and viscosity on the mean drop size using an airblast atomizer. The study showed that the mean drop size increased with greater surface tension

and viscosity. Similar effects of surface tension on mean drop size were observed by Custer *et al.* [**custer1988**]. However, viscosity effects were found to be less significant for the mean drop size at higher values of air to liquid ratio (ALR) and pressure drop.

Drop velocity affects mass dispersion within the combustor and also affects the evaporation rate. Furthermore, drop velocity affects the growth of droplet instability, which is directly related to secondary breakup and atomization quality [**Lefebvre1989**]. Kannaiyan *et al.* [**kannaiyan2014**] reported that an increase in fuel injection pressure resulted in increased drop velocity using the pressure swirl atomizer at ambient pressure. A higher fuel injection pressure provides more momentum transfer to the liquid, resulting in increases in the drop velocity [**durdina2014**]. On the other hand, Ma *et al.* [**ma2014**] reported that the influence of liquid injection pressure on drop velocity of an airblast atomizer was minimal at a constant air pressure drop across the swirler. Ma *et al.* [**ma2014**] also reported that the drop velocity increased significantly when the air pressure drop was increased. Similar trends were also observed by Chin *et al.* [**chin1999**].

The spray cone angle also plays an important role in gas turbine combustion, since it can lead to better fuel-air mixing and a wider dispersion of fuel drops within the combustor. Chen *et al.* [**chen1992**] reported wider spray cone angles with increases in fuel injection pressure using a pressure swirl atomizer based on mechanical patternator measurements. Similar trends of wider spray cone angles with increasing fuel injection pressure were also found by Ortman *et al.* [**ortman1985**] and Durdina *et al.* [**durdina2014**] using pressure swirl atomizers. For airblast atomizers, Ma *et al.* [**ma2014**] reported that the effect of liquid injection pressure on the spray angle was not significant. The fuel physical properties such as surface tension and viscosity were also reported to have an influence on the cone angle. Custer *et al.* [**custer1988**] observed narrower cone angles with increases in liquid viscosity when using an airblast atomizer. It was explained that the swirling motion of the liquid sheet was decreased by the viscous forces. An increase in surface tension, on the other hand, was found to produce wider cone angles. Chen *et al.* [**chen1992**] also found that increasing the liquid viscosity resulted in narrower spray cone angles and this effect was most pronounced at the highest liquid viscosity.

Despite many parametric studies [**wang1987**, **kannaiyan2014**, **wang1987**, **batarseh2010**, **chin2000**, **custer1988**, **rizkalla1975**, **durdina2014**, **ma2015**, **chin1999**, **chen1992**, **ortman1985**] on spray characteristics of standard fuels using both pressure swirl and airblast atomizers, few provided the spray characteristics of hybrid pressure swirl airblast atomizers for newly developed alternative jet fuels. This specific hybrid atomizer was selected for integration into a non-proprietary combustor rig, termed the "Referee Rig," that was developed with input from the Original Equipment Manufacturers (OEMs) for laboratory testing (Tier 3 in the American Standard and Testing Materials (ASTM International) D4054 qualification process). The Referee Rig was developed to assess risks associated with alternative fuels and to determine if further engine tests (Tier 4 in ASTM International D4054) are warranted. The fuel effect on the ignition characteristics using various fuels was studied in the Referee Rig at lean blowout conditions at the University of Dayton Research Institute [**corporan**]. The study found a trend of improved LBO performance with an increase in derived cetane number (DCN), which is a measure of ignition quality of the fuel. Furthermore, other fuel properties in terms of physical, distillation, and chemical were observed to have no clear correlation with LBO performance in Referee Rig [**corporan2017**]. Throughout this study, however, the information with regards to atomization was not provided. The air and fuel temperatures as well as the pressure in the combustor can directly affect fuel-spray atomization and vaporization, which in turn affects the ignition performance of the combustor. Therefore, it is also important to study the spray itself to understand the fuel effects on the combustor performance at lean blowout conditions.

In the present study, the spray characteristics of standard and alternative fuels were investigated at vessel pressure, swirler pressure drop, vessel temperature, and fuel temperature, which correspond to the conditions in the Referee Rig. The effects of pressure drop, fuel injection pressure, and fuel type on mean drop sizes, drop velocities, and spray cone angles were investigated. The spray structure was also studied by varying the axial distance downstream from the injector. Phase Doppler Anemometry (PDA) was used to measure the mean diameter statistics and the axial components of drop velocity at these axial distances. In addition to providing valuable information on the spray characteristics of these alternative

fuels, the measurements presented in this work will also be useful for computational model development.

4.2 Experimental Details

4.2.1 Test rig

The Purdue Variable Ambient Pressure Spray (VAPS) rig was used to investigate the spray characteristics at near lean blowout conditions. The test rig consists of three major components: the airbox assembly, the pressure vessel, and the fuel system. The airbox assembly includes a length of pipe that was installed inside of the pressure vessel to isolate the atomizing flow from the flow in the vessel, as shown in Fig. 4.1. The pressure vessel is 305 mm in inner diameter with 12.7 mm of wall thickness and 1524 mm tall. The inner diameter of the vessel was designed to be larger than the Referee rig [**esclapez2017**], which has 110 mm of inner diameter, to prevent the spray hitting on the optical windows. The vessel has four optical windows on the same horizontal plane: two 127 mm (5 inches) in diameter and two 76.2 mm (3 inches) in diameter. Both 76.2 mm windows are oriented at 60° from one of the 127 mm windows, with one of the 76.2 mm windows located diametrically on either side.

Two heated nitrogen flows (394 K) were supplied into the airbox and the vessel: the sweeping flow and the airbox flow. The sweeping flow was directly supplied into the vessel to pressurize it and to sweep the injected fuel out of the vessel. A window purge flow line was branched out from the sweeping flow to supply the window cavities on the vessel through manifolds. The purpose of the window purge flows was to mitigate the recirculation, collection, and condensation of fuel drops and vapor on the windows, thereby avoiding obscuration for laser diagnostics measurement. The airbox flow served as the atomizing flow exiting the swirler and was also used to build pressure within the airbox in isolation from the pressure in the vessel. This created the pressure differential between the airbox and the vessel: pressure drop across the swirler ($\Delta P/P$). Figure 4.1 illustrates these flows in the VAPS test rig. All gaseous flows within this experiment were nitrogen to prevent any formation of combustible mixtures.

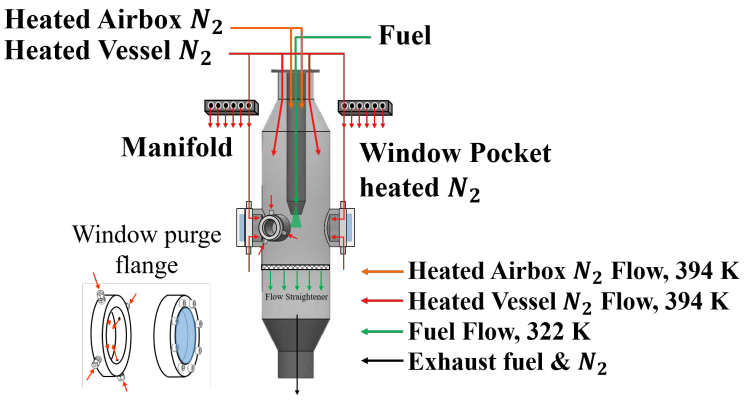

Figure4.1. Diagram of the flow system in VAPS test rig with window purge flange design

A hybrid pressure swirl airblast atomizer, designed by the Parker-Hannifin Corporation, was mounted on the end of the airbox [**mansour2003**]. The atomizer consisted of a prime injector and a gas swirler that housed the injector, as shown in Fig. 4.2. The prime injector has two different orifice sets: the pilot and the main. The pilot consisted of a single pressure-swirl orifice on the centerline of the injector. The main consisted of five orifices oriented radially outward from the injector centerline, which employs the airblast atomization mechanism. Detailed discussion on the injector operation and atomization processes can be found in Mansour *et al.* [**mansour2003**]. For this study, only the pilot nozzle was used.

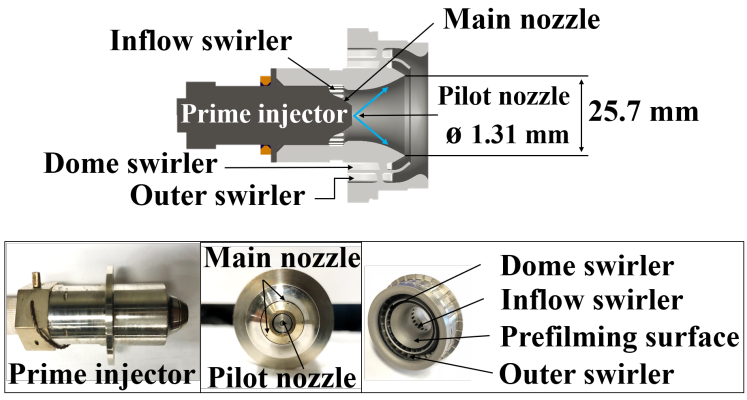

Figure4.2. Cross-section view of the Hybrid Air-blast Pressure-swirl Atomizer by Parker-Hannifin Corporation

A mobile fuel supply system was used to supply fuel to the VAPS rig. The fuel was pressurized and supplied to the main and pilot circuits of the injector using a gear pump. The fuel temperature was measured at just upstream of the prime injector inlet port. The pressure in the pilot fuel line at top of the airbox was measured as the fuel injection pressure.

4.2.2 Fuels

Five different fuels were investigated at near LBO conditions: A-2, C-1, C-5, C-7, and C-8. These fuels were the same as those used by Colket *et al.* [**colket2017**]. The A-2 (Jet-A) was selected as a reference fuel by comparing seven different fuel properties among the three different category A fuels: A-1 (JP-8), A-2 (Jet-A), and A-3 (JP-5). The seven properties are density, freeze point, viscosity, flash point, aromatics, cetane number, and hydrogen content. The category C fuels are candidate alternative fuels. Colket *et al.* [**colket2017**] described these fuels as unusual and outside the range of commonly used fuel; their unique features include narrowly distributed aromatics at the front-end of the boiling range and fuels with hydrocarbons confined to a narrow range of carbon numbers. The C-1 fuel is composed of heavily branched iso-alkanes and has an extremely low derived cetane number relative to other candidate fuels [**colket2017**]. The C-5 fuel is a blend of 1,3,5 trimethyl benzene with a C_{10} iso-paraffinic solvent, and has a very low boiling point [**colket2017**]. The C-7 and C-8 fuels are characterized as high cycloparaffin and high aromatic fuel, respectively.

The physical properties of each fuel can be found in Table 4.1. Surface tension, viscosity and density of each fuel were estimated at LBO condition using a curve fit based on data provided by the Air Force Research Laboratory (AFRL) [**edwards2017**]. These estimated values may have significant uncertainties due to values being scaled for temperature rather than being measured at LBO conditions.

4.2.3 Phase Doppler Anemometry

Phase Doppler anemometry was used to measure the drop size and drop velocity. Detailed discussion of the technique and the theory behind PDA can be found in Albrecht *et al.* [**albrecht2003**]. The physical setting and optical configurations for the PDA are shown in

Table4.1. Normalized physical properties of alternative fuels to the values of A-2 fuel at 322 K (A-2 : μ_l= 1.1×10^{-3} $kg/m.s$, σ = 0.024 N/m, ρ_l = 778 kg/m^3).

Fuel Property	A-2	C-1	C-5	C-7	C-8
Dynamic viscosity, μ_l	1.00	0.77	0.47	0.34	0.34
Surface tension, σ	1.00	0.88	0.87	1.04	0.98
Density, ρ_l	1.00	0.94	0.95	1.02	1.03

Fig. 4.3 and Table 4.2. The receiving probe with 310 mm focal length lens was oriented at a scattering angle of 60° from the laser exiting the transmitter, which contained a 400 mm focal length lens. The PDA system has three different aperture mask types (A, B, and C) which can be varied depending on the interest drop size range. For this study, an 'A' type of aperture mask was used, and this mask has an approximate drop size range of 1.8 μm - 95 μm. Two identical Zaber translation stages were used to move the transmitter probe and the receiving probe to the measurement locations, which were between ±30 mm from the center of the spray in 5 mm increments. Ten repeated measurements were taken with 20,000 samples recorded at each measurement location. The spherical validation and validation rates were in range of 93 - 95 % for all ten repeated measurements.

Table4.2. Optical PDA setting

Aperture mask	A
Spatial filter	Slit = 200 μm
Scattering angle	60°
Receiver optic lens	f = 310 mm
Transmitter optic lens	f = 400 mm

The uncertainties for PDA measurements at each radial location are shown in Table 4.3. The uncertainties for D_{10}, D_{32}, and MMD were obtained using standard deviations of 10 repeated measurements at each radial location. At radial location of 0 mm and 15 mm, the uncertainties for the axial velocity and MMD were higher than 10 %, however, the absolute uncertainties were much smaller compared to the averaged measurement values. The uncertainty bars on the U_z plots are the root-mean square (RMS) values. Detailed

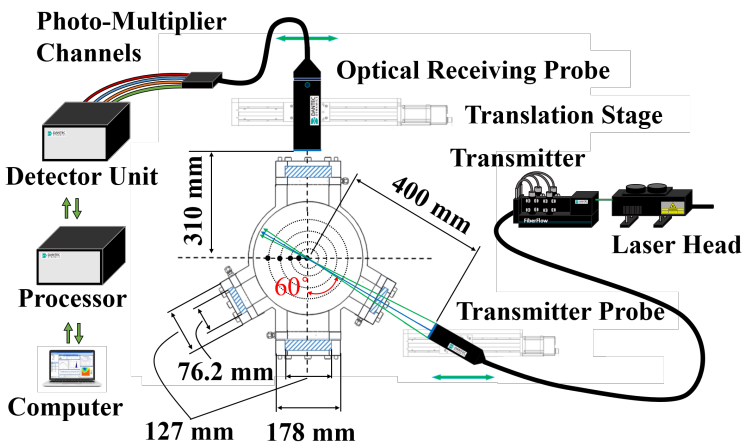

Figure4.3. Schematic of the PDA system set-up around the VAPS rig

discussion on the PDA uncertainty calculation using the standard deviation was reported in [**rodrigues2015**].

Table4.3. Uncertainties for D_{10}, D_{32}, MMD, U_z

r [mm]	U(D_{10})	U(D_{32})	U(MMD)	U(U_z)
30	2.7 %	2.4 %	3.5 %	3.6 %
25	2.3 %	2.1 %	2.3 %	3.3 %
20	2.3 %	1.9 %	2.3 %	4.8 %
15	2.0 %	1.8 %	2.1 %	12%
10	1.5 %	2.8 %	3.1 %	2.9 %
5	1.7 %	5.5 %	8.4 %	2.6 %
0	1.9 %	6.5 %	10%	2.8 %

4.2.4 Operating Conditions

Near lean blowout conditions in this study were defined by setting the vessel pressure, fuel temperature, and atomizing gas temperature to 2.07 bar, 322 K, and 394 K respectively. The varied parameters were the pressure drop across the gas swirler ($\Delta P/P$) and the fuel injection pressure differential across the pilot orifice (ΔP_{pilot}). The pressure drop across the swirler was quantified as a percentage of the pressure difference between the airbox and the vessel divided by the pressure in the vessel. The pressure drop, $\Delta P/P$, had values of 2, 3, and 4%. The fuel injection pressure differential was defined by the pressure difference

between the fuel line and the vessel. The injection pressure differential, ΔP_{pilot}, had values of 1.72, 3.45, and 5.17 bar. The spray measurements for A-2, C-1, and C-5 were performed at three different planes downstream from the swirler exit: 12.7, 25.4, and 38.1 mm as shown in Table 4.4.

Table 6.3 shows the percent uncertainties for operating condition measurements, such as the pressure drop across the swirler, fuel temperature, fuel injection pressure differential, vessel pressure, vessel temperature, and atomizing flow temperature. These uncertainties were obtained using standard deviations.

Table4.4. Spray Operating Conditions

Injector	z **[mm]**	$\Delta P/P$ **[%]**	ΔP_{pilot} **[bar]**
100 % Pilot	12.7	2.00 3.00 4.00	1.72
100 % Pilot	25.4	2.00 3.00 4.00	1.72
100 % Pilot	25.4	3.00	3.45 5.17
100 % Pilot	38.1	2.00 3.00 4.00	1.72

Table4.5. Uncertainties for Operating Conditions

Operating Parameters	**Operating Conditions**	**Uncertainty**
$\Delta P/P$	2,3,4 %	4.1 %
T_{fuel}	322 K	0.8 %
ΔP_{pilot}	1.72 Bar	3.2 %
P_{vessel}	2.07 Bar	0.3 %
T_{vessel}	394 K	1.7 %
T_{gas}	322 K	0.8 %

4.2.5 Cone Angle Measurement

The effect of fuel injection pressure (ΔP_{Pilot}) and pressure drop ($\Delta P/P$) on the full spray cone angle was investigated for A-2, C-1, and C-5 fuels using high-speed shadowgraph imaging. The ΔP_{Pilot} was varied to values of 1.72, 3.45, and 5.17 bar at $\Delta P/P = 2$ %. The

$\Delta P/P$ was varied to values of 2, 4, or 6% at $\Delta P_{Pilot} = 1.72$ bar. The full cone angle at 25.4 mm downstream from the swirler exit was estimated by adapting the Sobel edge detection method to average of 3,000 spray shadowgraph images. The linear regression was done along the detected edge to evaluate the angle between the centerline of the spray. Figure 4.4 shows the schematic diagram for the high-speed shadowgraph imaging set-up with the VAPS rig.

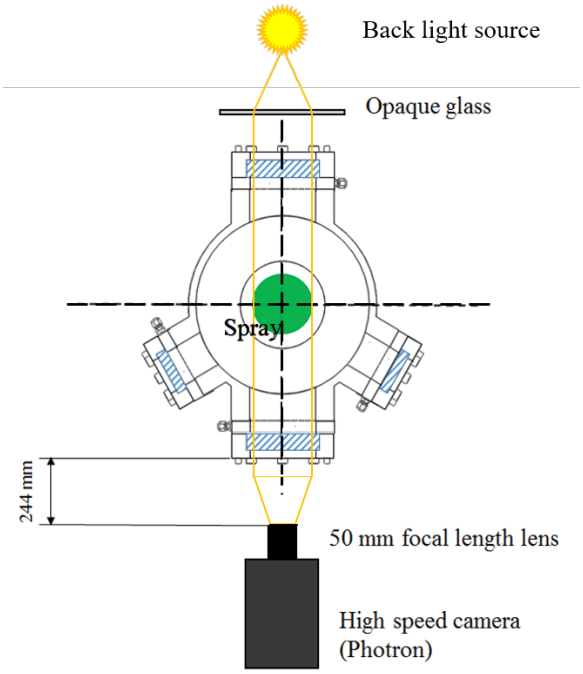

Figure4.4. Schematic diagram of the high speed shadowgraphic imaging set-up around the VAPS rig

4.3 Results and Discussion

4.3.1 Spatially-Resolved Drop Diameters and Velocities

The general atomization process of the pilot nozzle for the hybrid atomizer involves: (1) fuel injected from the pilot nozzle impinging on the prefilming surface, (2) the resulting fuel film flowing along the surface towards the prefilmer lip and thickening at the bottom of the prefilmer lip, (3) and formation of the ligaments as the fuel film extends off the tip of the prefilmer. The ligament then disintegrate to drops by interacting with the outer swirl gas flow. Some of these droplets experience secondary breakup in the bag regime, contributing

to the multiplicity of drop sizes [**sforzo2019**]. Figure 4.5 illustrates the spray of the hybrid atomizer.

The spray was characterized using D_{10}, D_{32}, MMD, and U_z for both the standard fuel A-2 (Jet-A) and alternative fuels (C-1, C-5, C-7, and C-8). The resulting D_{10}, D_{32}, MMD, and U_z are shown in Fig. 4.6 at three different measurement planes (12.7 mm, 25.4 mm, and 38.1 mm) for the C-1 fuel at conditions of $\Delta P/P$ = 3 %, T_{fuel}= 322 K, and T_{gas}= 394 K. Symmetry of the spray was observed at this representative condition for all three measurement planes. Due to continued observation of drop size distributions were radially symmetric to within experimental uncertainty at different operating conditions for each fuel, subsequent results presented in this paper will highlight measurements for the positive radial locations only.

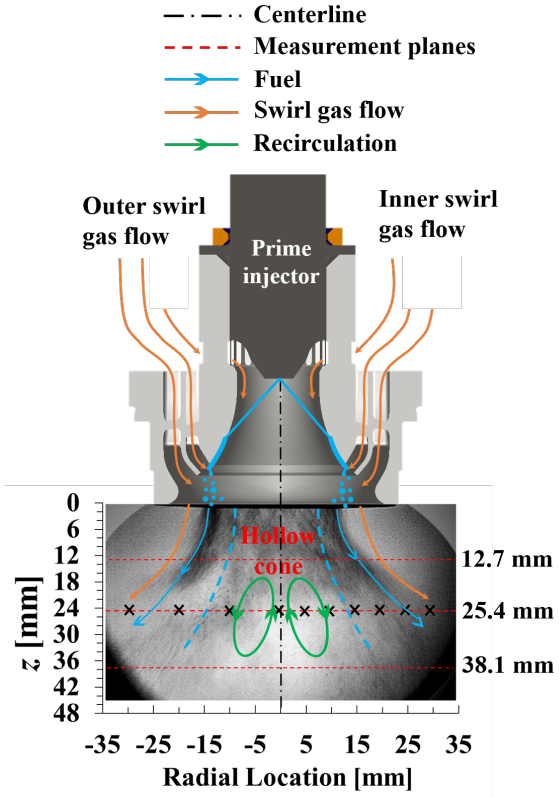

Figure4.5. Diagram of spray behavior for the hybrid atomizer

Smaller drop sizes (D_{10}, D_{32}, and MMD) were observed at the center of the spray (r = 0 mm) at each measurement plane. This region of smaller drop diameters can be attributed

to a recirculation zone in the hollow cone region of the spray, as shown in Fig. 5.2. The recirculation zone is caused by a lower pressure region within the hollow cone due to the mixture of fuel and nitrogen exiting the injector and gas swirler at high velocities. Smaller droplets that do not possess enough inertial force to maintain their trajectories are believed to recirculate back into the hollow cone due to entrainment. This observation was supported by the U_z distribution in Fig. 4.6(d). The U_z values near the center of the spray were observed to be negative, whereas radial locations greater than ± 10 mm were observed to have positive values. Positive U_z values indicate that the fuel droplets are traveling away from the injector, while negative U_z values indicate droplets traveling back towards the injector. The relative velocity between the fuel and gas was also estimated using the lowest Stokes number drops, which characterize the particle behavior suspended in the gas flow. The droplet sizes that have Stokes number less than 0.1 were selected from the PDA measurement data, and the gas velocity was obtained by averaging the axial velocity of each drop size that has Stokes number less than 0.1. The relative velocities were found to be varied within 2.7 m/s for pressure drop of 2%, 3.1 m/s for 3%, and 3.6 m/s for 4% of pressure drop.

As shown in Fig. 4.6, the largest mean diameters at each measurement plane were observed towards the edge of the spray. The D_{10} distribution showed the largest mean drop size at a radial location of ± 15 mm for the 12.7 mm plane. This shifted to ± 20 mm for the 25.4 mm plane and ± 30 mm for the 38.1 mm plane. Similarly, the largest drop sizes for D_{32} and MMD were observed at $r = \pm 10$ mm for the 12.7 mm plane, ± 15 mm for the 25.4 mm plane, and ± 30 mm for the 38.1 mm plane. These observations demonstrate that the larger drops continue to spread radially outward as they travel downstream of the injector and maintain their initial trajectory. This is due to their ability to maintain enough inertial force to overcome drag and entrainment by the atomizing gas flow.

The drop size and drop axial velocity of half radial profile of the spray were also measured at $z = 3.0$, 12.7, 25.4, and 38.1 mm downstream of the gas swirler for A-2 and C-5 fuels as shown in Fig.4.7. At the measurement plane of $z = 3.0$ mm, the drop size was still able to be measured and the spherical validation of 93% was achieved. Furthermore, the Weber number and Ohnesorge number for the drop size at $z = 3.0$ mm were estimated to be 2.0 and 0.08, respectively. This suggests that droplets at $z = 3.0$ mm are not likely to experience

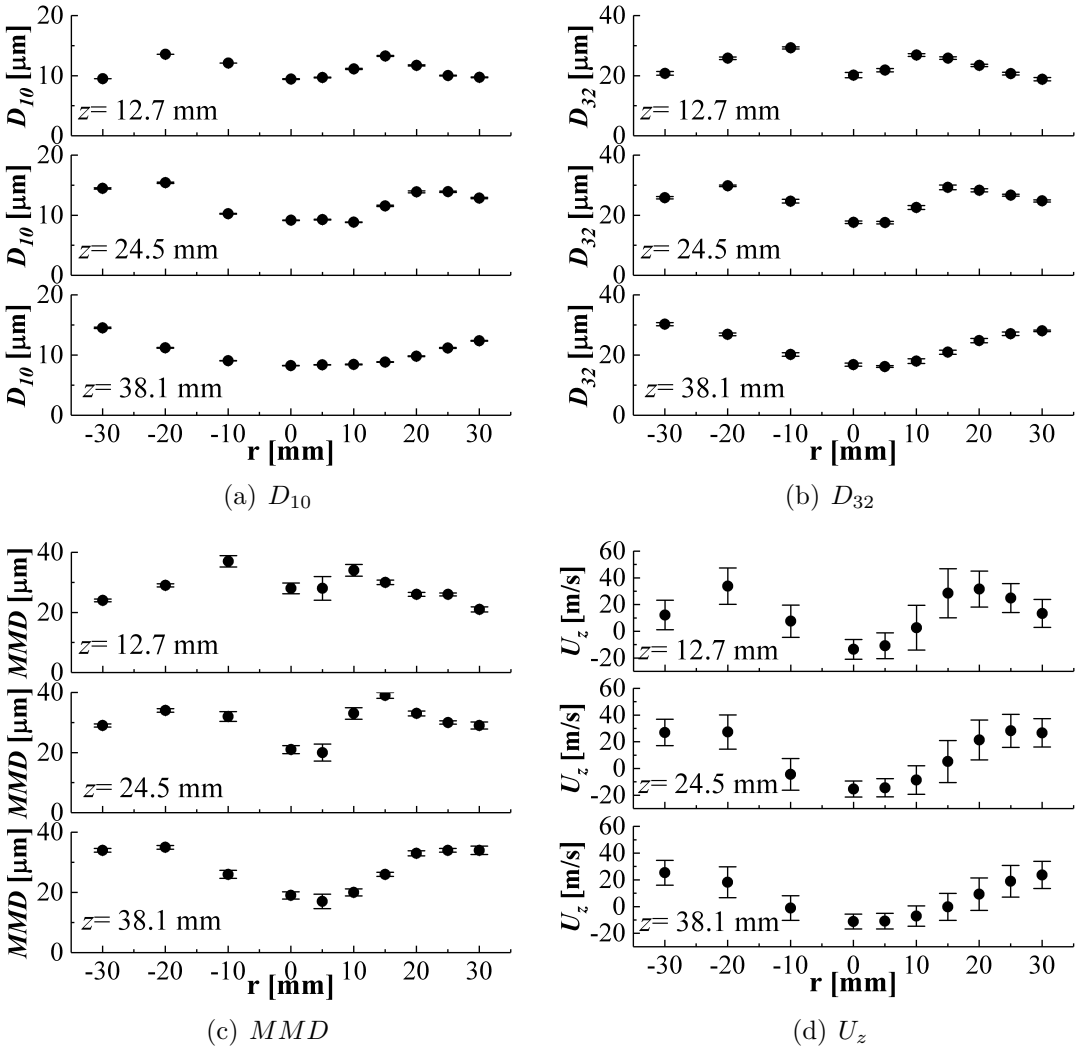

(a) D_{10} (b) D_{32}

(c) MMD (d) U_z

Figure4.6. Drop diameter and drop velocity distributions for C-1 at $\Delta P/P$=3 % for z=12.7, 24.5, and 38.1 mm

secondary atomization, based on the droplet deformation regime analysis by Hsiang *et al.* [**hsiang1992**].

The local data rate at each radial location were obtained from the PDA measurement. Figure 4.8 shows the local data rate at three different measurement planes for the C-1 fuel. The lowest data rates were observed at the center of the spray, and relatively lower data rate was observed within the hollow cone of the spray. The peaks of the data rate profile at each measurement plane indicates the thick fuel stream of the spray, which were observed at $r = \pm$ 20 mm for the measurement plane of z = 12.7 mm, $r = \pm$ 25 mm for z = 25.4

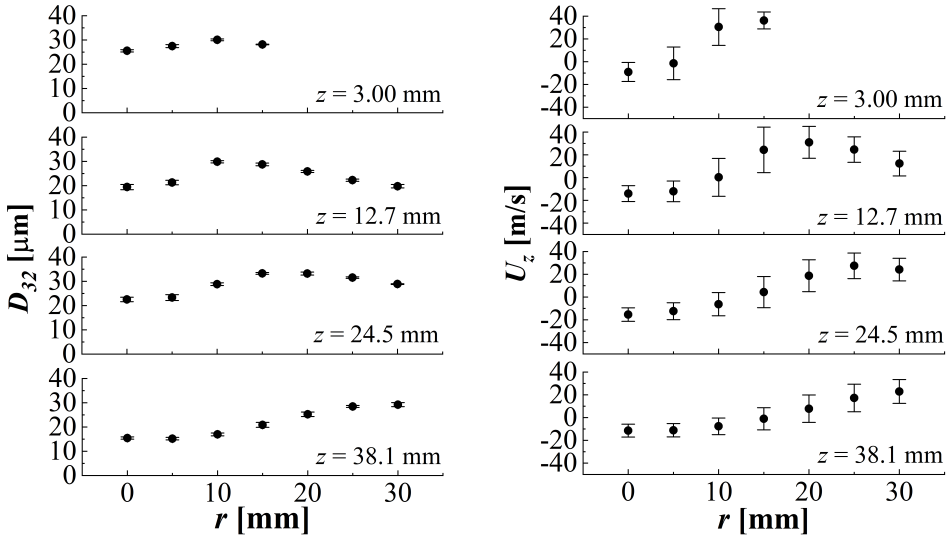

(a) D_{32}, A-2 (b) U_z, A-2

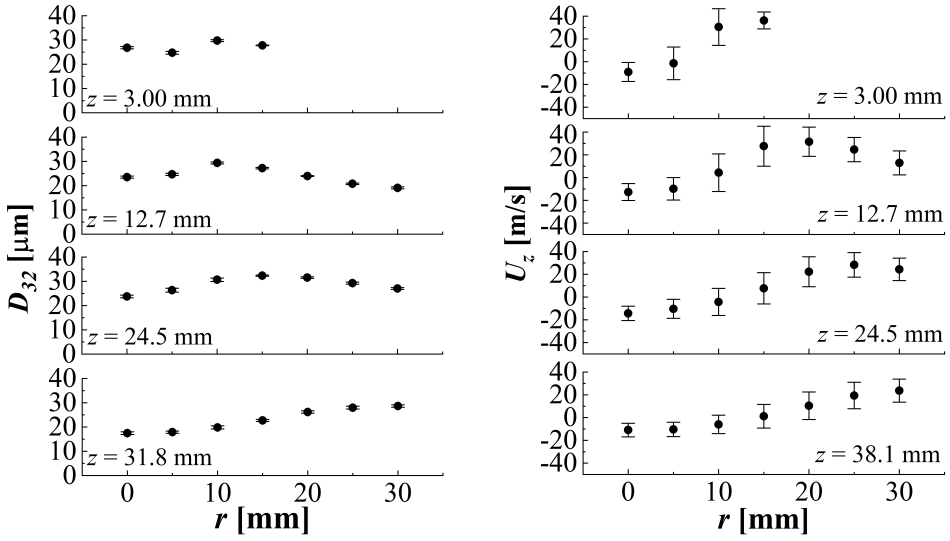

(c) D_{32}, C-5 (d) U_z, C-5

Figure4.7. D_{32} and U_z distributions for A-2 and C-5 fuels at $\Delta P/P$=3 % for z=3.0, 12.7, 24.5, and 38.1 mm

mm, and $r = \pm$ 30 mm for z = 38.1 mm. As similar to the observation of the mean drop size distributions, this peak was observed to shift towards the edge of the spray as the axial distance downstream of the injector increased. These trends were also observed for other fuels.

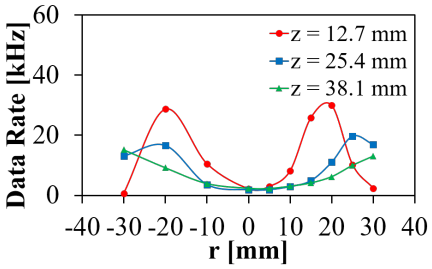

Figure4.8. Data rate at $\Delta P/P$=3 %, ΔP_{Pilot}=1.72 bar, and z=12.7, 25.4, 38.1 mm for C-1

4.3.2 Full Cone Angle

The full cone angles at z= 25.4 mm downstream of the swirler exit were measured using shadowgraph images. Measurements were obtained to investigate the effect of pressure drop across the swirler ($\Delta P/P$) and the fuel injection pressure (ΔP_{Pilot}) for A-2, C-1, and C-5 fuels. The pressure drop across the swirler was 2, 4, or 6% at ΔP_{Pilot} = 1.72 bar. The fuel injection pressure was 1.72, 3.45, or 5.17 bar at $\Delta P/P$ = 2 %. It was observed that the cone angle variations among three fuels were minimal. Furthermore, the effect of $\Delta P/P$ and ΔP_{Pilot} on the spray cone angles were not significant, and their variations were within the margin of experimental uncertainty.

4.3.3 Effect of Swirler Pressure Drop

The pressure drop across the swirler ($\Delta P/P$) was observed to have a significant effect on the D_{10}, D_{32}, MMD, and U_z for both standard (Jet-A) and alternative aviation fuels (C-1, C-5, C-7, and C-8). Figure 4.10 show that D_{10}, D_{32}, and MMD decreased with increasing $\Delta P/P$ for all radial locations. The magnitude of drop velocity was observed to increase for greater $\Delta P/P$, as presented in Fig. 4.10(d). Higher $\Delta P/P$ results in higher atomizing gas

Table4.6. Full Cone Angle Measurement

$\Delta P/P$ [%]		2.00	2.00	2.00	4.00	6.00
ΔP_{pilot} **[bar]**		1.72	3.45	5.17	1.72	1.72
A-2	Mean	59.7	58.9	58.5	63.3	61.7
	Uncertainty	±1.3	±0.5	±1.5	±1.0	±0.4
C-1	Mean	58.2	59.9	61.1	63.9	61.9
	Uncertainty	±2.1	±3.7	±1.0	±1.4	±1.4
C-5	Mean	56.2	55.9	57.1	59.3	58.2
	Uncertainty	±1.3	±0.4	±0.8	±2.2	±1.5

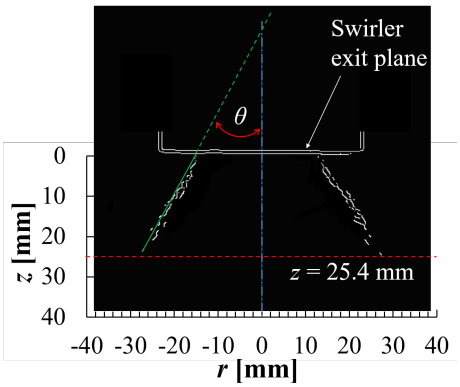

Figure4.9. Coneangle estimation at z=25.4 mm using Sobel edge detection technique.

velocity, which leads to greater inertial and aerodynamic forces to overcome the viscous and surface tension forces of the bulk liquid. This results in the observed smaller drop diameters. The variation in mean drop diameters with increase in $\Delta P/P$ from 3 to 4% was observed to be smaller than the variation with $\Delta P/P$ from 2 to 3%. No significant variation was observed at r = 15 mm, where the mean drop velocity was approximately zero. This observation was attributed to the transition of the spray from the hollow cone to the fuel cone, which is a defining feature of the spray pattern. Similar trends in drop size and velocity as function of $\Delta P/P$ were observed at the measurement planes of 12.7 and 38.1 mm.

Figure 4.11 shows the D_{10}, D_{32}, MMD, and U_z at each measurement plane for C-1 fuel. Mean drop sizes were also observed to decrease with increasing $\Delta P/P$. The droplet axial velocities also showed a similar trend of increasing axial velocity with greater $\Delta P/P$. In addition, a similar transition location between the hollow cone and fuel cone was observed

based on the axial velocity measurements. These trends were also observed for C-5, C-7, and C-8 fuels and can be seen more clearly in Fig. 4.12, which shows the D_{10}, D_{32}, MMD, and U_z only at $z = 25.4$ mm measurement plane for C-7 fuel.

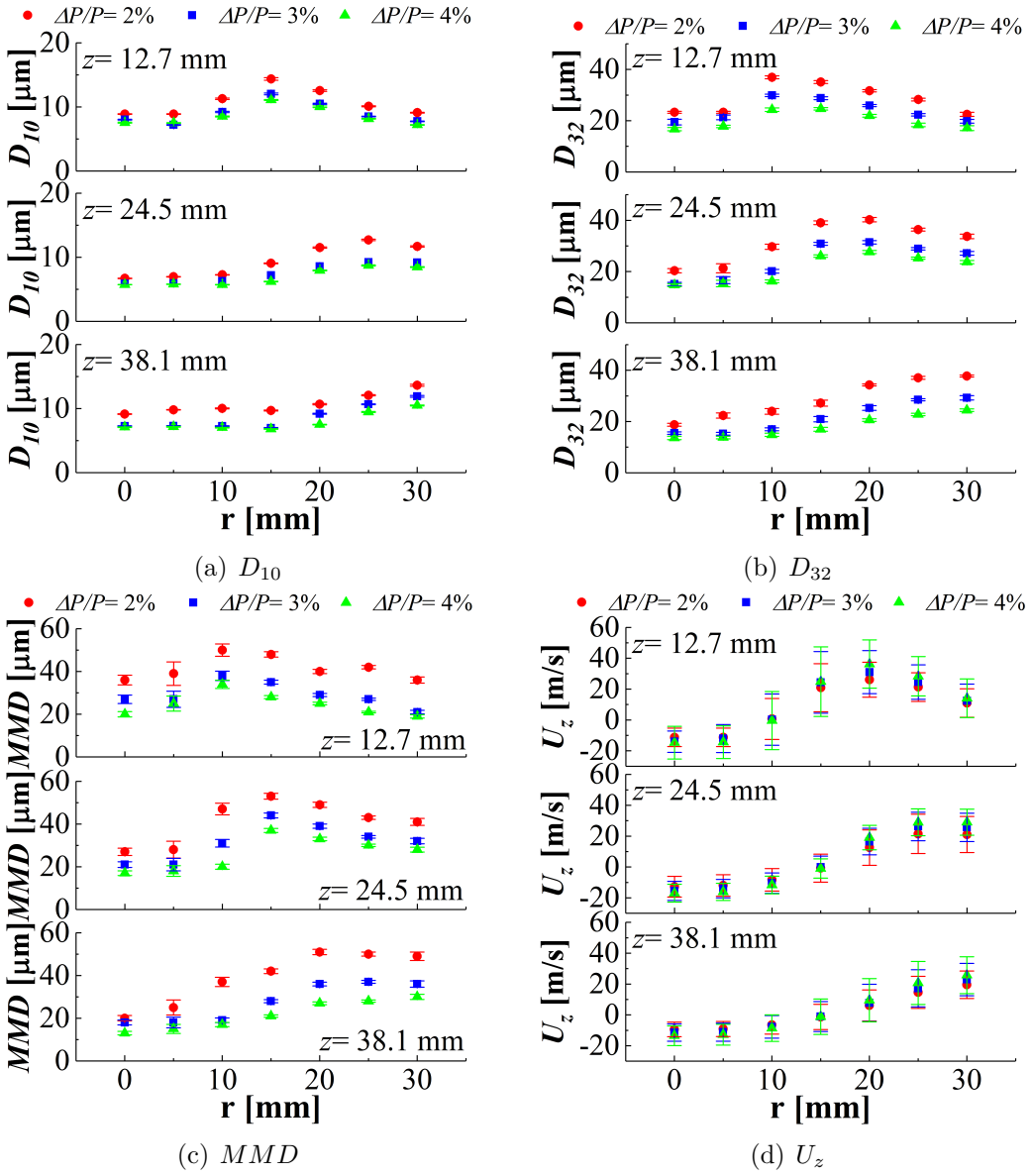

(a) D_{10} (b) D_{32}

(c) MMD (d) U_z

Figure4.10. Drop diameter and drop velocity distributions for A-2 at $\Delta P/P$=2, 3, 4 % for z=12.7, 25.4, and 38.1 mm

Figure 4.13 shows drop size and drop velocity probability density functions (pdfs) for different $\Delta P/P$ values at the 25.4 mm measurement plane for A-2 fuel. The drop diameter on x-axis for the number diameter probability density function in Fig. 4.13(a,c,e,g) was

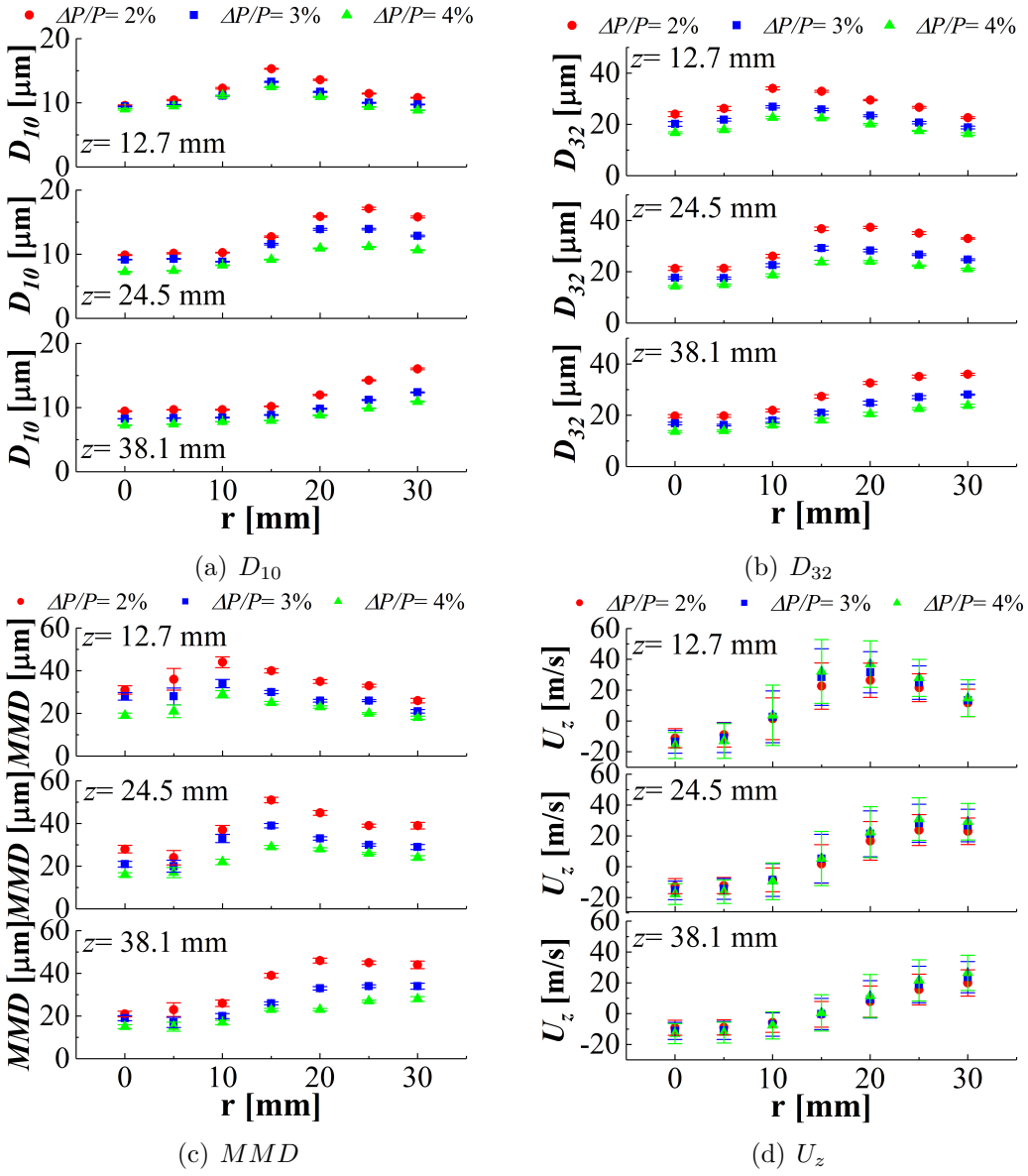

(a) D_{10} (b) D_{32}

(c) MMD (d) U_z

Figure4.11. Drop diameter and drop velocity distributions for C-1 at $\Delta P/P$=2, 3, 4 % for z=12.7, 25.4, and 38.1 mm

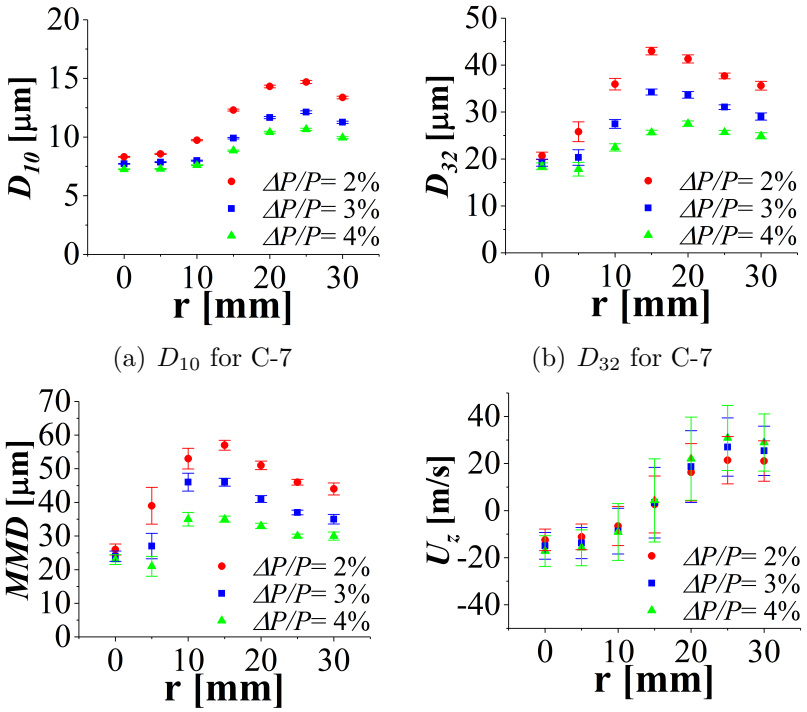

(a) D_{10} for C-7

(b) D_{32} for C-7

(c) MMD for C-7

(d) U_z for C-7

Figure4.12. Drop diameter and drop velocity distributions for C-7 at $\Delta P/P$ =2, 3, 4 % for z=25.4 mm

truncated to $0 - 50$ μm from $0 - 120$ μm measurement range to highlight the effect of $\Delta P/P$ on the smallest drop sizes. The number pdf was observed to shift towards smaller diameters with increasing $\Delta P/P$. The number of smaller droplets increased with greater $\Delta P/P$ and the number of larger drops decreased with increasing $\Delta P/P$. This shift in the distribution agrees well with the mean diameters observations in Fig. 4.10. The comparisons of the velocity pdfs with $\Delta P/P$ variation are shown in Fig. 4.13(b,d,f,h). It was observed that the distribution shifted towards a higher velocity magnitude range for greater $\Delta P/P$. In addition, the span and mode of the velocity probability density distribution was observed to vary with radial location. The drop velocities near the center of the spray were observed to be negative and this confirms that a majority of the droplets near the center were traveling back towards the injector within the hollow cone. At radial locations of 10 mm and 20 mm, both positive and negative velocities were observed, which was not discernible simply

from the U_z plot. Similar trends in the drop size and velocity pdfs were observed for the alternative fuels C-1, C-5, C-7, and C-8.

4.3.4 Effect of Fuel Type

The effect of fuel type (A-2, C-1, C-5, C-7, and C-8) was investigated at lean blowout conditions for $\Delta P/P$ = 2, 3, and 4%. Figure 4.14 shows D_{10}, D_{32}, MMD, and U_z for each fuel at the 25.4 mm measurement plane. Measurements showed that the C-1 fuel formed the largest D_{10} consistently across all radial locations, while A-2 formed the smallest D_{10}. The D_{32} and MMD measurements, however, showed that C-7 formed the largest D_{32} and MMD, while C-1 formed the smallest D_{32} and MMD. The differences in mean drop size between fuels at various radial locations were less than 5 μm for D_{10} and D_{32}; differences were within 10 μm for MMD. The U_z measurements, however, showed no significant variations among the fuels.

The fuel A-2 was found to have the highest viscosity value among the five fuels at near lean blowout conditions, as shown in Table4.1, which should lead to the formation of the largest mean drop sizes. However, A-2 produced the smallest D_{10}. Nevertheless, excluding the A-2 fuel, the trend observed in D_{10} tends to follow the fuel viscosity trend. For instance, the C-7 and C-8 fuels were found to have the lowest viscosity and formed the smallest D_{10}. These viscosity trends, however, were not observed in D_{32} and MMD. Furthermore, D_{32} and MMD were not observed to follow trends based on differences in surface tension and density. Similar effect of viscosity on mean drop size was observed by Custer *et al.* [**custer1988**]. Custer *et al.* investigated the effects of atomizer ALR and liquid properties (surface tension and viscosity) on D_{32} (Sauter mean diameter) using three different designs of hybrid airblast atomizer [**custer1988**]. Their study found that viscosity had minimal effect on D_{32} at higher ALR and pressure drop values for all three atomizers.

For presented work, the ALR value was four times higher than the values that Custer *et al.* used; moreover the viscosity values were varied in much narrower range among fuels. Custer *et al.* [**custer1988**] also found that surface tension had the most dominant effect on D_{32} for all three hybrid atomizer designs when it was varied up to 50 % in difference.

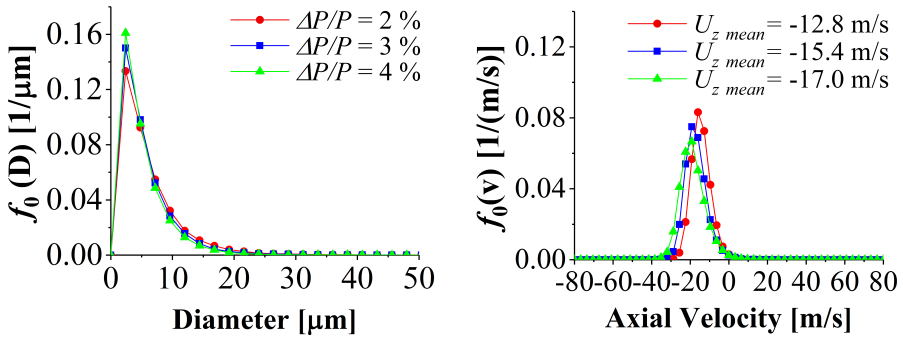

(a) $f_0(d)$ at $r = 0$ mm

(b) $f_0(v)$ at $r = 0$ mm

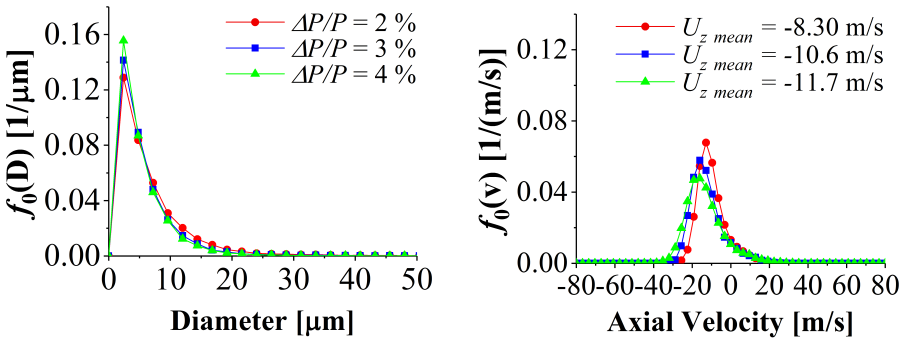

(c) $f_0(d)$ at $r = 10$ mm

(d) $f_0(v)$ at $r = 10$ mm

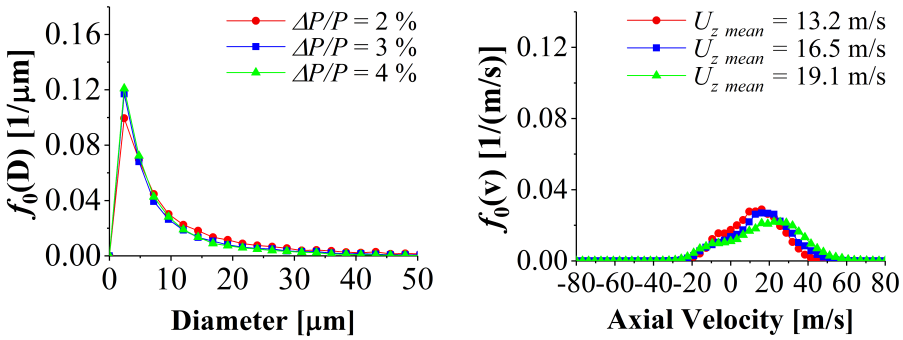

(e) $f_0(d)$ at $r = 20$ mm

(f) $f_0(v)$ at $r = 20$ mm

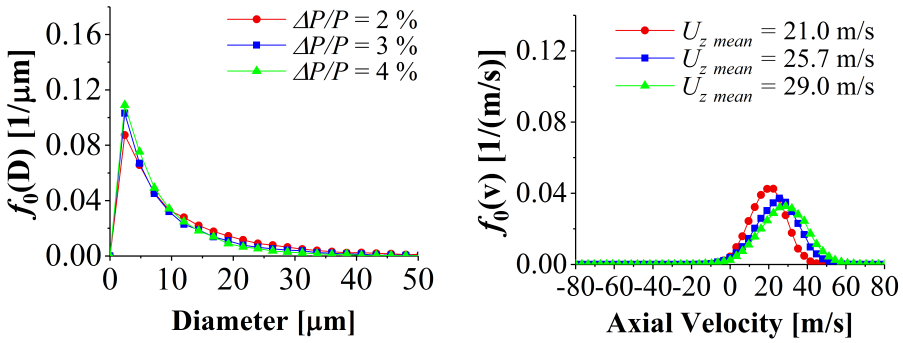

(g) $f_0(d)$ at $r = 30$ mm

(h) $f_0(v)$ at $r = 30$ mm

Figure4.13. Number probability density functions for drop size and axial velocity for A-2 at $\Delta P/P$=2, 3, 4 % and ΔP_{Pilot}=1.72 bar for z=25.4 mm

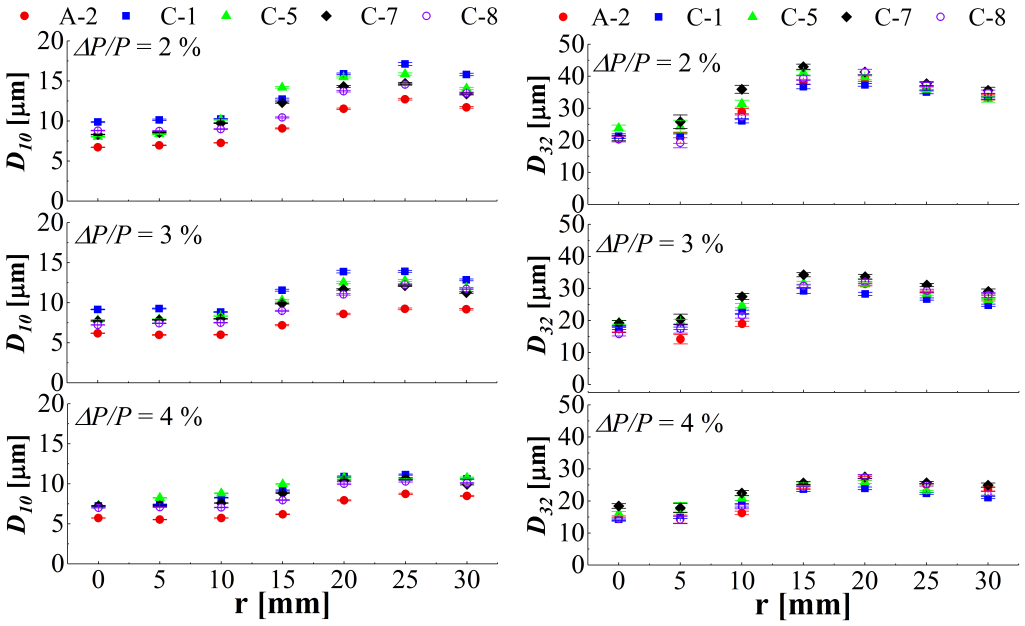

(a) Fuel type D_{10} at $\Delta P_{Pilot} = 1.72$ bar

(b) Fuel type D_{32} at $\Delta P_{Pilot} = 1.72$ bar

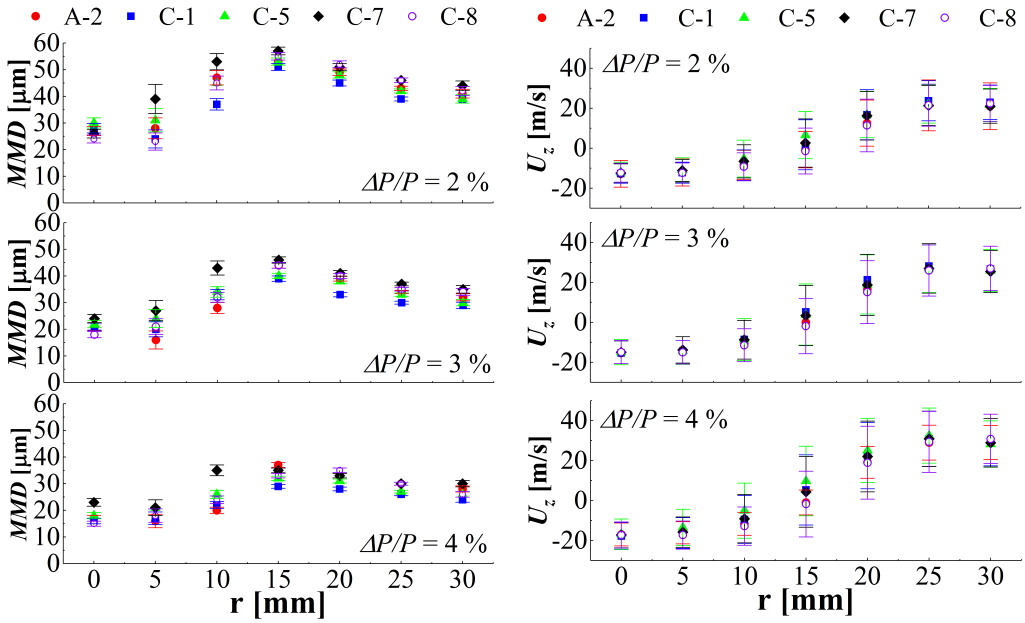

(c) Fuel type MMD at $\Delta P_{Pilot} = 1.72$ bar

(d) Fuel type U_z at $\Delta P_{Pilot} = 1.72$ bar

Figure4.14. Drop diameter and velocity comparisons for all five fuels at $\Delta P/P$=2, 3, 4 % for z=25.4 mm

However, the differences in surface tension for presented work were less than 14 %. Figure 4.15 shows the relations between fuel dynamic viscosity and surface tension and dimensionless measured drop size (D_{32o}/d_o) each for three different pressure drops of 2%, 3%, and 4%. This relation clearly showed that the effect of fuel viscosity on the drop size is limited while the effect of surface tension is still observed. This is believed to be due to the high impingement angle of the swirling gas flow onto ligament that was formed at the prefilmer tip. With higher viscosity, the longer disturbance wavelength and slower growth rate of disturbance on the ligament is expected due to resistance force to deformation. If the gas impingement angle is lower or close to parallel to the ligament axial direction, the viscosity effect may still be seen in drop formation. However, if gas flow impinges at angle close to normal to the ligament axial direction, the surface tension is the only force that is responsible for the drop formation. For clear explanation on the effect of high gas impingement angle on the drop formation, further experimental work would be needed. It was also observed that the increases in pressure drop diminished the variation in drop sizes among fuels in Fig. 4.14. The model successfully demonstrated the drop size trends that were observed with fuel viscosity and surface tension. It should be noted that the physical properties used in Table4.1 may have significant uncertainties due to the values being scaled for temperature, rather than being measured values. Accurate measurements of the physical properties for these fuels at near lean blowout conditions corresponding to the spray measurements would lead to more accurate conclusions regarding the effect of fuel type on the spray, particularly for the A-2 case.

4.3.5 Effect of Fuel Injection Pressure

The fuel injection pressure differential ΔP_{Pilot} across the pilot nozzle was varied to investigate the effect of the inertial force on the mean diameters (D_{10}, D_{32}, MMD) and the drop velocity (U_z) for values of 1.72, 3.45, and 5.17 bar. The injection pressure differential dictates the total fuel mass flow rate through the pilot nozzle. The mass flow rates as measured by a Coriolis flow meter for each fuel injection pressure were 2.52, 3.56, and 4.59 g/s respectively. The effect of the fuel injection pressure on the mean drop size and velocity was

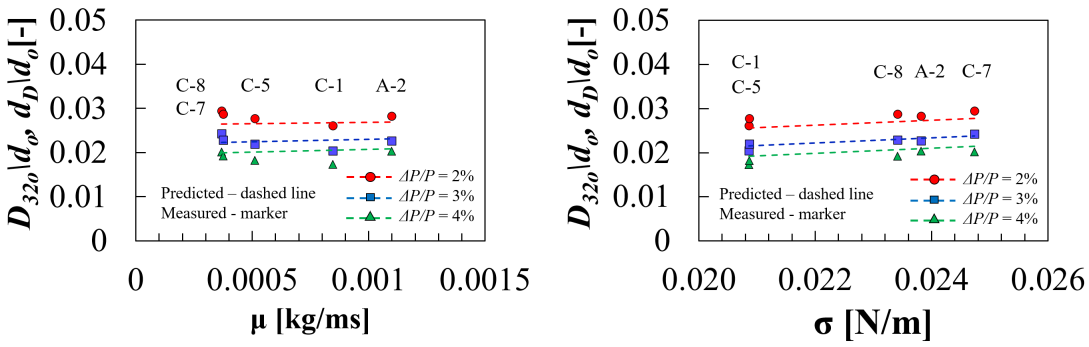

(a) D_{32o}/d_ovs μ (b) D_{32o}/d_ovs σ

Figure4.15. Relation between dynamic viscosity / surface tension and D_{32o}/d_o at $\Delta P/P$=2, 3, 4 % for r = 20 mm and z=25.4 mm

found to be minimal. Figure 4.16 shows the D_{10}, D_{32}, MMD, and U_z for the A-2 fuel. An increase in ΔP_{Pilot} from 1.72 bar to 5.17 bar resulted in slight increases in D_{10}, while the variations in D_{32}, MMD, and U_z were observed to be within the experimental uncertainties. The variations in D_{10} were observed to be in the range of 1 to 3μm with uncertainties of less than 1μm at each radial location. The variations in D_{32} and MMD were found to be in the range of 1 to 3μm, however, they were observed to be within the 3μm uncertainties, except at radial locations of r = 10 and 15 mm for MMD. For U_z, the variations were found to be less than 1 m/s. Moreover, the C-1 fuel showed no significant variation in D_{10}, D_{32}, MMD, and U_z for ΔP_{Pilot} variation from 1.72 bar to 3.45 bar. ΔP_{Pilot} variation from 1.72 bar to 5.17 bar for the C-5 fuel also showed similar trends. Chin *et al.* [**chin2000**] reported that the swirler arrangement in hybrid airblast atomizer had a significant effect on mean drop size. Their study found that mean drop size was increased with increasing liquid injection pressure in the range of 1 to 27 bar when the hybrid airblast atomizer had counter-rotating flows with injected liquid rotations for both inner and outer swirlers. The hybrid pressure swirl airblast atomizer used in presented work had the same swirler arrangement. However, the investigation was limited to much narrower injection pressure range. It was believed that the variations in fuel injection pressure (1.72 to 5.17 bar) were not significant enough to have any effects on mean drop size due to the dominating effect of the atomizing gas from the airblast component of the atomizer.

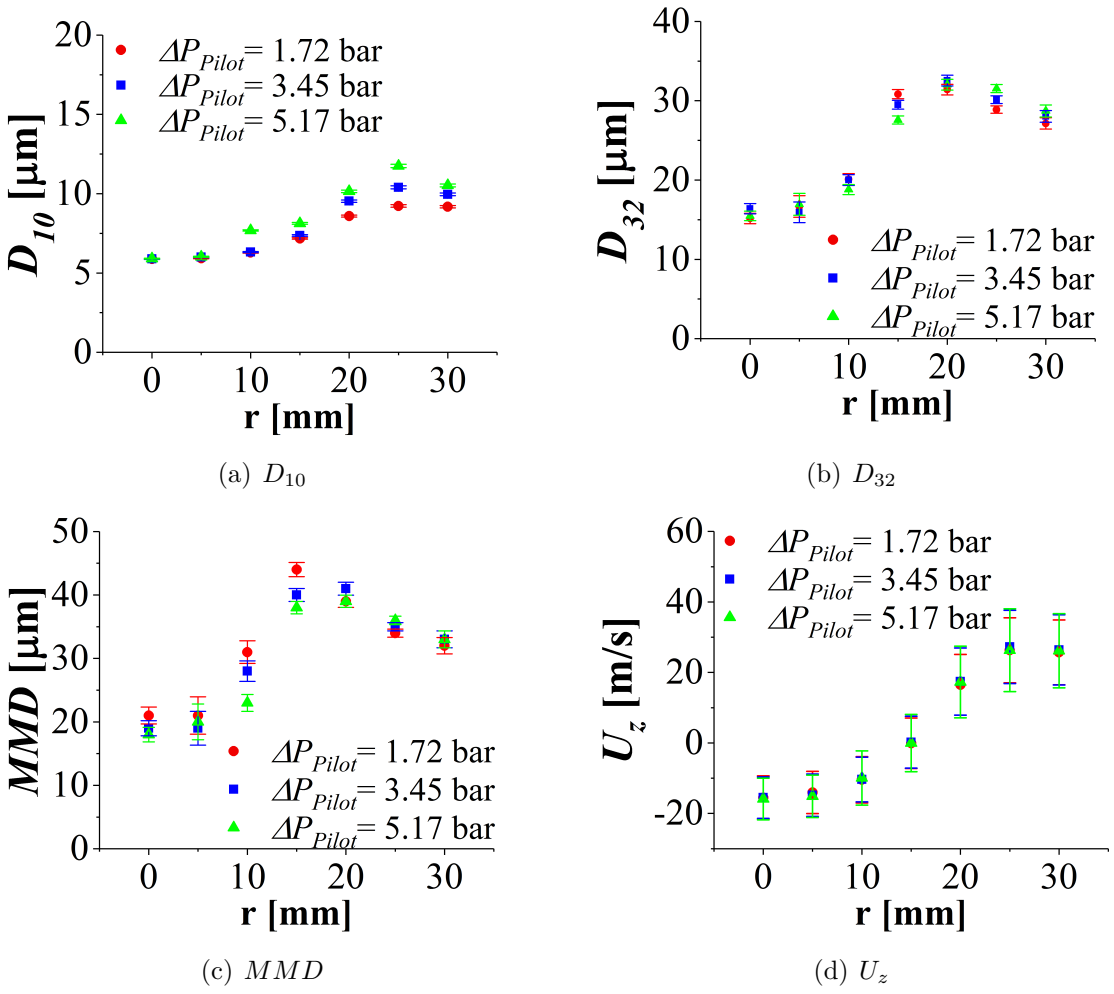

(a) D_{10} (b) D_{32}

(c) MMD (d) U_z

Figure4.16. Drop diameter and velocity distributions for A-2 fuel at ΔP_{Pilot}=1.72, 3.45, and 5.17 bar, $\Delta P/P$=3 %, and z=25.4 mm

Figure 4.17 shows the dimensionless measured line-of-sight D_{32} (D_{32}/d_o) with increasing fuel injection pressure at $\Delta P/P = 3\%$ for A-2 fuel. The drop size was observed to increase slightly at higher injection pressure. This is due to reduction in relative velocity between the liquid and gas as the fuel mass flow rate increases with injection pressure. The model prediction (d_D/d_o), however, shows minimal change in drop size with increasing fuel injection pressure.

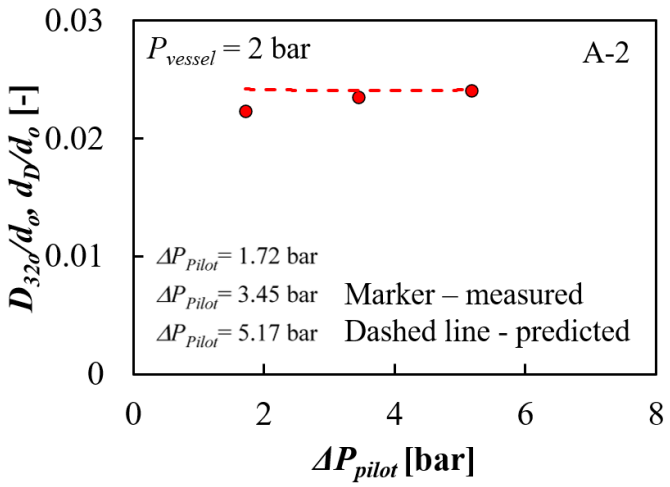

Figure4.17. D_{32o}/d_o and d_D/d_o for A-2 fuel at ΔP_{Pilot}= 1.72, 3.45, and 5.17 bar, $\Delta P/P$ =3 %, and z=25.4 mm

4.4 Summary

The spray characteristics of standard and alternative aviation fuels were studied at near lean blowout conditions ($P_{vessel} = 2.07$ bar, $T_{fuel} = 322$ K, and $T_{gas} = 394$ K) using a hybrid pressure swirl airblast atomizer. The effect of pressure drop ($\Delta P/P$) on the drop size and drop velocity was investigated at three different measurement planes using PDA, and the spray full cone angle was measured using shadowgraph imaging. The investigation of the spray at multiple measurement planes showed that the larger drops tend to maintain their trajectories and continued to spread radially while traveling downstream of the injector. An increase in the pressure drop across the swirler resulted in a decrease in mean drop sizes and an increase in axial velocity for both standard and alternative fuels. The effects of the

fuel type on drop size and velocity were investigated by comparing the physical properties of each fuel. The trend in the D_{10} distribution was observed to follow the viscosity trends, except for the A-2 fuel. However, no definitive relationship was observed in D_{32}, MMD, and U_z with the physical properties. The effect of fuel injection pressure (ΔP_{Pilot}) was also investigated and it was observed to have no significant effect on drop size or drop velocity due to limited injection pressure range. Similar spray characteristics between the standard and alternative fuels at near LBO conditions are encouraging for the potential incorporation of aviation fuels with slightly different physical properties. Future work includes investigating the spray characteristics at a cold start (P_{vessel} = 1.01 bar, T_{fuel} = 239 K, and T_{gas} = 239 K).

5. SPRAY CHARACTERISTICS OF STANDARD AND ALTERNATIVE AVIATION FUELS AT ENGINE COLD START CONDITIONS

5.1 Introduction

The dependence of the aviation industry on petroleum-derived fuels has sparked interest towards developing and incorporating alternative fuels composed solely of hydrocarbons. Key benefits of such alternative fuels include diversifying the energy supply, potentially reducing fuel costs, and mitigating impacts on the environment [**hileman2014**]. Crucial requirements for these alternative fuels, however, include seamless integration without engine redesign and incorporation without new infrastructure on the ground or in flight. Furthermore, their atomization quality and performance in combustion must be comparable to the standard fuels.

Certifying new alternative fuels through the American Standard and Testing Materials (ASTM) D4054 qualification process is required for commercial deployment [**colket2017**]. This can be a long and expensive process since it requires both extensive laboratory testing and full-scale engine testing to assess performance of the candidate alternative fuels. Testing of these fuels is required at representative engine conditions such as near lean blowout, cold start, and high altitude re-light. Evaluation of the spray characteristics at these conditions are also needed since the performance of the combustor is strongly dependent on the atomization. Sufficient atomization, which produces many smaller droplets, provides greater fuel surface, better air-fuel mixing, and lower pollutant emissions [**lefebvre1989**].

The atomization process can be strongly affected by atomizer type, liquid properties, and engine operating conditions. Airblast, pressure-swirl, and hybrid atomizers are widely used in gas turbine engine applications due to their effective atomization. Airblast atomizers use high-velocity airstreams to atomize a thin conical liquid sheet and provide a wide spray angle, resulting in lower soot formation [**lefebvre1989**]. However, the known disadvantages of airblast atomizers include a relatively narrow stability range and poor atomization at engine start-up due to lower air velocity [**lefebvre1989**, **mansour2003**]. Pressure-swirl

atomizers, which have a swirl chamber that directs liquid through a single orifice at relatively higher pressure, provide good performance during engine start-up and sufficient atomization over a wide range of liquid flow rates depending on the fuel supply pressure [**lefebvre1989**]. However, its cone angle is more sensitive to changes in ambient gas density compared to an airblast atomizer. The individual drawbacks of the airblast and pressure-swirl atomizers can be minimized by combining them. The hybrid pressure-swirl airblast atomizer retains advantages of both airblast and pressure-swirl atomizers and provides more flexible engine operability at start-up, cruise, and maximum power conditions [**mansour2003**].

The air-to-liquid ratio (ALR) of the hybrid pressure-swirl airblast atomizer (HPSA) is an important operating parameter that can significantly affect the combustion process [**lefebvre1989**]. The pressure drop across the swirler is often the key parameter of interest when investigating the effect of ALR, since it controls the air flow rate through the swirler. Batarseh *et al.* [**batarseh2010**] investigated the effect of ALR on mean drop size using a pre-filming airblast atomizer and observed smaller mean drop sizes with increasing air flow rates through the swirler. This trend of smaller mean drop size with increasing ALR, controlled through the pressure drop across the swirler, was also observed by Chin *et al.* [**chin2000**], Custer *et al.* [**custer1988**], and Rizkalla *et al.* [**rizkalla1975**]. These studies also noted that the effect of pressure drop was diminished with further increases.

The effect of fuel physical properties on the spray characteristics is of interest when studying the performance of alternative fuels, especially since the liquid physical properties can be strongly dependent on the fuel temperature. Rizkalla *et al.* [**rizkalla1975**] investigated the influence of liquid properties on spray characteristics created by an airblast atomizer and reported larger drop sizes with increased liquid-gas surface tension and liquid viscosity. Custer *et al.* [**custer1988**] observed a similar trend between liquid-gas surface tension and mean drop size, but also found viscous effects to be less significant at higher values of ALR and pressure drop across the swirler.

The representative diameters that are typically used to characterize sprays are D_{10}, D_{32}, and MMD. The arithmetic mean diameter (D_{10}) is a first-order mean representing the average drop diameter and is commonly used for general comparison. The Sauter mean diameter (D_{32}) is a fifth-order mean representing the ratio of drop volume to drop surface area. It

is a representative diameter commonly used for comparisons in mass transfer and reaction applications, such as gas turbine engines. The mass median diameter (MMD) is the diameter at which 50% of the total liquid volume is contained within smaller diameters. MMD is also commonly used to describe the spray for combustion applications. The detailed discussion for these representative diameters is well explained in the literature [**lefebvre1989**, **mugele1951**].

The existence of temporal and spatial fluctuations in two-phase (liquid and gas) flows through the combustion chamber may cause unsteadiness in the spray. This could potentially cause combustion instabilities or higher levels of undesirable exhaust gas emissions due to unexpected fluctuations in the local air-to-fuel ratio. A spray can be evaluated to determine if it behaves in a steady or unsteady manner using methodologies such as the one developed by Edwards and Marx [**edmarx19951**, **edmarx19952**]. The spray is determined to be steady if the interparticle arrival time distributions obey inhomogeneous Poisson statistics. The interparticle arrival time gaps and interparticle time distribution functions can be calculated using the droplet arrival times recorded by the PDA system.

The experimental interparticle time distribution $h_{exp}(\tau_{\mathrm{j}})$ and the theoretical interparticle time distribution $h_{th}(\tau_{\mathrm{j}})$ can be determined from a single long realization (SR).

$$h_{exp}(\tau_{\mathrm{j}}) = \frac{H(\tau_{\mathrm{j}})}{N\Delta\tau_{\mathrm{j}}} \tag{5.1}$$

$$h_{th}(\tau_{\mathrm{j}}) = \frac{\lambda_{SR}}{N\Delta\tau_{\mathrm{j}}} \tag{5.2}$$

where $H(\tau_{\mathrm{j}})$ is the measured number of events in the jth interparticle time gap, N is the total number of interparticle events, and $\Delta\tau_{\mathrm{j}}$ is the width of the jth interparticle time gap [**edmarx19951**, **edmarx19952**]. For the general experiment, the histogram of h_τ should follow a linearly truncated exponential decay. However, for long sample times (SR), such as the current measurement case, a pure exponential decay is expected in the time distribution since the spray is assumed to be driven by a Poisson process. The analytical expression of

$h_{th}(\tau_{\mathrm{j}})$ can be defined by λ_{SR}, which is the number of particles sampled per unit time in the experiment, and can be expressed as

$$\lambda_{SR} = \frac{n}{T} \tag{5.3}$$

Here n denotes the number of particles measured in each drop size category, and T is the total arrival time. In order to compare two distributions, a Chi-square goodness of fit test was used to determine whether the spray is steady or unsteady. Detailed discussion of the Chi-square goodness of fit test can be found in Luong *et al.* [**luong1999**].

The present work is part of an on-going effort by the National Jet Fuels Combustion Program (NJFCP) to streamline the certification process of alternative aviation fuels. Combustion tests have been performed in a generic combustion rig, with input from engine original equipment manufacturers (OEMs), as part of Tier 3 in the ASTM D4054 qualification process [**corporan2017**]. The ignition characteristics of the alternative fuels at lean blowout (LBO) conditions showed that the LBO performance tended to be improved as the derived cetane number (DCN) was increased. Other fuel properties in terms of physical, distillation, and chemical characteristics were observed to have no clear correlation with LBO performance [**corporan2017**]. Atomization tests were also performed at near LBO conditions, and no significant differences in the spray characteristics were observed between standard (Jet-A) and candidate alternative fuels (C-1, C-5, C-7, and C-8) [**shin2019**].

Building upon the earlier investigations at LBO conditions, the spray characteristics of three fuels at engine cold start conditions were investigated in the present work. The cold start conditions, which are characteristics of start-up conditions for the engine in cold weather, are defined here as: ambient gas pressure $P_{amb} = 1.01$ bar, fuel temperature $T_{fuel} =$ 239 K, and atomizing gas temperature $T_{airbox} = 239$ K. The work presented here considers the spray characteristics, including the drop size and drop velocity, for two standard fuels (A-2 and A-3) and one alternative fuel (C-3). The same hybrid pressure-swirl airblast atomizer as the previous works was used in this study. The influence of the pressure drop on the spray characteristics was studied, and fuel effects on the atomization are discussed. The drop sizes and drop velocities at near LBO and cold start conditions were also compared to

see the effect of operating conditions. A semi-empirical model was also developed for the atomization process of the HSPA atomizer used in the experiments. The predicted drop sizes were compared to the measured drop sizes at both near LBO and cold start conditions. These experimental and modeling efforts will contribute towards developing a streamlined certification process for commercial deployment of alternative fuels, as well as the validation of computational models for gas turbine engine combustion.

5.2 Experimental Apparatus and Systems

5.2.1 Test Facility

The Purdue Variable Ambient Pressure Spray (VAPS) test rig shown in Fig. 5.1 is capable of creating conditions over a wide range of ambient pressures, atomizing gas temperatures, and fuel temperatures for spray measurements. The two major components of the VAPS rig are the airbox and the pressure vessel. The airbox, which is a length of pipe, allows the atomizing gas flow to be isolated from the vessel flow. This enables the creation of a pressure difference between the airbox and the pressure vessel. For cold start conditions, a liquid nitrogen flow was introduced into a gaseous nitrogen flow upstream of the airbox to achieve the desired atomizing gas temperature of 239 K. The airbox flow exited through the gas swirler of the hybrid pressure-swirl airblast atomizer, which is mounted at the exit of the airbox.

As shown in Fig 5.1, The pressure vessel had four optical windows. Both 76.2 mm windows were oriented at 60° from one of the 127 mm windows, with one of the 76.2 mm windows located diametrically on either side. The vessel flow was heated up to 360 K and supplied directly into the vessel. The window purge flow was branched out from the vessel flow and supplied to each window purge flange to minimize the fuel wetting on the window. These heated flows also prevented condensation on the outer side of the windows. A chiller unit, which features two heat exchangers and a heat exchanger fluid, was used to chill the fuel to the desired temperature corresponding to the cold start condition (239 K).

The hybrid pressure-swirl airblast atomizer was manufactured by the Parker-Hannifin Corporation, and a schematic diagram of the spray behavior for the HSPA atomizer is

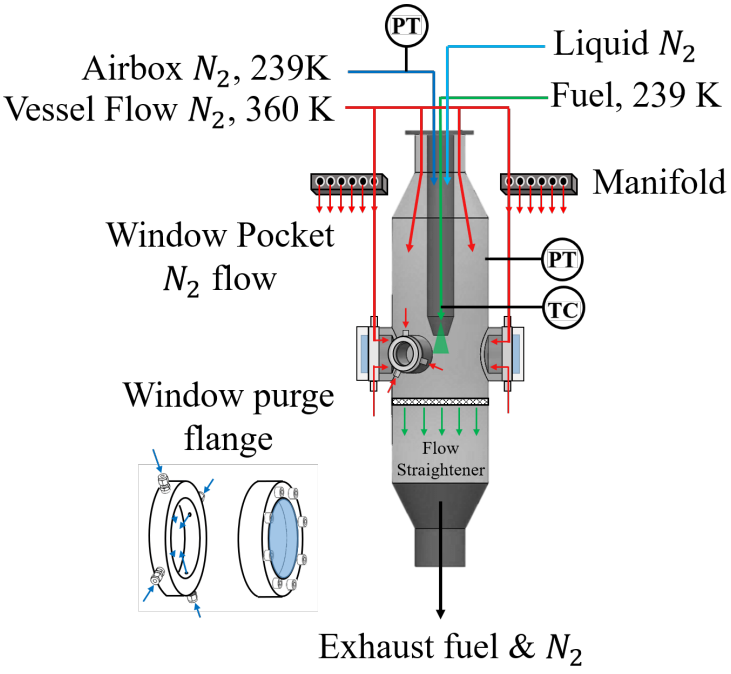

Figure5.1. Schematic diagram of the VAPS pressure vessel with four nitrogen flows.

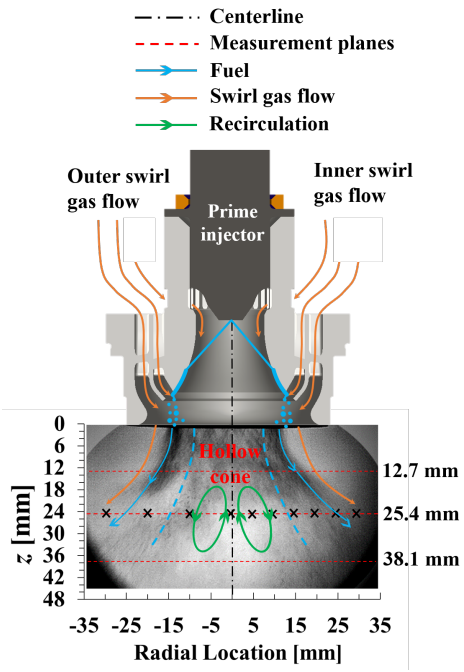

Figure5.2. Spray behavior in the atomizer and PDA measurement locations marked as × [**shin2019**].

shown in Fig. 5.2. The atomization process when using only the pilot fuel nozzle for this particular hybrid atomizer involves: (1) the fuel spray from the pilot nozzle impinges on the prefilming surface, (2) a fuel film develops along the surface and thickens towards the prefilmer tip, (3) ligaments are formed as the thickened fuel film extends off the prefilmer tip, (4) the ligaments are disintegrated into drops by the outer swirling gas flow. Some of these droplets experience secondary atomization, in the bag break-up regime, resulting in a multiplicity of drop sizes [**sforzo2019**]. A detailed discussion on this hybrid atomizer can be found in Mansour *et al.*[**mansour2003**].

5.2.2 Phase Doppler Anemometry

A phase Doppler anemometry (PDA) system was used to measure the drop diameter by measuring the phase difference of Doppler-burst signals from different detectors. The drop velocity was simultaneously determined from the frequency of Doppler-bursts from the detectors. A detailed discussion of PDA measurement theory can be found in references such

as Albrecht *et al.* [**albrecht2003**]. The PDA system around the VAPS rig is shown in Fig. 5.3. The same PDA system that we previously used for the LBO measurements [**shin2019**] was also used for the cold start measurements in the present work. Measurements were performed at spatial locations between ±30 mm from the centerline of the spray in increments of 5 mm. The translation of the PDA system was constrained within ±30 mm interval due to interference from the mounting flange of the 76.2 mm window. At each measurement location, 20,000 samples were recorded per test condition. The validation and spherical validation rates were in the range of 93 - 95 % for all ten repeated measurements at each radial location. The key optical settings for the PDA measurement are shown in Table 6.1.

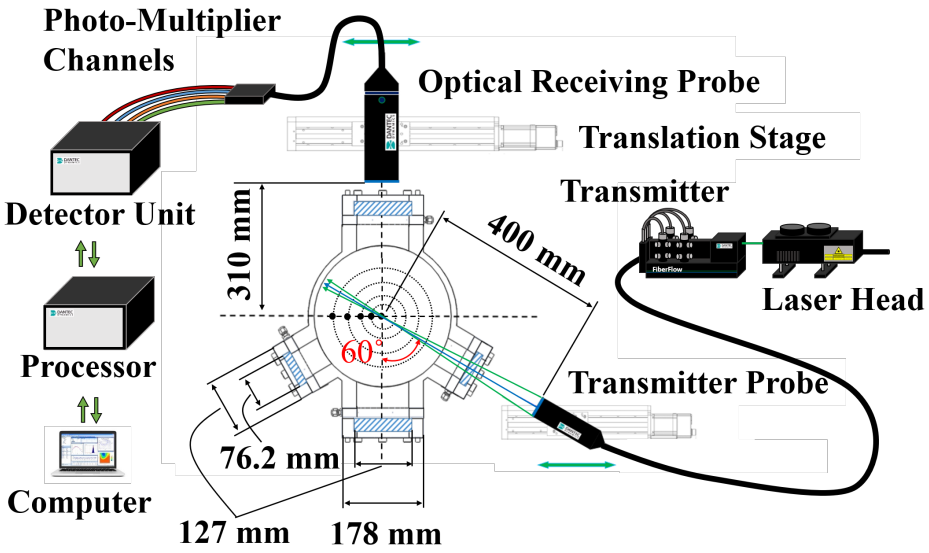

Figure5.3. Schematic diagram of the PDA system alignment relative to the VAPS rig [**shin2019**].

The uncertainties for the PDA measurements, listed in Table 6.2, were obtained using the standard deviations of ten repeated measurements at each radial location, following the approach of Rodrigues *et al.* [**rodrigues2015**]. The uncertainties for the U_z and MMD at some radial locations were higher than 5%. However, the absolute uncertainties at these locations were very small.

Table5.1. PDA Optical settings

Aperture mask	Mask A
Spatial filter	Slit 200 m
Scattering angle	60
Receiver optic lens	f 310 mm
Transmitter optic lens	f 400 mm

Table5.2. Uncertainties for D_{10}, D_{32}, MMD, U_z

r [mm]	**U**(D_{10})	**U**(D_{32})	**U**(MMD)	**U**(U_z)
30	1.3 %	1.8 %	2.9 %	3.9 %
25	2.8 %	2.3 %	3.5 %	3.7 %
20	1.7 %	1.6 %	2.3 %	2.4 %
15	1.4 %	1.9 %	2.5 %	3.0 %
10	0.9 %	2.3 %	3.6 %	2.6 %
5	1.5 %	3.1 %	4.3 %	2.3 %
0	1.2 %	3.2 %	6.8 %	2.5 %

5.2.3 Test Fuels Details

Jet-A (A-2), JP-5 (A-3), and a blend of JP-5 and farnesane (C-3) were investigated in this study. The standard aviation fuels are represented by the code A, while the alternative fuel is represented by the code C [**colket2017**]. The A-2 fuel was found to be an "average fuel" among the A fuels based on seven different properties: density, flash point, freeze point, viscosity, aromatics content, cetane number, and hydrogen content [**colket2017**]. The A-3 fuel was found to have a high flash point, viscosity, and aromatics content, while the C-3 fuel was characterized as the highest viscosity fuel among several candidate alternative fuels. Detailed discussions regarding fuel physical properties, chemical compositions, and fuel selection methods can be found in Colket et al.[**colket2017**]. The key physical properties of each fuel, such as surface tension, viscosity, and density, are shown in Table 6.5. These fuel properties were extrapolated and estimated at a fuel temperature of 239 K using measured values provided by the Air Force Research Laboratory (AFRL) [**edwards2017**]. The surface tension and density values of all three fuels only differed by 6 % and 2 %, respectively. The viscosity of each fuel, however, differed by 57 %.

Table5.3. Normalized physical properties of fuels to the values of the A-2 fuel at 239 K (A-2 : $\mu_l = 6.1\times10^{-3}\ kg/m.s$, $\sigma = 0.031\ N/m$, $\rho_l = 840\ kg/m^3$)

Fuel Property	A-2	A-3	C-3
Dynamic viscosity, μ_l	1.00	1.41	1.80
Surface tension, σ	1.00	0.97	0.94
Density, ρ_l	1.00	1.03	1.00

5.2.4 Test Operating Conditions

The cold start conditions were defined as a vessel pressure (P_{amb}) of 1.01 bar, fuel temperature (T_{fuel}) and atomizing gas temperature (T_{airbox}) of 239 K, and fuel injection pressure (ΔP_{pilot}) of 1.72 bar, as shown in Table 5.4. The fuel injection pressure (ΔP_{pilot}) is defined as the pressure differential between the fuel line and the vessel. The pressure drop across the

gas swirler ($\Delta P/P$) denotes the pressure difference between the airbox and the vessel in this study. The parameter $\Delta P/P$ was varied for values of 2, 3, and 4 % at each measurement plane. The measurement plane indicates the axial distance (z) downstream from the swirler exit plane, and it was varied to 12.7, 25.4, and 38.1 mm. The uncertainty of each operating parameters is shown in Table 6.3, using the approach by Kline *et al.* [**kline1953**].

Table5.4. Operating conditions

Injector	**ΔP/P** [%]	**ΔP_{Pilot}** [bar]	**P_{vessel}** [bar]	ALR	**z [mm]**
100 % Pilot	2.00	1.72	1.01	12.0	12.7
					25.4
					38.1
100 % Pilot	3.00	1.72	1.01	15.0	12.7
					25.4
					38.1
100 % Pilot	4.00	1.72	1.01	17.0	12.7
					25.4
					38.1

Table5.5. Uncertainties for Operating Conditions

Operating Parameters	**Operating Conditions**	**Uncertainty**
$\Delta P/P$	2, 3, 4 %	4.1 %
T_{fuel}	239 K	0.9 %
ΔP_{pilot}	1.72 Bar	3.5 %
P_{vessel}	1.01 Bar	0.3 %
T_{vessel}	360 K	2.3 %
T_{airbox}	239 K	0.8 %

5.3 Results and Discussion

5.3.1 Spatially-Resolved Drop Diameters and Drop Velocities

The spray of the standard (A-2 and A-3) and alternative (C-3) fuels was characterized using D_{10}, D_{32}, MMD, and U_z. The symmetry of the spray, in terms of the spatially-resolved mean drop size and axial velocity distributions, was consistently observed for the C-3 fuel at a variety of test conditions. Figure 5.4 shows the mean drop sizes and the axial drop velocities at three different measurement planes for the baseline condition corresponding to $\Delta P_{Pilot} = 1.72$ bar, $\Delta P/P = 3$ %, $T_{Fuel} = 239$ K, and $T_{airbox} = 239$ K.

The seagull-shaped profile in terms of spatial position was observed for the D_{10}, D_{32}, and MMD as shown in Fig. 5.4. The smaller values of D_{10}, D_{32}, and MMD found near the center of the spray can be attributed to the recirculation zone within the hollow cone of the spray. The recirculation zone was caused by the lower pressure region within the hollow cone, which was created by the fuel and gas mixture exiting the injector at high velocity and with a high swirl. This caused the gas flow to recirculate towards the spray center. The smaller drops, which were not able to maintain their trajectory due to their lower inertial force, were entrained by the gas flow and recirculated into the hollow cone. The larger drops, on the other hand, possessed enough inertial force to overcome the effect of drag and maintain their trajectories; they continued traveling radially towards the edge of the spray. The uncertainty bars on the D_{10}, D_{32}, and MMD plots indicate the standard deviations of the mean values for ten repeated measurements.

The U_z profile also shows this recirculation zone in Fig. 5.4(d). The negative U_z values observed near the spray center indicate that the droplets were traveling towards the injector. The transition of negative U_z to positive U_z was observed to occur near radial locations of 10 mm, 15 mm, and 20 mm at measurement planes of 12.7 mm, 25.4 mm, and 38.1 mm respectively, indicating that the hollow cone continued to expand radially as the downstream distance was increased. The spray symmetry was also observed consistently for the A-2 and A-3 fuels, and therefore, the subsequent data presented in this work highlights only the measurements at the positive radial locations for the sake of clarity. The bars on the U_z

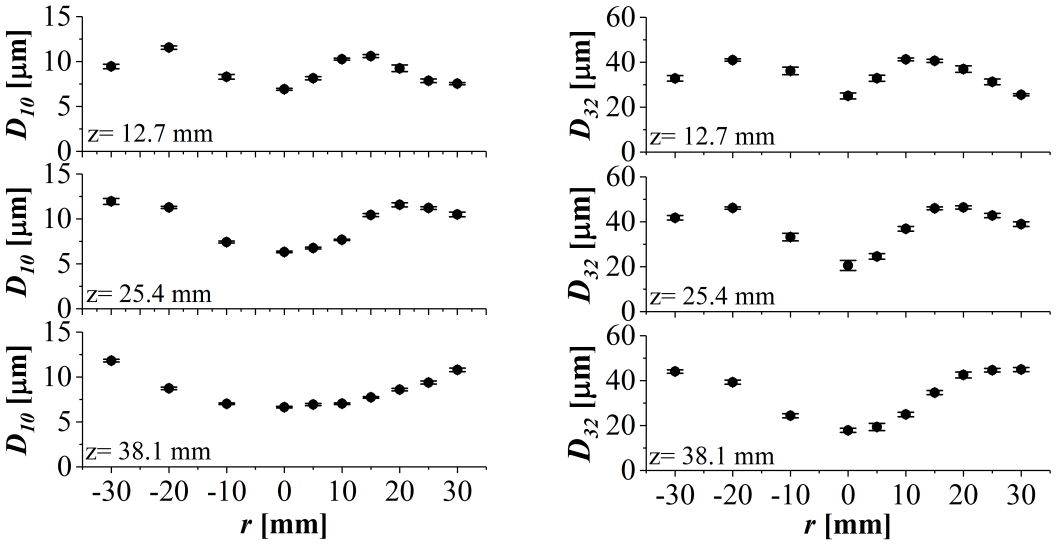

(a) D_{10}

(b) D_{32}

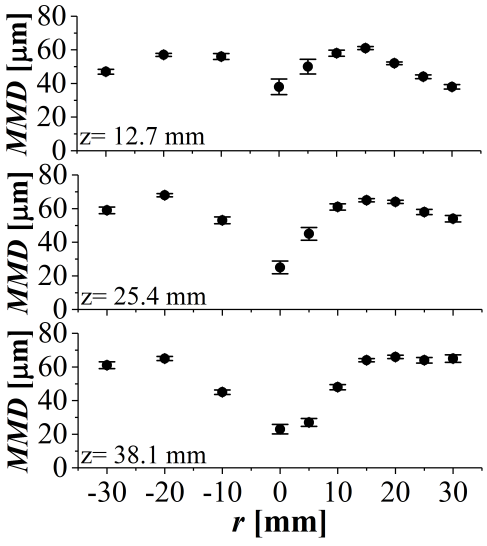

(c) MMD

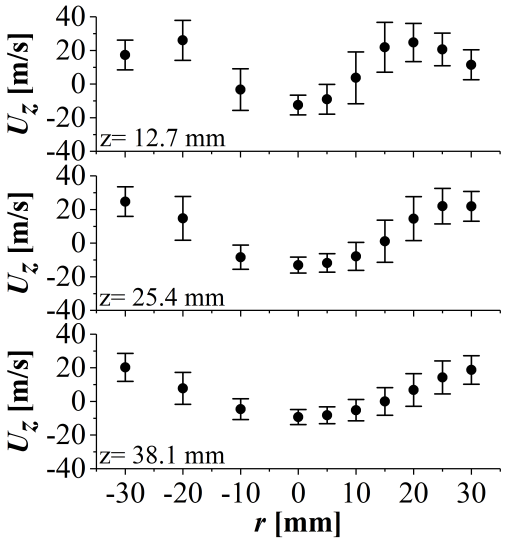

(d) U_z

Figure5.4. Comparisons of mean drop diameters and drop velocities for C-3 on different measurement planes with ΔP_{Pilot} = 1.72 bar, $\Delta P/P$= 3 %, T_{Fuel} = 239 K, T_{airbox} = 239 K.

plots denote the root-mean-squared (RMS) values and indicate the turbulence level in the flow.

Figure 5.5 shows the data rates obtained using the PDA system at each radial location and at the three measurement planes for the C-3 fuel at the baseline condition. A much lower data rate was observed within the hollow cone of the spray due to lower concentration of droplets. The peak rates in each profile indicate the location of the relatively dense fuel stream of the spray were observed at radial locations of $r = \pm$ 20 mm for the $z = 12.7$ mm, $r = \pm$ 25 mm for the $z = 25.4$ mm, and $r = \pm$ 30 mm for the $z = 38.1$ mm measurement planes. This trend is similar to the observed trend for the larger droplets traveling downwards and towards the edge of the spray. Similar trends were also observed for the A-2 and A-3 fuels.

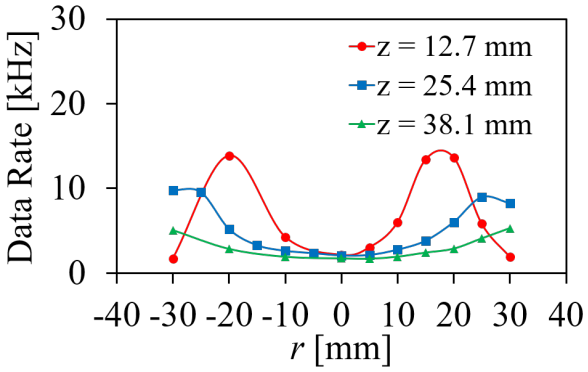

Figure5.5. Data rate profiles at $\Delta P/P = 3\%$, $\Delta P_P = 1.72$ bar, and z = 12.7, 25.4, 38.1 mm for C-3.

Figure 5.6 shows the comparison of the experimental and theoretical interparticle time distribution functions for $\Delta P_{Pilot} = 1.72$ bar, $\Delta P/P = 3$ %, and $r = 20$ mm for the C-3 fuel. Since the number probability density of drop sizes between 1.5 μm and 10 μm was observed to be much higher than the drop size probability density in other drop size ranges, the interparticle time distribution functions for D $\leq 5m$ and D = 10 $\mu m \pm 1$ μm were considered. The P values for both cases were observed to be larger than the significance level of 0.05, and the spray was, therefore, determined to be steady. The uncertainty bars in Fig. 5.6 indicate the expected deviation from the theoretical values.

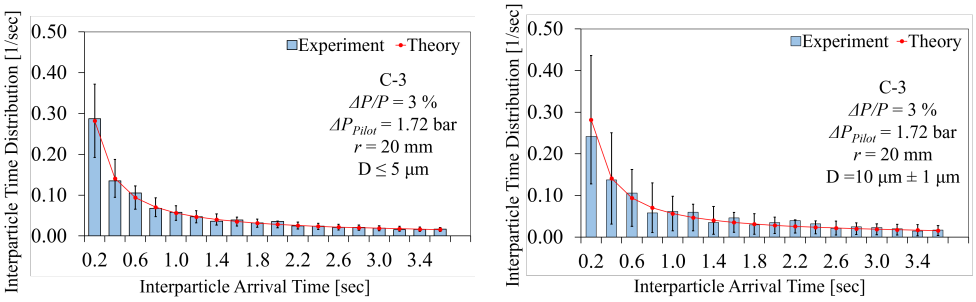

(a) D$\leq 5m$ (b) D = 10 $m \pm 1$ m

Figure5.6. Experimental and theoretical interparticle time distributions for C-3 at $\Delta P/P = 3$ %, $\Delta P_{Pilot} = 1.72$ bar, and $r = 20$ mm

5.3.2 Effect of Fuel Type

The three fuels (A-2, A-3, and C-3) were compared to investigate the effects of fuel properties on D_{10}, D_{32}, MMD, and U_z. Figure 5.7 shows the comparisons of mean drop diameters and axial velocities for the three fuels at $\Delta P/P = 3\%$ at the 25.4 mm measurement plane. As provided in Table 6.5, each of the fuels had different physical properties such as surface tension, viscosity, and density. The surface tension and density of each fuel were identified to differ by only 6% and 2%, respectively. The viscosity, however, differed by 57% between the C-3 and A-2 fuels. Higher liquid viscosity hinders bulk liquid deformation and disintegration through dissipation of the aerodynamic force. The C-3 fuel had the highest viscosity value among the fuels and was expected to form larger droplets. However, it was observed to form the smallest D_{10} and D_{32}. The A-2 fuel, on the other hand, had the lowest viscosity value among the fuels, and the spray had nearly the same D_{10} as the A-3 fuel. The largest D_{32} was observed for the A-3 fuel within the recirculation zone while the A-2 and C-3 fuels formed similar D_{32} in the same region. Then, the A-2 fuel is seen to form slightly larger D_{32} than other fuels near the edge of the spray, but the variations among the fuels were limited. The MMD and U_z measurements showed only minimal variations among the three fuels. These trends were also observed for $\Delta P/P$ of 2 and 4%.

Figure 5.8(a) shows the relation between dynamic viscosity for each fuel and the dimensionless drop sizes (D_{32_o}/d_o and d_D/d_o) from experiment and the prediction from Eq.3.15

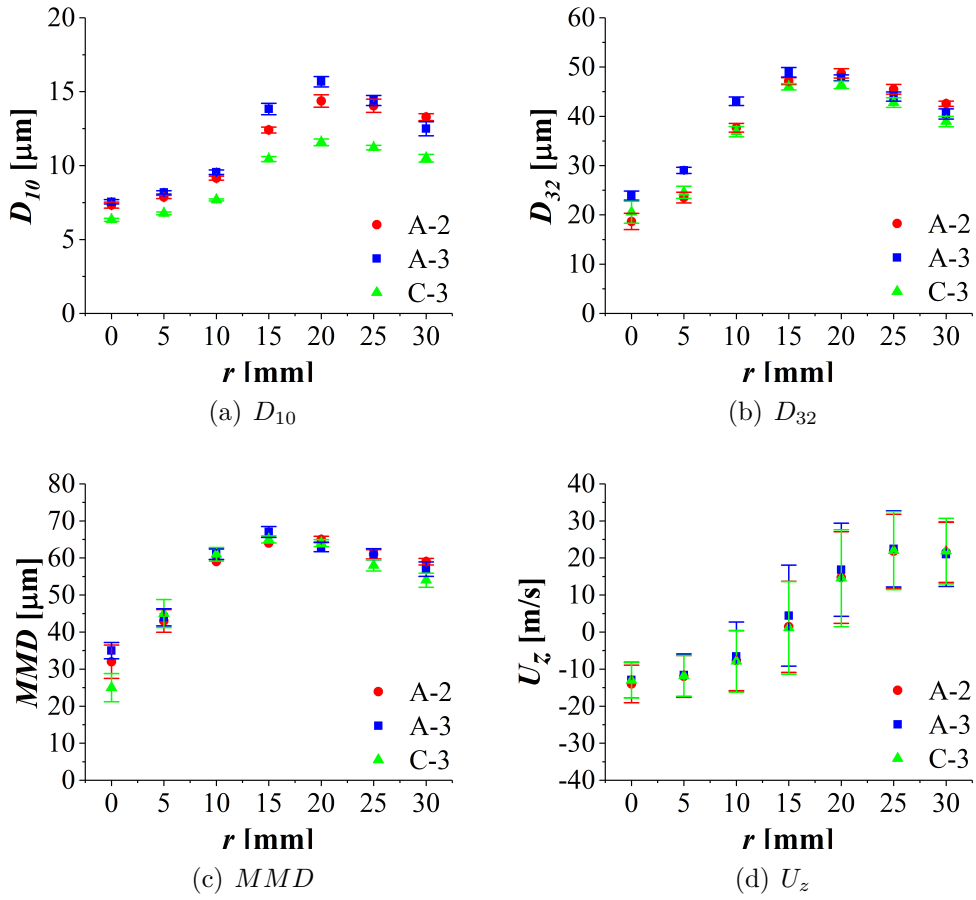

(a) D_{10} (b) D_{32}

(c) MMD (d) U_z

Figure5.7. Comparisons of drop diameters and drop velocities for A-2, A-3 and C-3 at $\Delta P/P = 3$ %, $\Delta P_{Pilot} = 1.72$ bar, $T_{fuel} = 239$ K, and $T_{airbox} = 239$ K for $z = 25.4$ mm.

respectively. The A-2 fuel was found to have the lowest viscosity value, while the C-3 fuel was found to have the highest viscosity value. The dashed lines in Fig.5.8(a) and Fig.5.8(b) represent the predicted dimensionless drop size (d_D/d_o) for each fuel at different ALR values. As shown in Fig.5.8(a), it was observed that the effect of viscosity on the D_{32o}/d_o was not significant. Instead, the measured drop size D_{32o}/d_o was observed to decrease slightly as the viscosity increased. This is due to the dominant effect of surface tension over the viscosity on the drop sizes, as shown in Fig. 5.8(b). The rank of the fuel (high to low) in surface tension was found to be in the order of C-3, A-3, and A-2, which is the opposite rank shown in Fig. 5.8(a). Although the variation in D_{32o}/d_o due to the surface tension

was still small, it was observed that surface tension affected the drop size more even with 6% variation compared to the viscosity, which varied by 60%. The model predicted the drop size d_D/d_o and successfully demonstrated the trend observed in experimental drop size with viscosity and surface tension. If the viscosity solely increases, the model will predict the larger and longer ligament diameter and length. As a result, the value of the ligament term in the denominator of Eq.3.15 will be reduced, and therefore, resulting in larger drop size. However, the surface tension value is also different for each fuel and has a trend opposite to that of the viscosity among fuels. The decrease in surface tension will increase the aerodynamic term in the denominator in Eq.3.15, and thereby, higher effectiveness of the aerodynamic term is believed to dominate the effect of viscosity in the ligament term. This resulted in smaller drop size. Hence, no definitive trend in the drop size was observed with the viscosity. According to Custer *et al.* [**custer1988**], the effect of the viscosity on the mean drop size is minimal at higher values of atomizer ALR, which was 5. For this work, the atomizer had much high ALR values. Furthermore, the variation in the viscosity values was much narrower among fuels compared to Custer *et al.* [**custer1988**], where their viscosity values were differed by orders of magnitude. Moreover, the effect of viscosity was found to be negligible in the prompt atomization when the atomizing gas flow impinges on the liquid at a sufficiently high angle, which is the case for the atomizer used in the present study [**lefebvre1992**].

Figures 5.9 and 5.10 show the cumulative density functions (CDFs) and number probability density functions (PDFs) of the droplet diameters at radial locations of 10, 20, and 30 mm for all three fuels. As shown in Figs. 5.9 and 5.10, C-3 fuel, the highest viscosity fuel, produced more droplets with diameters less than 20 m compared to A-2 and A-3 fuels at all radial locations. This also suggests that the effect of viscosity on the drop size seemed to be negligible in this work. Instead, the surface tension, which acts as a restorable force of liquid, had affected more sufficiently on the drop formation. The comparisons of the velocity PDFs with $\Delta P/P$ variation are shown in Fig. 5.10(b,d,f,h). It was observed that the velocity PDFs of all three fuels were similar at each radial location.

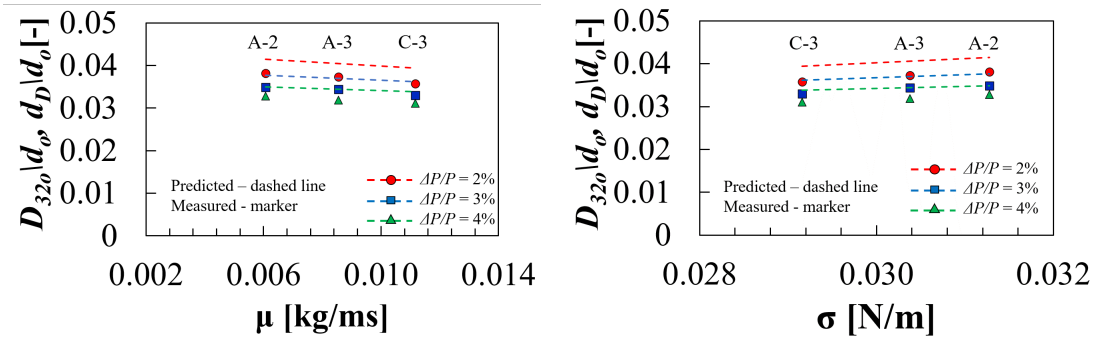

(a) μ vs $D_{32}/d_0, d_D/d_o$ (b) σ vs $D_{32}/d_0, d_D/d_o$

Figure5.8. Relation of fuel dynamic viscosity and surface tension versus the dimensionless drop sizes for experiment and prediction ($D_{32}/d_0, d_D/d_o$) at $\Delta P_{Pilot} = 1.72$ bar, $T_{fuel} = 239$ K, and $T_{airbox} = 239$ K.

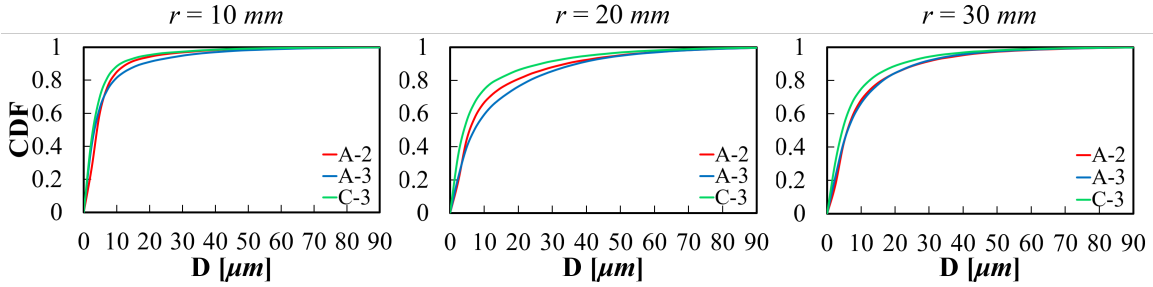

Figure5.9. Comparisons of cumulative density functions (CDFs) for A-2, A-3 and C-3 at $\Delta P/P = 3$ %, $\Delta P_{Pilot} = 1.72$ bar, $T_{fuel} = 239$ K, and $T_{airbox} = 239$ K for $z = 25.4$ mm.

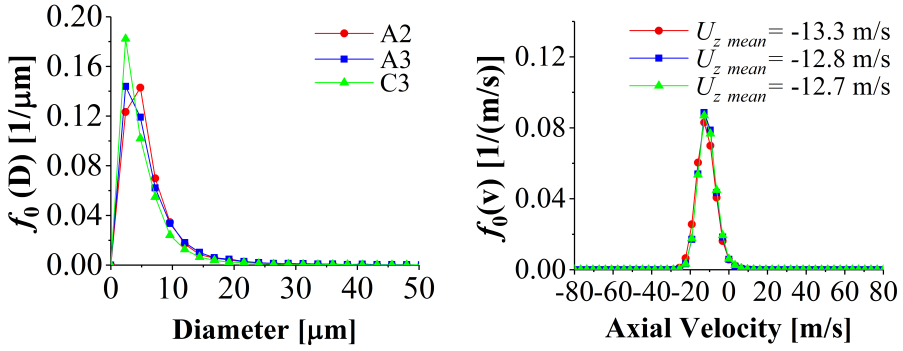

(a) $f_0(d)$ at $r = 0$ mm

(b) $f_0(v)$ at $r = 0$ mm

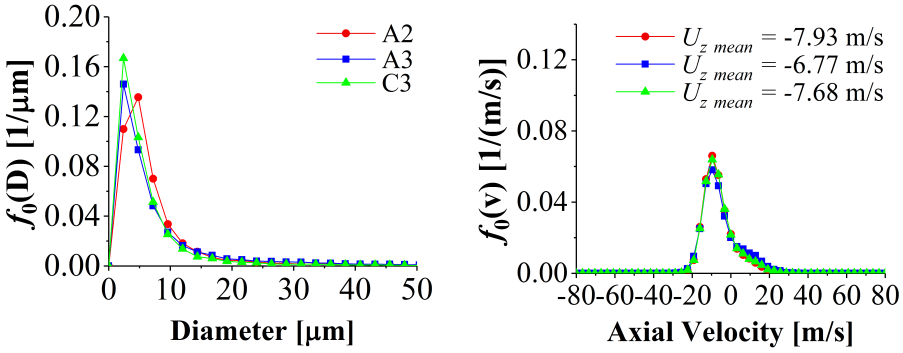

(c) $f_0(d)$ at $r = 10$ mm

(d) $f_0(v)$ at $r = 10$ mm

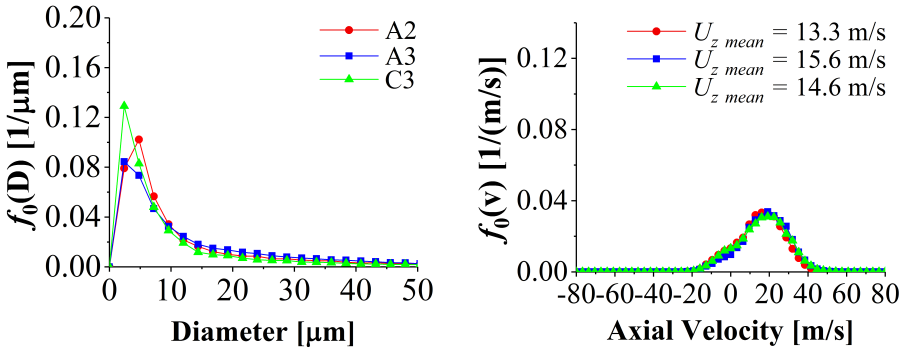

(e) $f_0(d)$ at $r = 20$ mm

(f) $f_0(v)$ at $r = 20$ mm

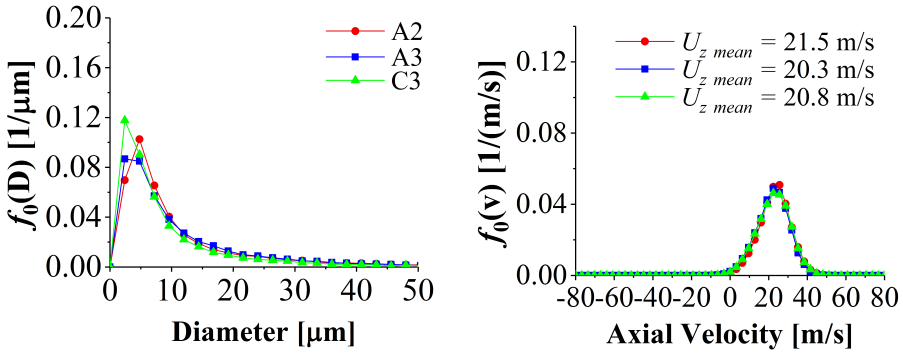

(g) $f_0(d)$ at $r = 30$ mm

(h) $f_0(v)$ at $r = 30$ mm

Figure5.10. Number probability density functions for drop size and axial velocity for A-2, A-3, and C-3 at $\Delta P_{Pilot} = 1.72$ bar, $\Delta P/P = 3$ %, $T_{Fuel} = 238$ K, and $T_{gas} = 238$ K on $z = 25.4$ mm.

5.3.3 Effect of Pressure Drop across the Swirler

The pressure drop across the swirler ($\Delta P/P$) was found to have a significant effect on the parameters D_{32} and U_z for the A-2, A-3, and C-3 fuels. Figure 5.11 shows the spatial distributions of D_{32} and U_z for pressure drops of 2, 3, and 4%, at a constant fuel injection pressure differential ($\Delta P/P$) of 1.72 bar and at the measurement plane of 25.4 mm for all three fuels. The air-to-liquid ratios (ALR) of the atomizer for pressure drop of 2, 3, and 4% were calculated to be 12, 15, and 17, respectively. The drop size D_{32} was observed to decrease significantly as the pressure drop was increased. The mean drop axial velocity, on the other hand, was observed to increase in magnitude with increasing pressure drop. An increase in pressure drop resulted in a higher atomizing gas velocity, which corresponds to greater inertial and aerodynamic forces for the gas flow. This caused an amplification of the hydrodynamic instabilities on the bulk fuel and resulted in smaller droplets. Figure 5.12 shows the relation between ALR and the experimental and theoretical dimensionless drop sizes($D_{32}/d_0, d_D/d_o$). The model correctly predicted the trend of decreasing drop sizes with increasing ALR that was observed experimentally. Moreover, the model also showed the diminishing effect of ALR on the drop size with a further increase in ALR, which was also noted by a number of studies [**lefebvre1989**, **rizkalla1975**, **lefebvre1992**].

5.3.4 Effect of Engine Operating Conditions

The spray characteristics of the A-2 fuel were studied at two different operating conditions: near LBO and cold start conditions. Near LBO conditions correspond to T_{fuel} = 322 K, T_{airbox} = 394 K, and P_{amb} = 2.03 bar, while the cold start conditions correspond to T_{fuel} = 239 K, T_{airbox} = 239 K, and P_{amb} = 1.01 bar. Detailed results at near LBO conditions can be found in Shin *et al.* [**shin2019**]. It should be noted that the direct comparison of relevant parameters is not possible between two conditions since each condition has a different fuel temperature, atomizing gas temperature, ambient gas temperature, and ambient gas pressure. The change in fuel temperature affects the fuel physical properties, while the atomizing gas temperature would also affect the flow velocity, which determines the kinetic energy of the gas flow. The ambient gas temperature and pressure would also affect the

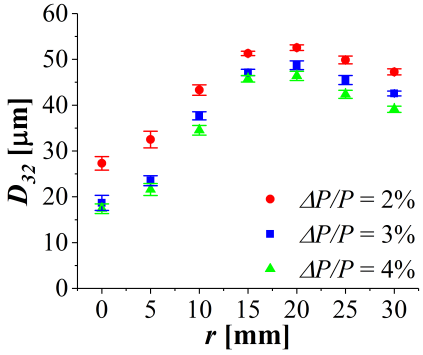

(a) D_{32} for A-2 fuel

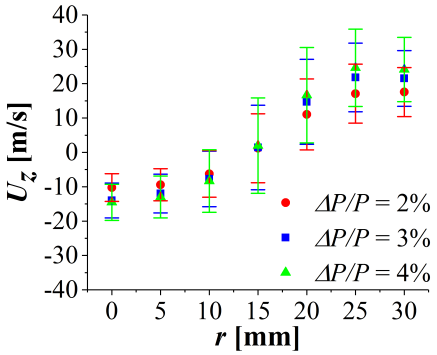

(b) U_z for A-2 fuel

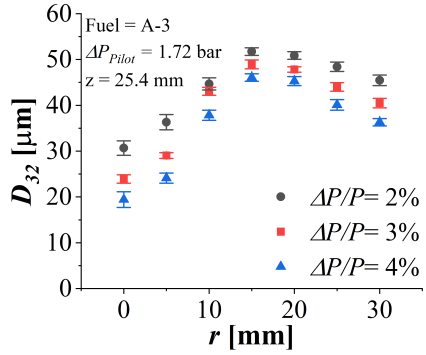

(c) D_{32} for A-3 fuel

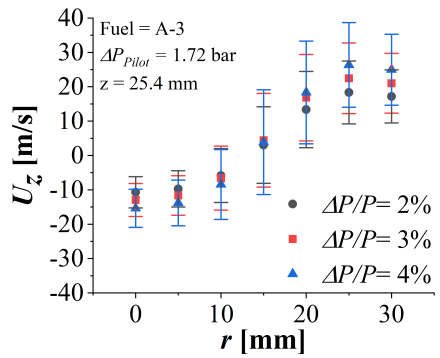

(d) U_z for A-3 fuel

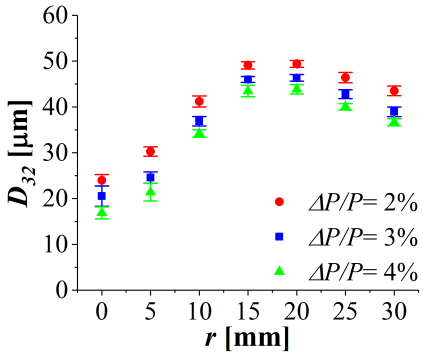

(e) D_{32} for C-3 fuel

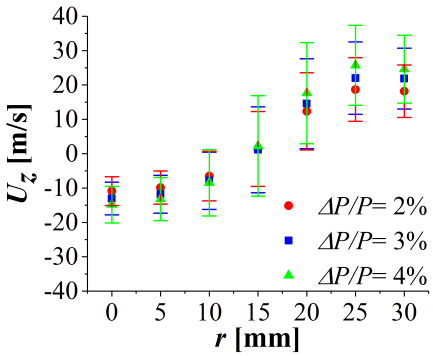

(f) U_z for C-3 fuel

Figure5.11. Comparisons of drop diameters and drop velocities for A-2, A-3, and C-3 at $\Delta P/P$ = 2, 3, 4 %, ΔP_{Pilot} = 1.72 bar, T_{fuel} = 239 K, and T_{airbox} = 239 K for z = 25.4 mm.

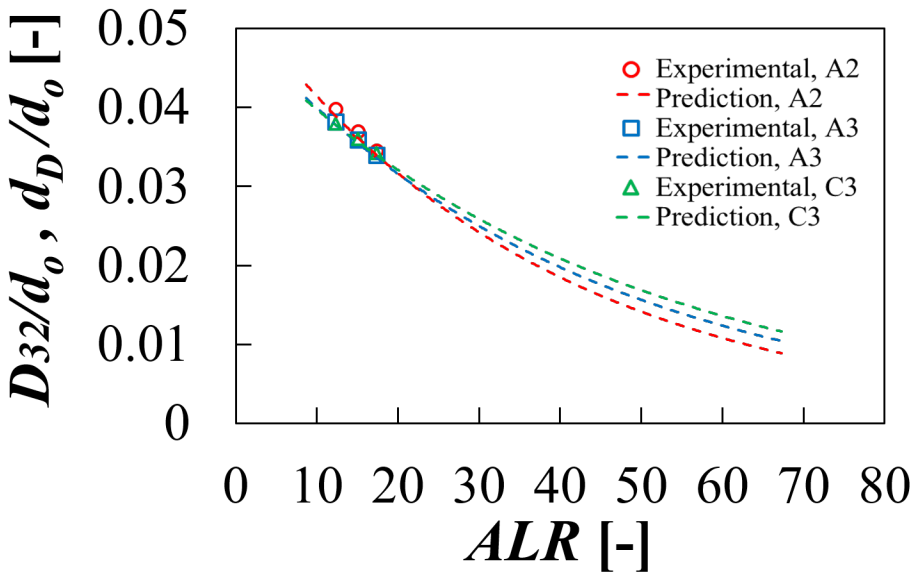

Figure5.12. Comparison of experimental and predicted dimensionless drop sizes ($D_{32}/d_0, d_D/d_o$) as a function of ALR for A-2, A-3, and C-3 at ΔP_{Pilot} = 1.72 bar, T_{fuel} = 239 K, and T_{airbox} = 239 K

atomizing gas velocity, but more importantly, the density of ambient gas. An increase in ambient pressure reduces the D_{32} significantly due to the higher density of the surrounding gas [**zheng1996**]. Further investigation, where each of these parameters is varied independently, would be necessary to determine its effect on the drop size and velocity. Therefore, the purpose of the comparison between two conditions in this section is simply to highlight general observation concerning the changes in drop size and drop velocity.

Figure 5.13 shows the comparisons of D_{32} and U_z for two different operating conditions at $\Delta P/P$ = 3% and ΔP_{Pilot} = 1.72 bar for 25.4 mm measurement plane. The D_{32} values were observed to be significantly larger at the cold start conditions compared to the near LBO conditions. This observation can be attributed to the combination of effects from the increase in fuel viscosity and surface tension due to lower temperature and lower ambient pressure. The increases in viscosity and surface tension due to the lower fuel temperature increased the restorative force of the liquid and viscous damping effects. This resulted in the formation of larger droplets. Although the effect of viscosity was observed to be minimal in the present study, where the viscosity was differed by 60% for the different fuels, the viscosity was 81% higher for cold start compared to LBO conditions. Furthermore, the

surface tension, which observed to have a dominant effect over the viscosity, was varied by 24% higher for cold start than LBO conditions.

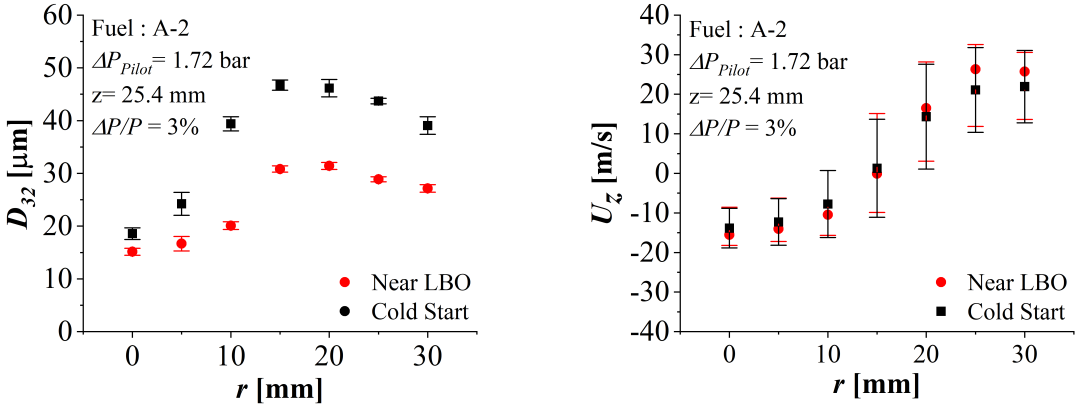

(a) D_{32} (b) U_z

Figure5.13. Comparison of D_{32} and U_z for near LBO and cold start conditions for A-2 fuel at $\Delta P/P = 3$ %, $\Delta P_{Pilot} = 1.72$ bar

The axial velocity U_z at the cold start conditions was observed to be slightly lower than the U_z at near LBO conditions. This can be attributed to the combined effects of different fuel/atomizing gas temperature, drop size, and ambient gas pressure/temperature between the near LBO and the cold start conditions.

Figure 5.14 illustrates the agreement between the measured D_{32_o} and the predicted D_{32} calculated using Eq.3.15 for both near LBO and cold start conditions. The model overestimated the drop size for the cold start and slightly underestimated the drop size for the LBO conditions. These errors may be caused by assumptions that considered in each sub-model. For example, the film formation sub-model was assumed inviscid and neglected drop splash and bound mechanisms and only considered drop spread mechanism. This may resulted in inaccurate film thickness on the surface; in consequence, inaccurate ligament diameter and length may be predicted. The average percentage errors between the predicted and measured drop size were 15% and 3% for the near LBO and cold start conditions, respectively. The correlation coefficient was found to be around 0.97.

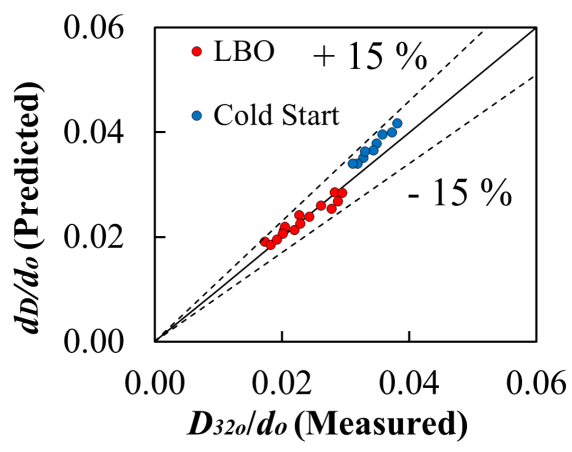

Figure5.14. Measured D_{32_o} versus predicted D_{32} calculated from Eq.3.14

5.4 Summary

The spray characteristics for standard and alternative aviation fuels were investigated at cold start conditions using a hybrid pressure-swirl airblast atomizer. The effect of varying $\Delta P/P$ on the mean drop diameters and velocities was found to be significant, with increasing $\Delta P/P$, resulting in decreased mean drop sizes and increased axial velocities for both the standard and alternative aviation fuels (A-2, A-3, C-3). The investigation at multiple measurement planes showed that the larger droplets maintained their trajectories and continued to travel radially outwards as they traveled downstream from the injector. No definite trend was observed with the viscosity on drop size. Although the surface tension seemed to dominate the effect of viscosity, its drop size variation was not significant due to such a small difference in surface tension value among fuels. From this observation, it can be concluded that no significant difference is in drop size between tested standard and alternative fuels at cold start conditions.

The effect of operating conditions was observed to be significant on the mean drop size. Larger mean drop sizes were observed at cold start compared to that of LBO conditions. This is attributed to the combined effects of higher viscosity and surface tension at lower fuel temperature, resulting in a greater restorative force of the droplet and viscous damping effect, and lower ambient pressure at the cold start compared to LBO conditions.

A phenomenological three-step atomization model, including pressure-swirl spray droplet formation, droplet impingement and film formation, and aerodynamic breakup, successfully demonstrated the trend observed in drop size with the fuel viscosity and surface tension. The model predicted drop sizes as function of ALR, atomizing gas velocity, surface tension, density, and ligament length and diameter within $\pm$ 20% of error for both LBO and cold start conditions. More experimental work is required to validate the model over a wider range of operating conditions and fuel physical properties. Future work includes efforts to investigate the spray structure and dynamics using planar laser-induced fluorescence (PLIF) and Mie scattering. Extending the PDA and PLIF/Mie measurements towards elevated ambient pressure will provide additional insight into the spray characteristics.

6. SPRAY CHARACTERISTICS OF STANDARD AND ALTERNATIVE AVIATION FUELS AT HIGH AMBIENT PRESSURE CONDITIONS

6.1 Introduction

Commercial deployment of any specific alternative jet fuel relies on the approval and issuance of a specification by the American Society for Testing and Materials (ASTM) International and needs to go through the D4054 qualification process [**colket2017**]. This qualification process can be long and expensive since it requires extensive laboratory, combustor rig, and full-scale engine testing of the fuel to assess combustion performance [**colket2017**]. To reduce the cost and time in the qualification process, the National Jet Fuel Combustion Program (NJFCP) has focused on investigating the influence of alternative aviation fuel properties on combustion performance, aiming for developing an advanced computational model to predict full-scale sensitivities of new fuels at realistic aircraft engine combustor conditions. This computational combustor model can be implemented and replace some of the testing requirements in D4054 process, ultimately accelerating the certification process with less cost.

The evaluation of spray characteristics for alternative fuels at realistic gas turbine engine operating conditions is essential since combustion performance is strongly affected by the quality of atomization. Insufficient atomization produces larger droplets, leading to the formation of soot and nitric oxides due to fuel-rich combustion [**lefebvre1989**]. On the other hand, sufficient atomization produces many small droplets, leading to a greater volumetric heat release rate, easier light-up, a wider burning range, and lower pollutant emission [**lefebvre1989**].

In gas turbine combustors, fuel sprays are injected into highly turbulent, swirling, and recirculating streams of reacting gases [**lefebvre1989**]. The pressure and temperature of the ambient gas in the combustor can vary widely depending on engine operability and can strongly affect the fuel atomization. The operating pressure in combustors has been raised continuously in recent years in the quest for better thermal-efficiency. Operational pressures

can even exceed the critical pressure of the liquid fuel [**boyce2011**]. Higher pressure in combustion results in increasing thermal efficiency by improving the specific fuel consumption [**boyce2011**].

Several studies [**batarseh2010**, **becker2004**, **corber2018**, **chaussonnet2019**, **jasuja1981**] investigated the spray characteristics of prefilming airblast atomizer at elevated ambient pressure and temperature. Batarseh *et al.* [**batarseh**] and Chrigui *et al.* [**chrigui2010**] reported a significant reduction in mean drop size with increasing in ambient pressure from 1 to 5 bar, but further increases in ambient pressure increased D_{32}. The axial velocity of the drop, on the other hand, was reported to decrease continuously with the ambient pressure, in both studies. Zheng *et al.* [**zheng1996**] also observed similar trends in mean drop szie and axial velocity with increasing the ambient pressure, but the variation in drop size was small. Zheng *et al.* [**zheng1996**] attributed this to the counter swirling airblast atomizer in which the atomization process is dominated by the liquid sheet breakup mechanism which is independent of pressure. In contrast to those findings in the literature ([**batarseh2010**, **chrigui2010**, **zheng1996**]), other studies [**becker2004**, **corber2018**, **chaussonnet2019**, **jasuja1981**] reported that D_{32} decreased continuously with increasing ambient pressures, beyond 10 atm. However, the reduction in D_{32} was observed to be diminish with a further increase in the ambient pressure. The different observations on the D_{32} trends with increasing ambient pressure between literature may be caused by different nozzle geometry and operating conditions used in their studies. In this work, PDA, PLIF and Mie scattering imaging systems were used to investigate atomization characteristics of alternative fuel (C-5) and compared to those of standard aviation fuel (A-2) at elevated ambient pressure up to 9.5 atm.

The spray cone angle is a vital combustion parameter since the optimum cone angle can lead to better fuel-air mixing and a wider dispersion of fuel drops within the combustor. Zheng *et al.* [**zheng1996**] reported a widening in spray cone angle near the nozzle with increasing ambient pressure from 1 bar to 12 bar; however, the cone angle at further downstream of the spray was remained fairly constant. Besides Zheng *et al.* [**zheng1996**], the studies [**batarseh2010**, **chrigui2010**, **becker2004**, **corber2018**, **chaussonnet2019**, **jasuja1981**] did not provide the effect of ambient pressure on the spray cone angle of the pre-

filming airblast atomizer. In the present study, the spray cone angle of the hybrid pressure-swirl airblast atomizer was investigated using both number of instantaneous Mie images and averaged Mie image were used to investigate the spray cone angle fluctuation at each ambient pressure condition.

Laser sheet imaging techniques were employed in the present study, Planer Laser-Induced Fluorescence (PLIF) and Mie scattering imaging, to obtain a 2-D images of the spray. PLIF is widely used in spray and combustion applications in which knowledge of the concentration of liquid and vapor phase and 2-D measurement of flame and spray are critical. In PLIF [**hanson1990**], a laser sheet illuminates the flow and excites the ground-state molecules of the fluid to a higher electronic energy state. The excited molecules then de-excite and emit light at a longer wavelength. Depending on applications, a fluorescent dye with an appropriate granularity can be added to the fluid or an aromatic hydrocarbon that presents naturally in the fuel can be used as a fluorescent dye [**hanson1990**]. Under certain conditions, the population of these tracer species in a unit volume of the fluid is directly proportional to the fluorescence signal [**hanson1990**, **fansler2015**]. This can be used to obtain information regarding the concentration or mass distribution of the spray [**fansler2015**]. Mie scattering is elastically scattered light from particles similar to or larger than the incident light wavelength. The Mie scattering image also provides a 2-D representation of the spray, but only for the liquid phase of the spray. Using both PLIF and Mie scattering images, the distribution of the liquid and vapor phases in the spray can be determined since the PLIF signal can be detected from both liquid and vapor phases.

In this work, the aromatics in jet fuel were the species that fluoresced. Orain *et al.* [**ordain2014**] investigated the fluorescence spectroscopy of kerosene vapor at high temperature and pressure by comparing excitation wavelengths of 266, 248, 282, and 308 nm in nitrogen. Orain *et al.* [**ordain2014**] observed that the fluorescence intensity was stronger for 248 nm and 266 nm excitation resulting from a strong absorption of the laser by the aromatics at these wavelengths. It was concluded that the excitation at 266 nm was the most promising scheme for the aromatic fluorescence for kerosene. Furthermore, Orain *et al.* [**ordain2014**] found that the variation in kerosene fluorescence excited by 266 nm wavelength in nitrogen was minimal with ambient pressure at a constant temperature. Suto

[**suto1992**] also observed the fluorescence signals from benzene and naphthalene, which are also aromatic molecules in jet fuels, at 240 – 280 nm and at 190 – 295 nm, respectively. Therefore, a Nd:YAG laser tuned to 266 nm excitation wavelength was used in the present work for the fuel-PLIF measurement.

Building upon an earlier study at near LBO conditions [**shin2019**], the spray characteristics of standard and alternative fuels at high ambient pressure conditions were investigated using phase Doppler anemometry (PDA) and fuel-PLIF/Mie imaging in this present work. The ambient pressure was varied to 1, 2, 3, 4, 5, and 9.5 bar at fuel temperature,T_{fuel} = 332 K, atomizing gas temperatureT_{airbox} = 394 K, fuel injection pressureΔP_{pilot} = 1.72 bar, and pressure drop across the gas swirler$\Delta P/P$ = 3%. The spray characteristics considered in this study include the Sauter Mean Diameter (D_{32}), drop axial velocity (U_z), and cone angle (θ) for standard fuel (A-2) and alternative fuel (C-5). The same hybrid pressure-swirl airblast (HPSA) atomizer as the previous work [**shin2019**] was used in this study.

6.2 Experimental System

6.2.1 Test Rig

The Purdue Variable Ambient Pressure Spray (VAPS) test rig shown in Fig. 6.1(a) is capable of creating conditions over a wide range of pressures and temperatures of ambient gas, atomizing gas, and fuel for spray measurements. The VAPS rig has two major components: the airbox and the pressure vessel. The airbox is a length of pipe inside the vessel and allows the atomizing gas flow to be isolated from the vessel flow. This creates a pressure difference between the airbox and the pressure vessel. The flow in the airbox exits through the gas swirler of the hybrid pressure-swirl airblast atomizer, which is mounted at the exit of the airbox.

The pressure vessel has four optical windows. The window orientation has been modified and is different than one from the previous study [**shin2019**] . For the present work, three 127 mm windows are oriented perpendicular to each other, and a 76.2 mm window is oriented at 60 from one of the 127 mm windows as shown in Fig. 6.1(b). The heated (394 K) nitrogen flow was separated into three lines and supplied directly into the airbox, vessel, and

the window purge flange. The purpose of the window purge flow was to minimize the fuel wetting on the window by creating an N_2 flow shield near the window surface. These heated flows also prevented condensation on the outer side of the windows. The fuel temperature was measured just upstream of the prime injector inlet port, while the pressure in the pilot fuel line was measured at the inlet of the airbox.

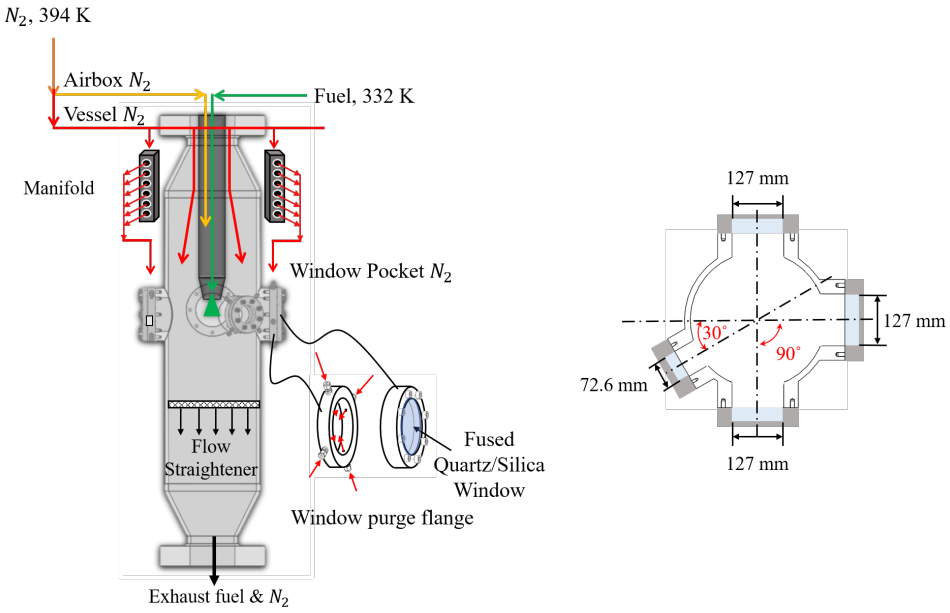

Figure6.1. Schematic diagram of the VAPS pressure vessel with nitrogen flows. (a) vessel, airbox, window purge, and fuel flows in the VAPS rig (b) the window orientation on the pressure vessel.

6.2.2 Atomizer

The hybrid pressure-swirl airblast atomizer designed by the Parker-Hannifin Corporation was used in this study. A schematic diagram of the atomizer's internal view and resulted in spray behavior is shown in Fig.6.2. The atomization process using only the pilot fuel nozzle in the hybrid atomizer involves: (1) the hollow cone fuel spray resulted from the pilot nozzle impinges on the prefilming surface, (2) a fuel film develops along the surface and thickens towards the prefilmer tip, (3) the ligaments are formed as the fuel film extends from the prefilmer tip, (4) the swirling gas flow disintegrates the ligaments into droplets.

Some droplets resulting from primary breakup experiences secondary atomization in the bag breakup regime, resulting in a multiplicity of drop sizes [**sforzo2019**]. A detailed discussion on this hybrid atomizer can be found in Mansour *et al.* [**mansour2003**].

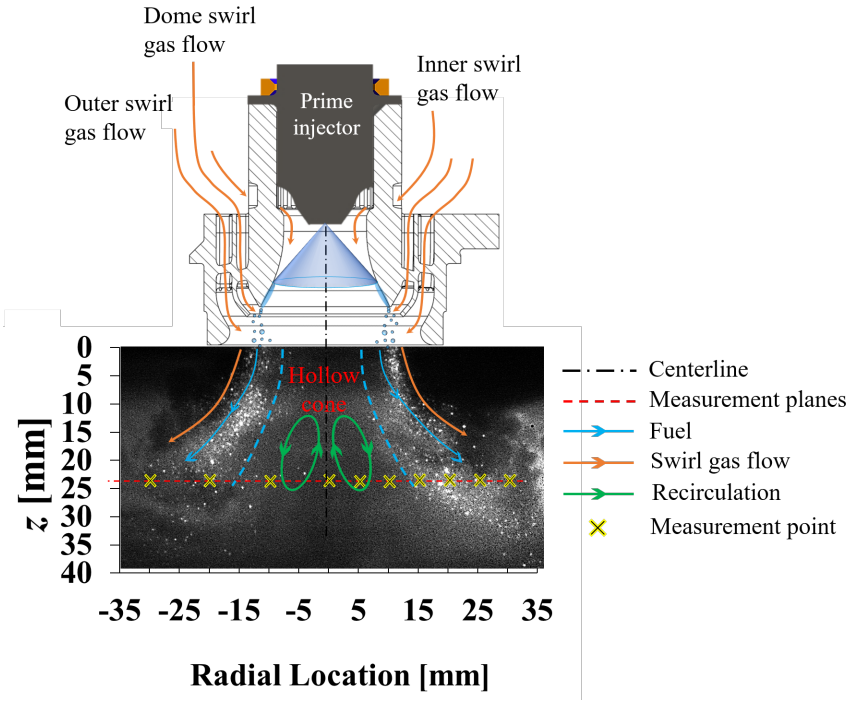

Figure6.2. Schematic diagram of internal view of the atomizer and resulted spray behavior in a hybrid pressure-swirl airblast atomizer [**mansour2003**]

6.2.3 Diagnostic Techniques

Planar Laser Induced Fluorescence and Mie Scattering

Simultaneous Planar Laser Induced Fluorescence (PLIF) and Mie scattering measurement were performed to provide a 2-D visualization of the spray. Figure 6.3 shows the schematic diagram of the PLIF and Mie measurement system in the VAPS rig. Q-switched Nd:YAG laser was tuned to 266 nm using 2nd and 4th harmonic generators. This excitation light beam profile was expanded to 40 mm in height and collimated into a cylindrical lens to form a sheet, entering the pressure vessel through the fused silica window. The laser with a power of approximately 70 mJ/pulse had illuminated the spray at a 10 Hz repeti-

tion rate. The fluorescence spectrum of kerosene and 1,2,4 trimethyl benzene are shown in Fig.6.4 [**ordain2014**, **ordain2010**]. The A-2 (Jet-A) was found to have the same aromatic compounds as kerosene (JP-8), such as alkyl-benzene and alkyl-naphthalenes [**ordain2014**, **edwards2017**], while C-5 fuel was found to have 1,2,4 trimethyl benzene as its aromatic compounds [**edwards2017**]. The fluorescence of each fuel and scattered light with 266 nm incident beam then were separated by the dichroic beam splitter, which reflected 266 nm scattered light and transmitted the fluorescence above 266 nm. Two synchronized ICCD cameras (PI-MAX4) equipped with UV lenses (Nikkor 70 210mm f/4.5 and Objectif UV 100 f/4.5), captured the scattered light and fluorescence from fuel. For the PLIF camera, a transmission filter centered at 320 nm with a bandpass of 40 nm were used to capture the fluorescence spectra. This scheme captures the entire emission range for Jet-A and almost half of the fluorescence range for C-5 fuel. Although some fluorescence at 270 nm may transmitted through the 266 nm bandpass filter, for the Mie signal camera, that contribution of fluorescence signal was negligibly small.

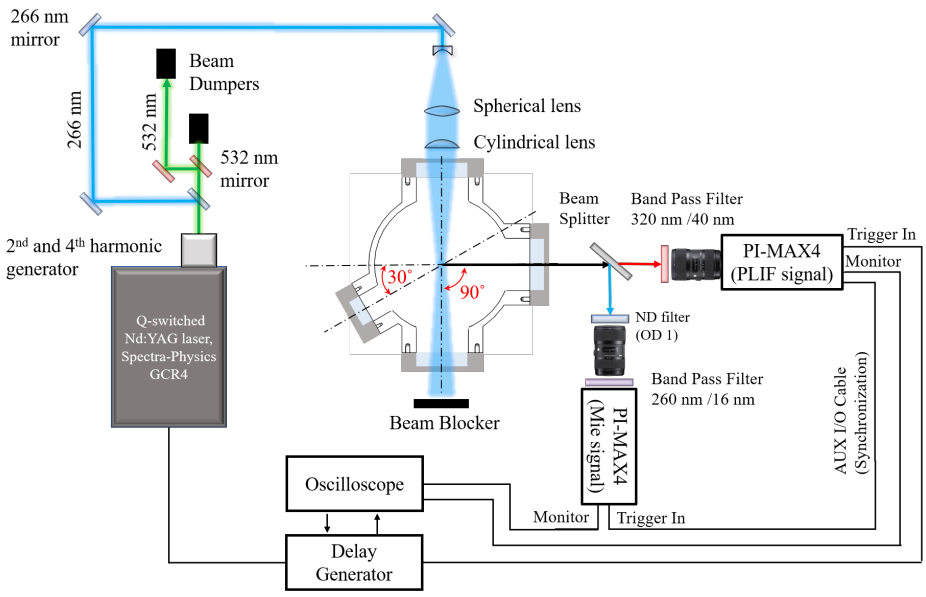

Figure6.3. Schematic diagram of the PLIF and Mie measurement system in the VAPS rig

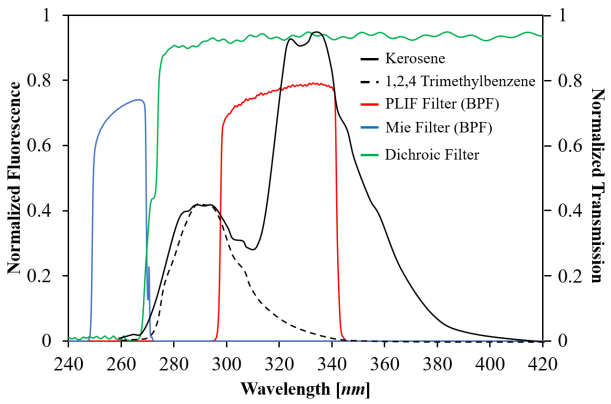

Figure6.4. Emission wavelength of fuels with 266 *nm* excitation wavelength [**ordain2014**, **ordain2010**] and optical filters configuration

Phase Doppler Anemometry

A phase Doppler anemometry (PDA) system was used to measure the droplet diameter and droplet velocity . The phase difference of Doppler-burst signals, from different detectors, determines the droplet diameter, while the frequency of Doppler-bursts determines the droplet velocity. The fundamentals of the PDA measurement system can be found in references such as Albrecht *et al.* [**albrecht2003**]. The PDA system relative to the VAPS rig is shown in Fig.5.3. The same PDA system previously used for the LBO and engine cold start measurements [**shin2019**, **shin2021**] was also used, except for a different scattering angle. The scattering angle was set to 30 in this study due to window orientation. Measurements were performed at spatial locations between ±30 mm from the spray center in increments of 5 mm. The translation of the PDA system was constrained within ±30 mm intervals due to interference from the mounting flange of the 76.2 mm window. Ten measurements, each, with 20,000 samples were recorded at each radial location (r) per test condition. The validation and spherical validation rates were in the range of 95 97% and 88 95%, respectively. The key optical settings for the PDA measurement are shown in Table . The uncertainties for the PDA measurements, listed in Table 6.2, were obtained using the standard deviations of ten repeated measurements at each radial location.

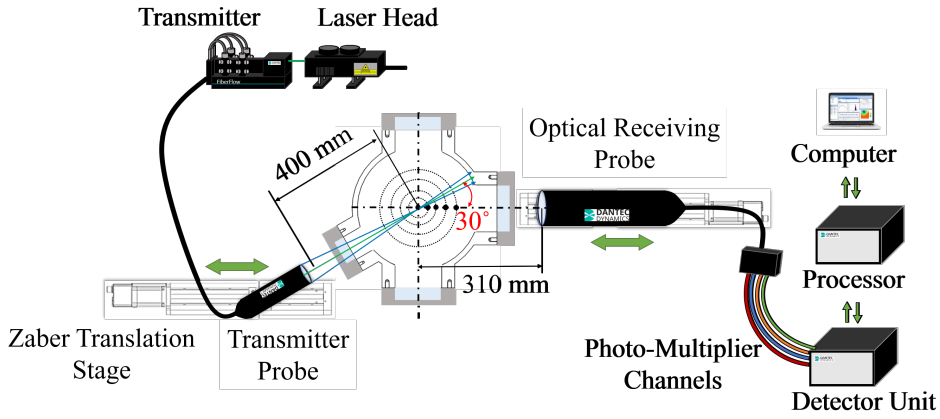

Figure6.5. Schematic diagram of the PDA system relative to the VAPS rig

Table6.1. Optical setting for PDA system

Aperture mask	Mask A
Spatial filter	Slit 200 m
Scattering angle	30
Receiver optic lens	f 310 mm
Transmitter optic lens	f 400 mm

Table6.2. Uncertainties for PDA measurement

r [mm]	**U**(D_{32})	**U**(U_z)
30	1.6 %	1.2 %
25	1.4 %	0.7 %
20	1.4 %	2.3 %
15	1.5 %	4.2 %
10	2.7 %	4.0 %
5	2.8 %	2.2 %
0	3.6 %	1.2 %

6.2.4 Test Conditions

The high ambient pressure conditions were defined here as following: vessel pressure $P_{vessel} = 1$, 2, 3, 4, 5, 9.5 bar, fuel temperature$T_{fuel} = 332$ K, atomizing gas temperatureT_{airbox} of 394 K, and fuel injection pressure$\Delta P_{pilot} = 1.72$ bar, pressure drop across the gas swirler$\Delta P/P$ = 3%,. The fuel injection pressure is defined as the pressure differential between the fuel line and the vessel. AtΔP_{pilot} 1.72 bar, mass flow rate measured by Coriolis flowmeter was 2.52 g/s. The pressure drop across the gas swirler denotes the pressure difference between the airbox and the vessel. At $\Delta P/P = 3\%$, the calculated gas velocity at the exit of swirler was 82 m/s. The measurement plane, axial distance (z) downstream from the swirler exit plane, was set at 25.4 mm for the PDA measurement. The uncertainty of each operating parameter is shown in Table 3, following the approach of Kline *et al.*[**kline1953**].

Table6.3. Uncertainties of Operating Parameters

Operating Parameters	Operating Conditions	Uncertainty
P_{vessel}	1,2,3,4,5,9.5 Bar	0.4 %
$\Delta P/P$	3%	2.8 %
T_{fuel}	332 K	4.2 %
ΔP_{pilot}	1.72 Bar	2.5 %
T_{airbox}	394 K	1.1 %
$\dot{m}_{fuel}$	2.5 g/s	2.5 %

6.3 Fuels

Jet-A (A-2) and C-5 were investigated in this study. The standard aviation fuels are represented by the code A while the alternative fuels are represented by the code C [**colket2017**]. The A-2 fuel was found to be a "nominal fuel" based on three combustion-related properties selected by the OEM: flash point, viscosity, and aromatics content [**colket2017**]. The C-5 fuel was created by blending 1,3,5 trimethyl benzene with a C10 isoparaffinic solvent. This test fuel has an extremely flat boiling range at roughly 165C [**colket2017**]. Detailed discussions regarding physical properties, chemical compositions, and fuel selection method can be found in Colket *et al.* [**colket2017**].

Table shows the key physical properties of each fuel, such as surface tension, viscosity, and density. These properties were extrapolated at a fuel temperature of 332 K using measured values provided by the Air Force Research Laboratory (AFRL)[**edwards2017**] The viscosity, surface tension, and density values of the C-5 fuel were found to be different from A-2 by 53%, 15%, and 4.7%, respectively.

Table6.4. Fuel physical properties at 332 K. The data points were extrapolated using measured values provided by AFRL [**edwards2017**]

Fuel Type	Temp.	μ	σ	ρ	Notable Characteristics
A-2	332 K	9.2E-4	0.023	770	Average flash point, viscosity, aromatics
C-5	332 K	4.4E-4	0.020	734	Flat boiling range (boils at 165C)

6.4 Results and Discussion

6.4.1 Effect of Ambient Pressure on Drop Diameter and Drop Velocity

The spray characteristics of the standard (A-2) and alternative (C-5) fuels were investigated using Sauter Mean Diameter (D_{32}) and drop axial velocity (U_z). The symmetrical nature of the spray was consistently observed for both fuels, and therefore only half of the spray data obtained from PDA is presented. Figure6.6 shows the comparisons of D_{32} and U_z at P_{vessel} = 1,2,3,4,5, and 9.5 bar for the baseline condition corresponding to$\Delta P/P$ = 3%,ΔP_{pilot} = 1.72 bar,T_{fuel} = 332 K, andT_{airbox} = 394 K at z = 25.4 mm. As reported in the previous study [**shin2019**], the spray generated from the hybrid pressure-swirl airblast atomizer in this study was observed to be a hollow cone, which was the region observed within radial locations of ±10 mm in the spray.

The effect of ambient pressure (P_{vessel}) was found to affect the mean drop size significantly. As shown in Fig., a significant decrease in D_{32} was observed with increased ambient pressure from 1 bar to 2 bar. The D_{32} continued to decrease gradually with further increases in the ambient pressure from 2 bar to 9.5 bar. However, the effect of ambient pressure on drop diameters diminished with further increase in ambient pressure, and a minimal decrease in D_{32} value was observed when the ambient pressure increased from 5 bar and 9.5 bar. Furthermore, the droplets across the radial locations was observed to be monodisperse at

higher ambient pressure. The inertial force on the liquid sheet and ligament increases with the increasing density of the ambient gas. This raises the growth rate and wavenumber of disturbance on the liquid sheet and ligament resulted in smaller droplets [**decorso1960**].

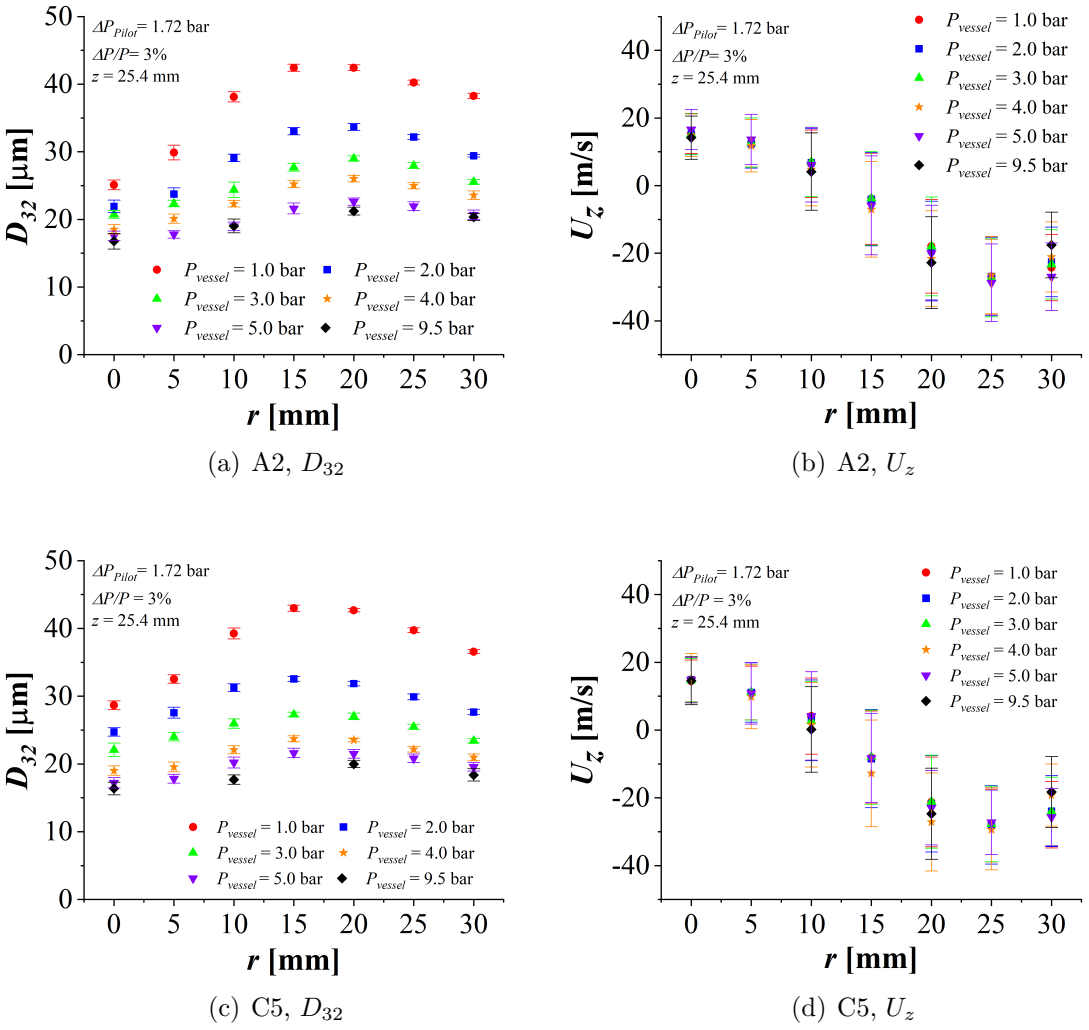

(a) A2, D_{32} (b) A2, U_z

(c) C5, D_{32} (d) C5, U_z

Figure6.6. Comparisons of drop diameters and drop velocities for A-2 and C-5 fuels at P_{vessel} = 1,2,3,4,5, and 9.5 bar, $\Delta P/P$ = 3%, ΔP_{Pilot} = 1.72 bar, T_{Fuel} = 332 K, and T_{airbox} = 394 K for z = 25.4 mm

The drop size probability density functions (PDFs) and cumulative density functions (CDFs) at each ambient pressure are shown in Fig. for C-5 fuel. The PDFs and CDFs were observed to shift towards the smaller drop diameter range with increasing ambient pressure. The number of smaller drop diameters increased with increasing P_{vessel} while the number of

larger drop diameters decreased at higher P_{vessel} for both radial locations of 0 and 20 mm. This observation supports the trend of decreasing in D_{32} with increasing P_{vessel}. Moreover, it can be seen that greater number of smaller droplets present at the spray center (r=0 mm) compared to those number near the spray edge (r = 20 mm).

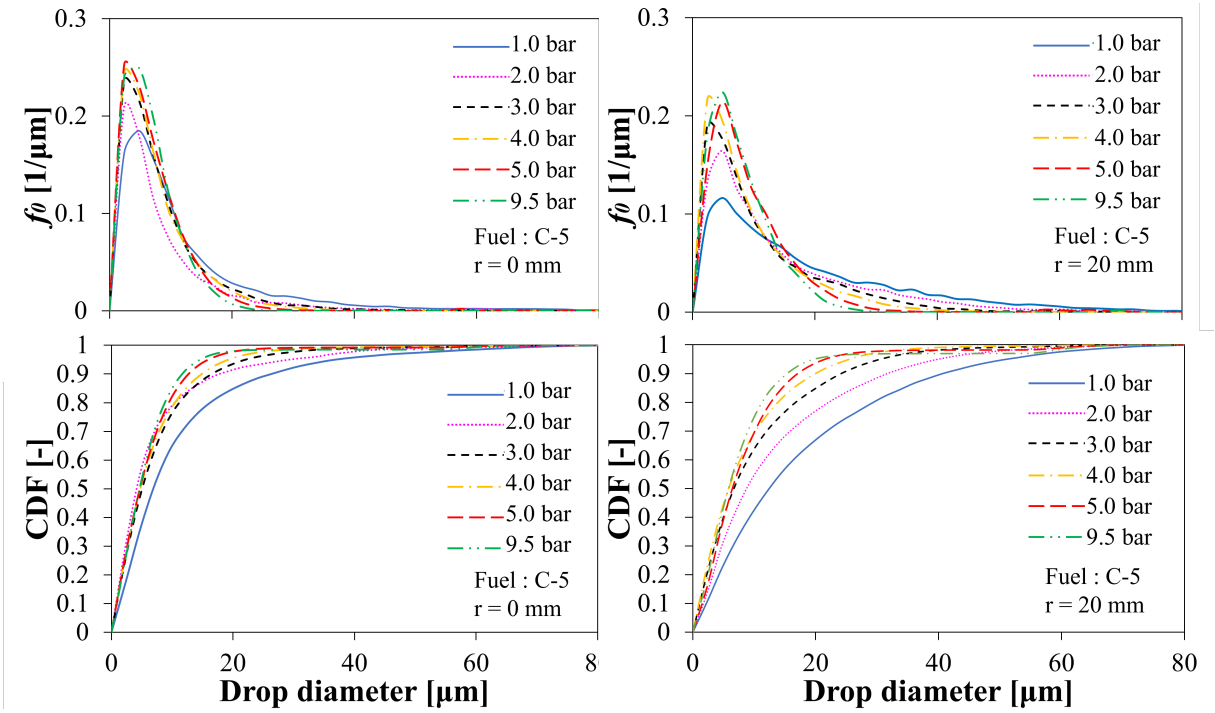

(a) PDFs and CDFs at r = 0 mm

(b) PDFs and CDFs at r = 20 mm

Figure6.7. Comparison of number probability density functions and cumulative density function for C-5 fuel at P_{vessel} = 1,2,3,4,5, and 9.5 bar, $\Delta P/P$ = 3%, ΔP_{Pilot} = 1.72 bar, T_{Fuel} = 332 K, and T_{airbox} = 394 K for z = 25.4 mm

Figure 6.8 shows the effect of pressure drop across the swirler ($\Delta P/P$) on D_{32} and U_z at P_{vessel} = 5 bar for A-2 fuel. The pressure drop was varied to values of 2, 3, and 6% atΔP_{pilot} = 1.72 bar,T_{fuel} = 332 K,T_{airbox} = 394 K, and z = 25.4 mm. As shown in Fig.6.8(a), the D_{32} decreased with increasing$\Delta P/P$ and tend to be mono-disperse across the radial locations at higher$\Delta P/P$. The drop axial velocity was observed to increase with increasing $\Delta P/P$ as shown in Fig.6.8(b).

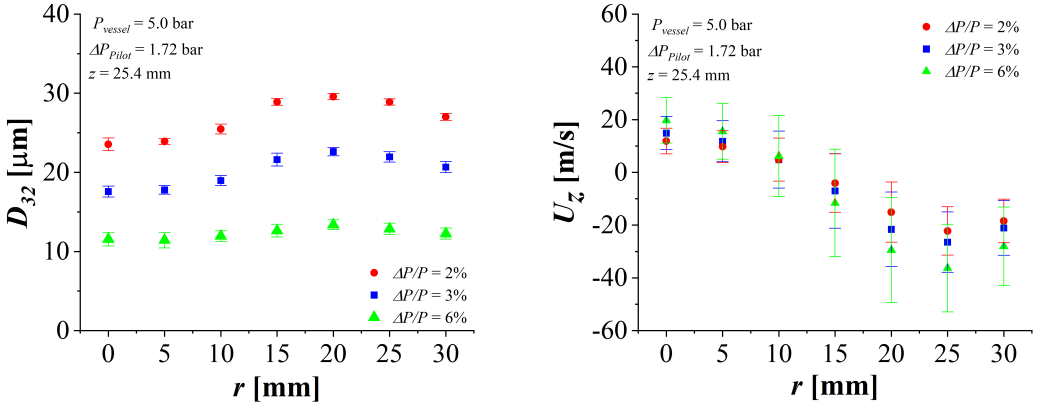

(a) D_{32} (b) U_z

Figure6.8. Comparisons of drop diameters and drop velocities for A-2 fuel at $\Delta P/P$ = 2,3,and 6%, P_{vessel} = 5 bar, ΔP_{Pilot} = 1.72 bar, T_{Fuel} = 332 K, and T_{airbox} = 394 K for z = 25.4 mm

6.4.2 Laser Sheet Spray Measurement

Fuel-PLIF and Mie scattering images were taken at 5 Hz for both A-2 and C-5 fuels at P_{vessel} = 1, 2, 5, and 9.5 bar,$\Delta P/P$ = 3%,ΔP_{pilot} = 1.72 bar,T_{fuel} = 332 K, andT_{airbox} = 394 K. Figure6.9 shows the normalized instantaneous and averaged PLIF and Mie images at P_{vessel} = 2 and 9.5 bar for A-2 fuel. For the averaged images, 200 images were used. From the instantaneous images shown in Fig.6.9(a), more droplets were observed in the hollow cone region at higher ambient pressure. This is attributed to increase number of smaller droplets at higher ambient pressure as observed in PDA measurement. These smaller droplets tend to recirculated into the hollow cone region. Also, this increase in number of smaller droplets causes greater number of scattering events, and thereby increase the signals in Mie and PLIF images at higher ambient pressure. The averaged PLIF and Mie from Fig.6.9(b) also shows that the signals in the hollow cone region increased with ambient pressure.

The laser sheet drop sizing (LSD) technique [**yeh1993**, **sankar1999**, **legal1999**] was used to obtain D_{32} map of a plane of the spray using the PLIF and Mie scattering images. Laser absorption and laser sheet corrections were not required since the PLIF and the Mie scattering images were obtained simultaneously on identical ICCD cameras. In order to

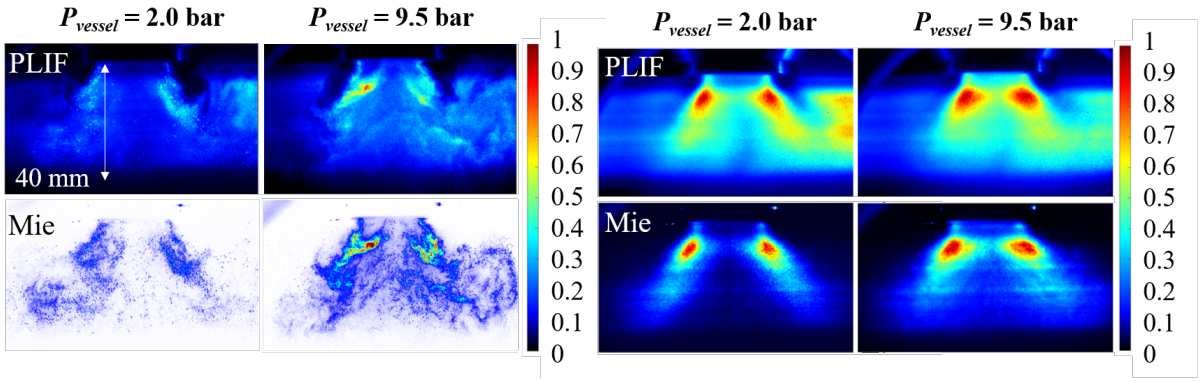

(a) Normalized instantaneous Images (b) Normalized averaged Images

Figure6.9. Instantaneous and averaged PLIF and Mie images at P_{vessel} =2 and 9.5 bar, $\Delta P/P$ = 3%, ΔP_{Pilot} = 1.72 bar, T_{Fuel} = 332 K, and T_{airbox} = 394 K for A-2 fuel

match the field of views, a cross-correlation was performed between the instantaneous PLIF and Mie images, by identifying the pixel locations of the observable droplets on both images. Averages of 200 PLIF and 200 Mie images were overlapped to obtain the ratio of LIF and Mie signals. The signal dependence on the laser spatial profile was canceled by the ratio. As shown in Fig., the ratioed LIF and Mie image was used to obtain estimated D_{32} maps for P_{vessel} = 1, 2, 5, and 9.5 bar cases [**jermy2000**, **stojkovic2001**, **kannaiyan2016**].

The LIF/Mie signal ratio and measured drop size by measured PDA system at z = 25.4 mm and at P_{vessel}= 1 bar were used to get the drop size calibration (Fig. 6.10(a)). This calibration was applied to the D_{32} map and was used to calculate D_{32} values at different ambient pressure conditions. In the present work, the LIF and Mie signals were not found to be proportional to the volume (D^3) and surface area (D^2) of the droplet. Therefore, the calibration curves shown in Fig. 6.10(a) were found to be not following the typical trend of increasing LIF/Mie ratio with increasing drop size [**corber2018**, **mishra2014**, **mishra2017**, **kannaiyan2016**], but showed an opposite trend.

This is attributed to multiple scattering [**berrocal2008**, **powell2007**] and high aromatic concentration in the fuel [**domann2001**, **richard2020**, **pastor2002**]. Multiple scattering is a phenomenon in which a Mie photon scatters off several other droplets before reaching the CCD/ICCD camera sensor. These multiple scattering paths of photons can lead to a

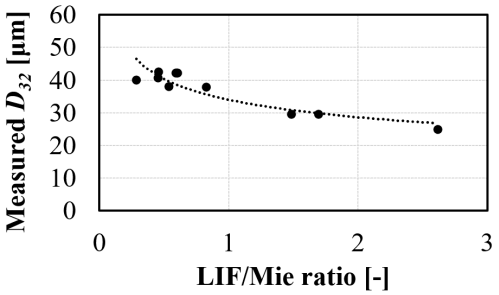

(a) Calibration curve at P_{vessel} = 1 bar

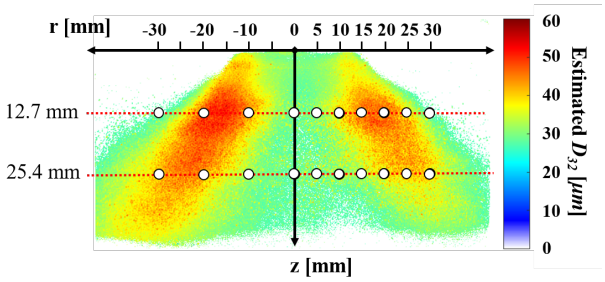

(b) Estimated D_{32} map for P_{vessel} = 1 bar

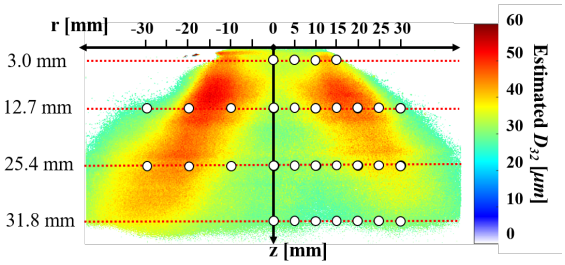

(c) Estimated D_{32} map for P_{vessel} = 2 bar

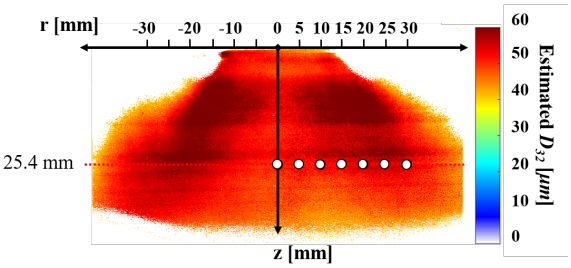

(d) Estimated D_{32} map for P_{vessel} = 5 bar

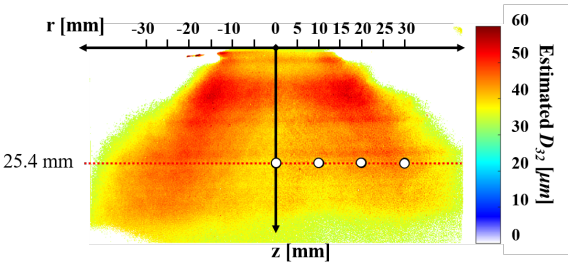

(e) Estimated D_{32} map for P_{vessel} = 9.5 bar

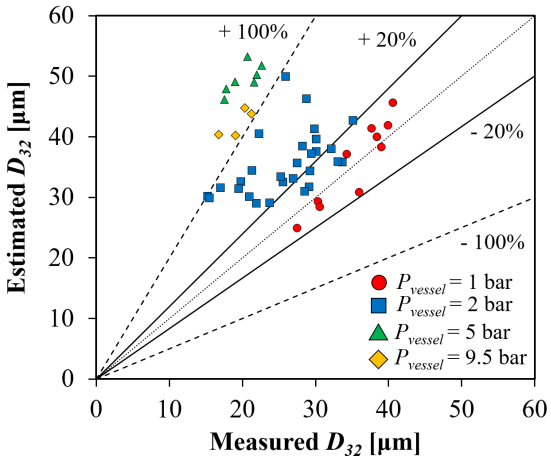

(f) Validation of estimated D_{32} at each P_{vessel}

Figure6.10. Calibration curve and estimated D_{32} map using LSD technique for P_{vessel} = 1, 2, 5, and 9.5 bar cases.

misinterpretation of the droplet size. In addition, the photons may not reach the camera sensor due to multiple scattering [**richard2020**]. This leads to a loss in the Mie signal. The LIF signal may be absorbed or scattered by intervening droplets or vapor phase. A high concentration of aromatic or fluorescent dye in the liquid will increase the re-absorption and lead to incomplete internal reflection path with in the droplet. This resulted in deviating the LIF signal's proportionality to the volume of droplets [**domann2001**, **domann2003**].

It was also discovered that the drop size calibration obtained from one ambient pressure condition was not applicable to other ambient pressure conditions, as shown in Figs. 6.10(c)6.10(d)6.10(e). The calibration curve for each ambient pressure conditions was observed to be different and have two different measured D_{32} values were found for an identical LIF/Mie ratio value. It is believed to be due to the fact that the scattering signal scales with the number density of particles [**laufer1996**]. As shown in Fig.6.7, the number of smaller droplets increased with increasing ambient pressure at a constant fuel flow rate, resulting in increased total number of droplets. Thus, the scattering signal scaled differently at each ambient pressure, resulting in different calibration factors for each ambient pressure case. Figure 6.10(f) shows the comparison between estimated D_{32} and measured D_{32} for each ambient pressure case. The percentage of deviation from measured D_{32} values increased over 100% at higher ambient pressure.

Therefore, the Structured Light Illumination Planar Imaging (SLIPI) technique is suggested to suppress the multiple scattering effectively in LSD measurement for more accuracy [**mishra2014**, **mishra2017**, **kulkarni2019**]. Furthermore, it can be suggested to use the fluorescence dye to control its concentration in LSD measurement, rather than the aromatic contents presented in the fuel [**domann2001**, **domann2003**].

6.4.3 Effect of Ambient Pressure on Cone Angle

The full cone angle was estimated using 200 instantaneous Mie images at each ambient pressure condition. As shown in Fig.6.11(a), the spray boundaries in each instantaneous image were defined using the Canny edge detection method [**canny1986**]. A threshold was set to include most of droplet clusters in the spray boundaries for each ambient pressure

condition. The angle between two lines along the outer spray boundaries was estimated as a full spray cone angle. Figure 6.11(b) provides the estimation of full cone angle (2θ) at P_{vessel} = 1, 2, 5, and 9.5 bar near z = 6 mm and z = 25.4 mm for A-2 and C-5 fuels. The dashed lines indicate the linear trends of cone angle measurements at each ambient pressure.

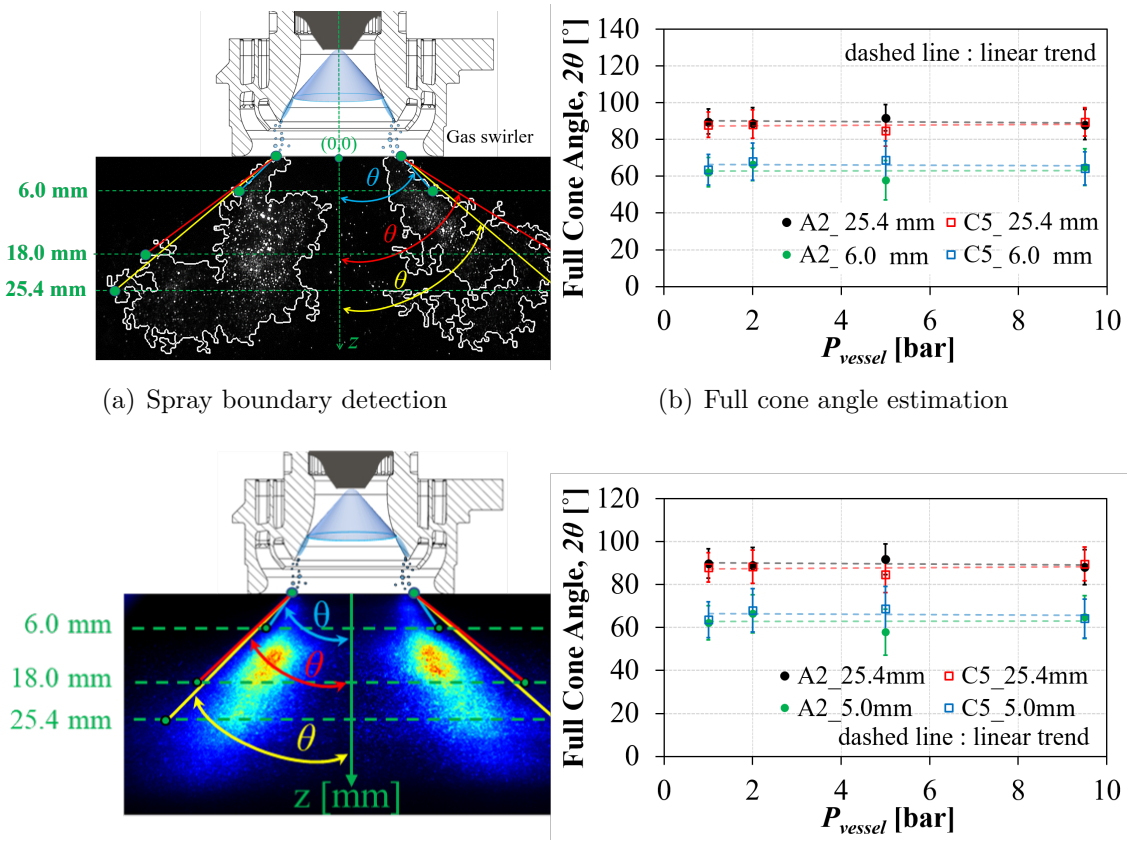

(a) Spray boundary detection

(b) Full cone angle estimation

(c) Spray boundary detection

(d) Full cone angle estimation

Figure6.11. Full cone angle estimations for A-2 fuel at $\Delta P/P$ = 3%,ΔP_{pilot} = 1.72 bar,T_{fuel} = 332 K, andT_{airbox} = 394 K. (a) spray boundary detection using Mie images (P_{vessel} =1 bar case) (b) cone angle estimation at z = 6 mm and 25.4 mm.

The cone angle estimation at z = 6 and 25.4 mm shows that the effect of ambient pressure on the spray cone angle was minimal for both fuels. Since the swirler pressure drop ($\Delta P/P$) was set at constant at each ambient pressure condition, it appears that the spray was able to penetrate and reach to similar axial distance and generate similar cone angle. The fluctuations of the cone angle near z = 6 mm and 25.4 mm were observed to be similar, and those values were found to be ± 8°and ± 9° at z = 6 mm and 25.4 mm respectively

for both A-2 and C-5 fuels. The values for angle fluctuation are the standard deviation of estimated spray cone angles from 200 instantaneous images at each pressure condition.

Full cone angle at z = 18 mm was observed to increase with increasing ambient pressure as shown in Fig.6.12. This is attributed to entrainment of smaller droplets near the spray edge. At higher ambient pressure, the number of smaller droplets increased. These smaller droplets usually respond quickly to the gas flow due to their less inertia. By following the gas flow, smaller droplets are entrained and traveled back up to upper measurement plane such as z =18 mm. The number of entrainment event increases at higher ambient pressure with increasing number of smaller droplets. This resulted in increase in cone angle with increasing ambient pressure at z=18 mm. The entrainment of smaller droplets is observed in instantaneous Mie images at P_{vessel} = 9.5 bar and can be found in the Fuel Liquid/Vapor Distribution section.

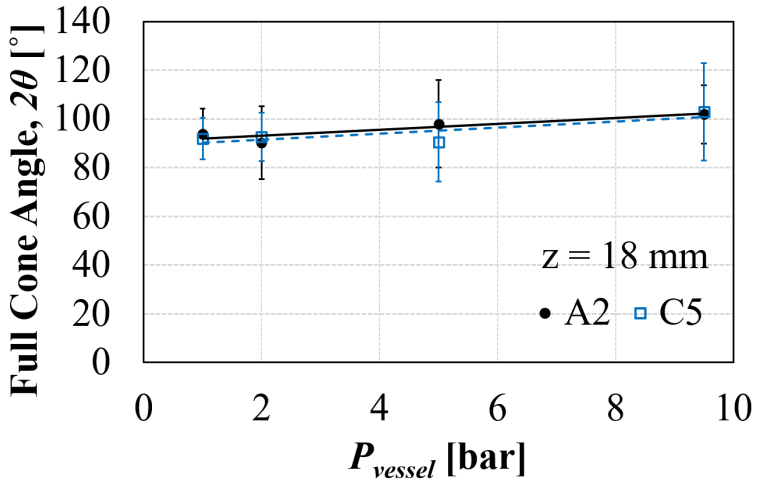

Figure6.12. Full cone angle estimations for A-2 and C-5 fuels at z = 18 mm using instantaneous Mie images

6.4.4 Fuel Liquid/Vapor Distribution

The liquid and vapor discrimination analysis was performed following a similar approach used by Andersson *et al.* [**andersson2011**]. Figure6.13 shows pairs of simultaneously captured PLIF (left) and Mie (middle) images and the normalized difference image from PLIF

and Mie images at P_{vessel} = 1, 2, and 9.5 bar. Both PLIF and Mie images were divided by the peak intensity value. The differences of images were calculated by subtracting the Mie image from the PLIF image. The linear normalization was done on the difference image to obtained the normalized difference image in scale of 0 to 1, as shown in Fig.6.13(c)(f)(i).

In this comparison, it should be noted some factors affect the PLIF and Mie signals differently. Ideally, the Mie scattered light signal is proportional to the surface area of the droplets, whereas the LIF signal is proportional to the volume of the droplets [**yeh1993**]. However, this hypothesis was not valid in the present work, as also demonstrated in other studies [**charalampous2011**, **zaller2000**, **domann2001**, **domann2003**]. This will influence the LIF and Mie light signals differently where the droplets have different sizes depending on the location in the spray. Another factor to consider is the multiple scattering, so called diffuse scattering, within the spray [**linne2013**]. Diffuse scattering from droplets on the periphery of the spray can be absorbed by the droplets near the centerline and converted to fluorescence. The presence of signal inside of the hollow cone region in the spray, as shown in Fig.6.13(a)(d)(g), is likely caused by diffuse scattering from near the laser sheet plane [**berrocal2008**, **powell2007**]. This multiple scattering was observed to be relatively stronger for the PLIF image. Thus, the comparison between the Mie and LIF images presented in this section is non-quantitative. However, it can be a useful approach to identify and distinguish liquid and vapor in the spray.

From Figure6.13(b)(e)(h), it is evident that the number of droplets near the spray center increased at higher ambient pressure. This is believed to be due to an increased number of smaller droplets at higher ambient pressure, as observed from droplet PDF comparison in Fig.6.7. Figure6.14 shows the data rate of PDA measurement at each radial location for C-5 fuel. The data rate near the center of the spray increases significantly with increasing ambient pressures. This observation supports that a significant number of smaller droplets are recirculated into the hollow cone region and also increase the number of scattering events and signals by increasing the surface area (D^2) [**zelina1998**]. Smaller droplets at P_{vessel} = 9.5 bar seem to respond quickly to the gas flow compared to those observed at lower P_{vessel}, as shown in Fig.6.13(c)(f)(i). This resulted an increase in cone angle at z = 18 mm with increasing ambient pressure.

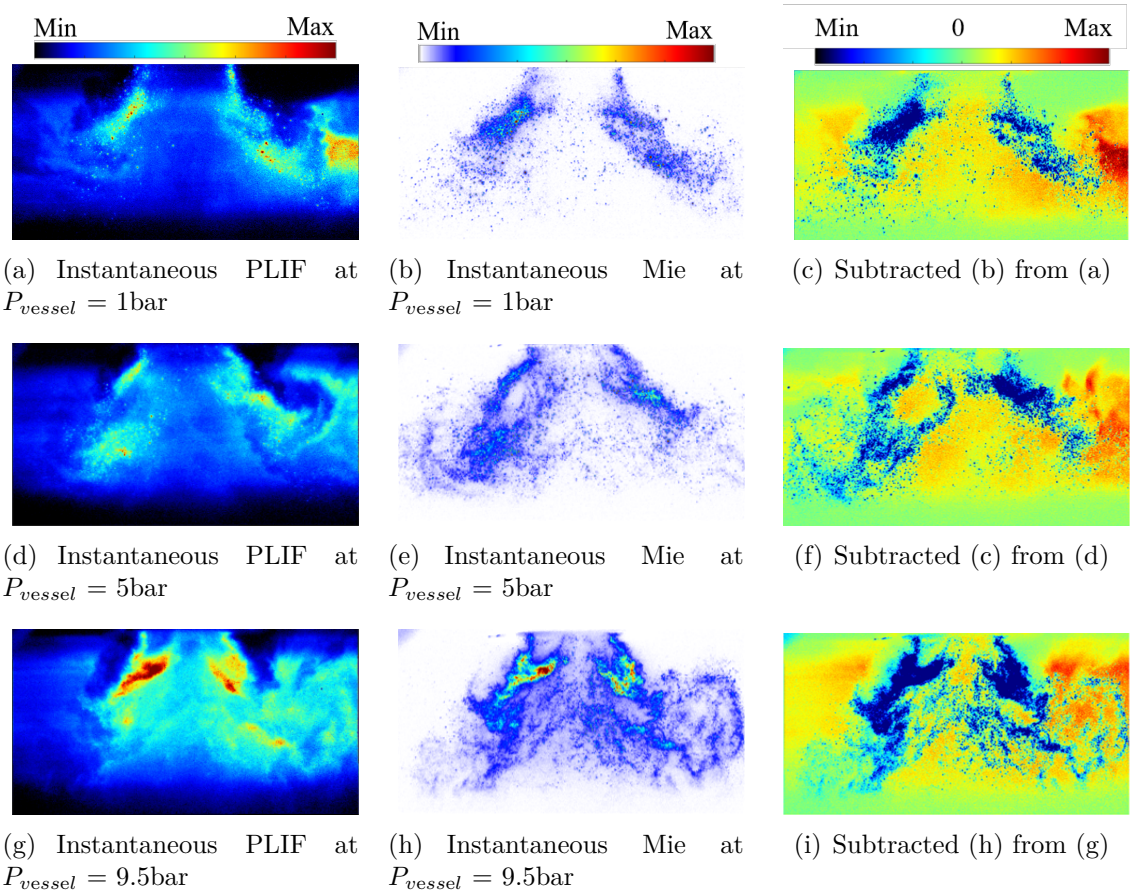

(a) Instantaneous PLIF at P_{vessel} = 1bar

(b) Instantaneous Mie at P_{vessel} = 1bar

(c) Subtracted (b) from (a)

(d) Instantaneous PLIF at P_{vessel} = 5bar

(e) Instantaneous Mie at P_{vessel} = 5bar

(f) Subtracted (c) from (d)

(g) Instantaneous PLIF at P_{vessel} = 9.5bar

(h) Instantaneous Mie at P_{vessel} = 9.5bar

(i) Subtracted (h) from (g)

Figure6.13. Liquid – vapor discrimination A-2 fuel at P_{vessel} = 1, 2, and 9.5 bar,$\Delta P/P$ = 3%,ΔP_{pilot} = 1.72 bar,T_{fuel} = 332 K, andT_{airbox} = 394 K.

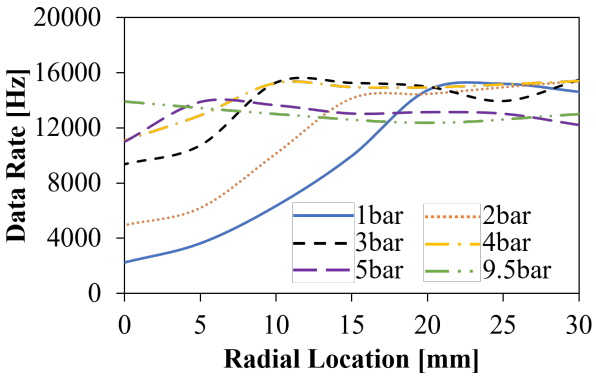

Figure6.14. Comparison of data rate measurement from PDA at each ambient pressure for C-5 fuel

6.5 Drop Size Prediction

Drop sizes at each ambient pressure condition were predicted using the semi-empirical model provided in Chapter 3. Figure6.15 shows the predictions of essential parameters from each sub-model, such as the pressure-swirl spray drop size (d_{Dp}/d_o), fuel film thickness (t_f/d_o), and its flow velocity (U_{film}) on the prefilming surface, ligament diameter (d_{L2}/d_o), and ligament length (λ_{L2}/d_o) using Eq.3.14. In this section, these parameters were non-dimensionalized using the pilot nozzle orifice diameter (d_o). As shown in Fig.6.15(a), the droplet diameter from the pressure-swirl spray were predicted to decrease with increasing ambient pressure. Increasing in inertial force of gas flow due to higher ambient gas density causes the growth rate and wavenumber of disturbance on the liquid sheet to increase. This resulted in smaller droplet diameter from the pressure-swirl spray. Due to the smaller droplet size at higher ambient pressure, the thickness of the film formed on the prefilmer surface was predicted to become thinner as the ambient pressure increases, as shown in Fig.6.15(b). Moreover, the film flow velocity was predicted to be increased as the film became thinner based on the continuity since the fuel mass flow rate was set to be constant. The ligament diameter and length were also predicted to decrease with increasing ambient pressure, as shown in Fig.6.15(c)(d). The ligament diameter is the function of film thickness and wavenumber of the film. At higher ambient pressure, the wavenumber of the film increases as the growth rate of disturbance on the film rises due to the higher density of gas

flowing along with the film. Hence, the ligament diameter was predicted to decrease with increasing ambient pressure. Similarly, a higher growth rate of disturbance on the ligament with a higher wavenumber of the ligament caused the ligament length to be decreased with increasing ambient pressure.

The comparisons of dimensionless predicted (d_D/d_o) and measured drop sizes (D_{32o}/d_o) for A-2 and C-5 fuels are shown in Fig. 16 for $\Delta P/P$ = 3%, ΔP_{pilot} = 1.72 bar, T_{fuel} = 332 K, T_{airbox} = 394 K, and z = 25.4 mm. The orifice diameter of the pilot nozzle (do) was used for this dimensionless quantity. The diminishing effect of ambient pressures on the drop size was observed for both A-2 and C-5 fuels. Moreover, it can be observed that the A-2 drop size are slightly larger than for C-5 fuel. The percentage difference in dimensionless measured drop sizes (D_{32o}/d_o) between A-2 and C-5 fuels was 1% at P_{vessel} = 1 bar and 17% at P_{vessel} = 9.5 bar. This difference is believed to be due to the higher viscosity and surface tension of A-2 fuel compared to those of C-5 fuel, as shown in Table. Higher liquid viscosity and higher surface tension hinder bulk liquid deformation and disintegration through dissipation of the aerodynamic force by increasing the restorative force of the liquid and viscous damping effects [**lefebvre1989**, **rizkalla1975**]. This resulted in larger droplets for the A-2 fuel.

The model predicted drop sizes at P_{vessel} = 1, 2, 3, 4, and 5 bar within ± 10 % and drop sizes at P_{vessel} = 9.5 bar with approximately 20% error compared to experimental data. Although the model was improved in predicting the drop size at higher ambient pressure by implementing the correlation of pressure-swirl spray cone angle variation [**dodge1986**], more experimental work is needed for a better demonstration of drop size trend at high ambient pressure.

Figure6.17 shows the comparison of predicted and measured dimensionless drop sizes for A-2 fuel at$\Delta P/P$ = 2, 3, and 6%, P_{vessel} = 5 bar,ΔP_{pilot} = 1.72 bar,T_{fuel} = 332 K, and T_{airbox} = 394 K for z = 25.4 mm. The model predicted the drop size at different$\Delta P/P$ within 10% error. Although the model successfully demonstrated the drop size trend observed with $\Delta P/P$ variation at P_{vessel} = 5 bar, more experimental data point with wider range of pressure drop would be needed to validate the model at higher pressure drop.

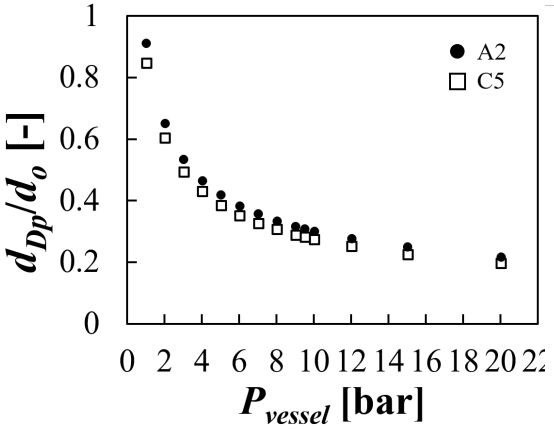

(a) Predicted pressure-swirl spray drop size

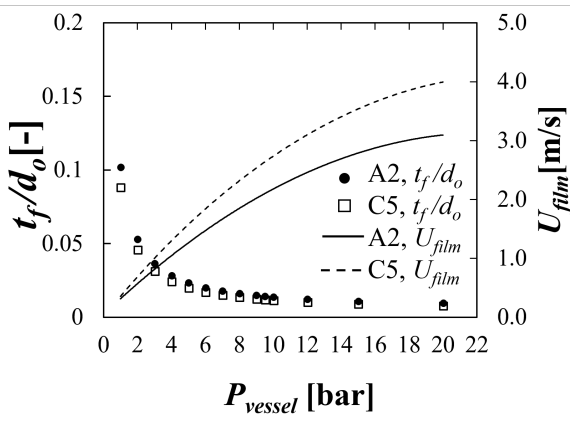

(b) Predicted film thickness and velocity

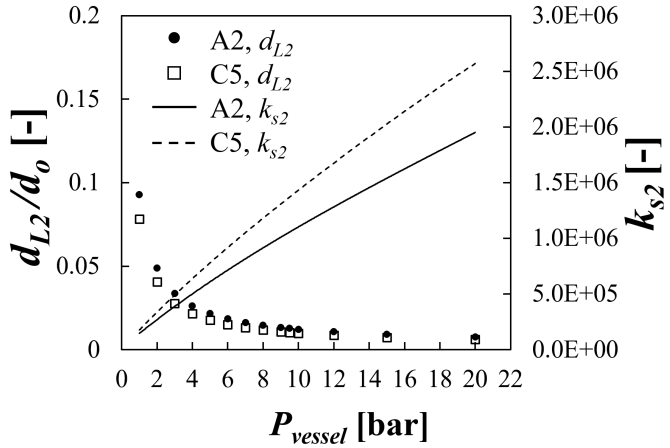

(c) Predicted ligament diameter and film wavenumber

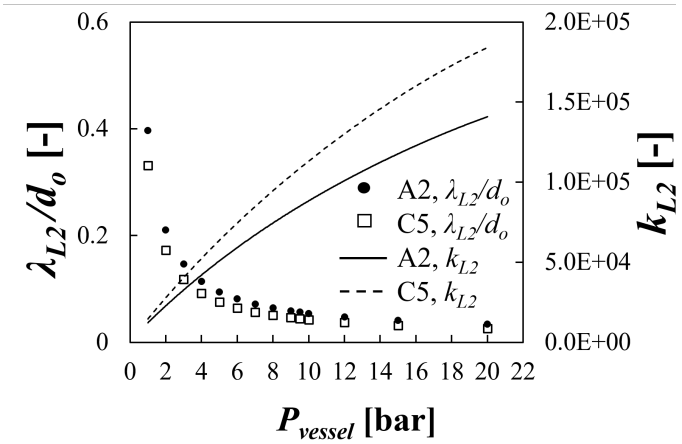

(d) Predicted ligament length and ligament wavenumber

Figure6.15. Predictions for the pressure-swirl spray drop size (d_{Dp}), film thickness on the prefilmer surface (t_f), film velocity (U_{film}), and ligament diameter (d_L), film wavenumber (k_{dL}), ligament length (λ_L), and ligament wavenumber ($k_{\lambda L}$). The model predicted these parameters at$\Delta P/P$ = 3%,ΔP_{pilot} = 1.72 bar,T_{fuel} = 332 K, andT_{airbox} = 394 K.

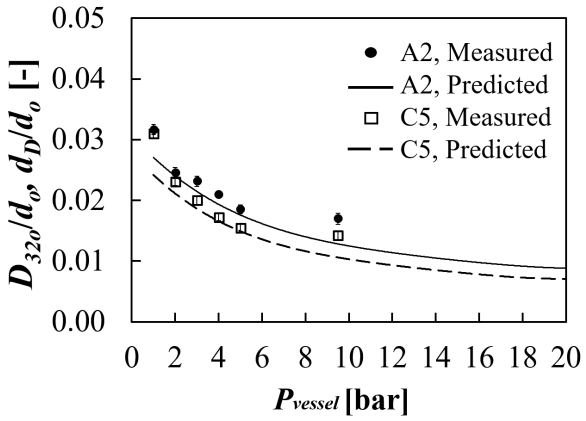

Figure6.16. Comparison of non-dimensionalized measured average drop sizes (D_{32}o/do) and predicted drop size (d_D/d_o) at different ambient pressures for A-2 and C-5 fuels at$\Delta P/P$ = 3%,ΔP_{pilot} = 1.72 bar,T_{fuel} = 332 K, andT_{airbox} = 394 K for z = 25.4 mm.

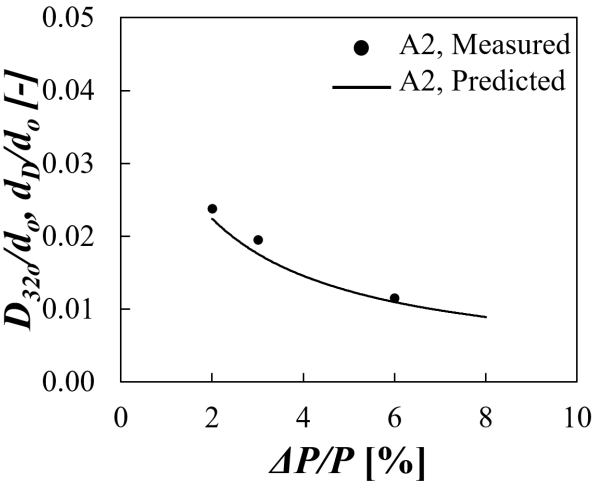

Figure6.17. Comparison between the measured and predicted dimensionless drop sizes at$\Delta P/P$ =2, 3, and 6% and P_{vessel} = 5 bar for A-2 fuel

6.6 Summary

The characteristics of a non-reacting spray, generated by the hybrid pressure-swirl airblast (HPSA) atomizer, were investigated under high ambient pressure conditions for standard and alternative aviation fuels using PDA and simultaneous PLIF and Mie imaging techniques.

A significant reduction in D_{32} was observed with increasing P_{vessel} from 1 bar to 9.5 bar. This is attributed to higher ambient gas density causing a greater gas inertial force on the liquid. This raises the growth rate and wavenumber of disturbance on the liquid and results in smaller droplets. However, the effect of ambient pressure on the drop size diminished with a further increase in ambient pressure. Furthermore, the spray tends to have a monodisperse droplet at higher ambient pressure. The droplet sizes of A-2 fuel were greater than those for C-5 fuel due to the higher viscosity and surface tension of the A-2 fuel. The axial drop velocity was observed to be similar for all ambient pressures, but droplets near the spray edge were observed to slow down with increasing pressure. A greater number of smaller droplets resulted at higher ambient pressure due to higher inertial force of the gas with greater gas density. The PLIF data indicates that these droplets tended to recirculate in the hollow-cone region. The spray cone angle was observed to be independent of ambient pressure at $z = 6$ and 25.4 mm for both A-2 and C-5 fuels. However, the cone angle at $z = 18$mm was observed to increase with increasing ambient pressure due to entrainment of smaller droplets at high ambient pressure.

A phenomenological three-step atomization model, including pressure-swirl spray droplet formation, droplet impingement and film formation, and aerodynamic breakup, was used to calculate the drop size with increasing ambient pressure. Higher ambient gas density caused to increase in the dynamic pressure force on the liquid and raised the growth rate of disturbance on the sheet and ligaments in the model. This resulted in decreasing the diameter and length of ligament formed at the prefilmer tip. However, more experimental work is required to validate the model over a wider range of operating conditions and physical fuel properties.

7. FUTURE WORK

This chapter describes a potential work that can be extended from the previous work.

7.1 Droplet Segmentation using Convolutional Neural Network

Identifying drop size and drop distribution of the spray is a critical task in characterizing the spray. Although the measurement technique can vary depending on applications, typical measurement techniques for measuring the drop sizes and drop distributions in spray applications are phase Doppler anemometery (PDA) and laser diffraction analyzer for their high accuracy and high spatial resolution. However, both techniques are limited to a single pointwise and a line-of-sight measurement, respectively. It will be a trivial and time/resource consuming process to construct a two-dimensional spray field using these techniques. The laser sheet drop sizing technique, such as LIF/Mie signal ratio using Structured Laser Illuminated Planar Imaging (SLIPI), can provide a two-dimensional drop size map of the spray. However, the fundamental of LIF/Mie ratio drop sizing is not always valid due to various factors such as multiple scattering, aromatic/fluorescent dye concentration, and evaporation. Furthermore, it would need an additional set of drop size measurements such as PDA or laser diffraction analyzer to calibrate LIF/Mie signal to drop size.

Building upon the laser sheet spray measurement, image segmentation using an autoencoder neural network can be done using Mie scattering images to detect individual droplets. An autoencoder neural network has been used to reconstruct the desired image from the original compressed image through dimensionality reduction for image denoising, image segmentation, and audio compression. One of the most widely used autoencoder architecture is the UNet, which was primarily developed for medical image segmentation [**ronneberger2015**]. As an example, Figure. 7.1 shows an UNet architecture developed by Ronneberger *et al.* [**ronneberger2015**]. This UNet architecture can be explored for denoising and segmentation to detect the droplets from the Mie scattering images.

The UNet architecture consists of an encoder (contracting path) and a decoder (expansive path), which gives it the u-shaped architecture. The encoder downsamples (left side of the structure) the image keeping only the most prominent features by removing the noise. Each

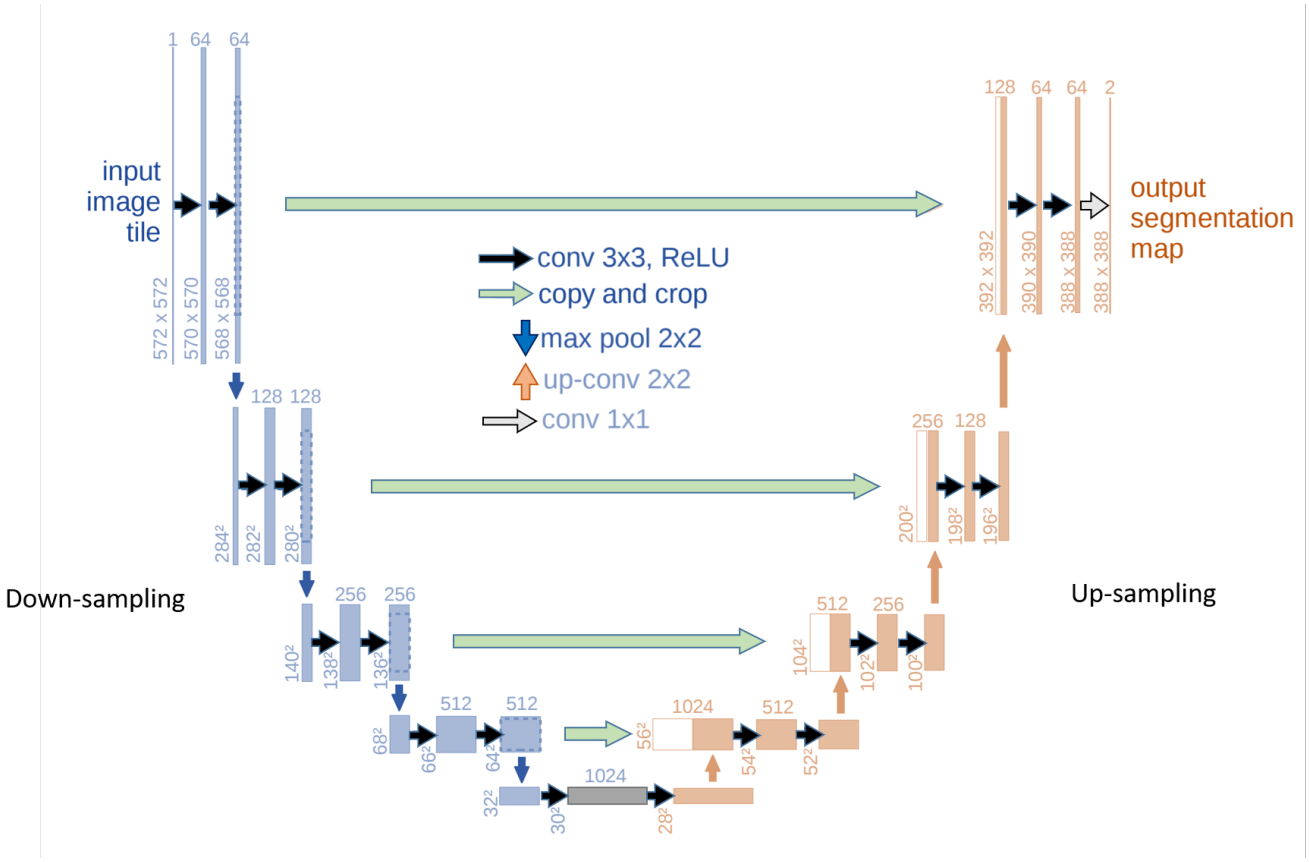

Figure7.1. U-net architecture for 32x32 pixels in the lowest resolution. Each blue box indicates a multi-channel feature map. The number of channels is denoted on top of the box. The x-y-size is provided at the lower left edge of the box. White boxes indicates copied feature maps. The arrows denote the different operations [**ronneberger2015**]

convolution is followed by a recified linear unit (ReLU) and a max pooling operation. The decoder is the inverse operation of the encoder. The decoder upsamples (right side of the structure) the image and reconstructs the input image to get the desired output image. The skip connections (green arrows) between the corresponding layers in the encoder and decoder add the important features that may be removed during the downsampling in the image reconstruction process. The Swish activation function can be used with the encoder and leaky ReLU with the decoder. The loss function can be mean squared error between the original image and the reconstructed output image.

8. SUMMARY AND OUTLOOK

To conclude, sprays generated by a hybrid pressure-swirl airblast (HPSA) atomizer for two standard (A-2 and A-3) and six different alternative aviation fuels (C-1, C-3, C-5, C-6, C-7, and C-8) have been investigated at realistic gas turbine engine conditions such as lean blowout (LBO), engine cold start, and high ambient pressures. Using phase Doppler anemometry, the mean drop sizes, drop size distributions, and drop axial velocities were measured and compared to investigate effect of fuel physical properties and operating conditions on spray. Simultaneous PLIF and Mie scattering images were also used to measure the spray cone angle and discriminate the liquid and vapor phases in the spray. A semi-empirical model for the HPSA atmoizer was developed to predict the drop size. The main results and achievements of this work are enumerated as follows:

- The spray characteristics of Jet-A (A-2) and alternative fuels (C-1, C-5, C-7, and C-8) have been studied at near lean blowout conditions (P_{vessel} = 2.07 bar, T_{fuel} = 322 K, and T_{gas} = 394 K) using a hybrid pressure-swirl airblast (HPSA) atomizer. An increase in the swirler pressure drop resulted in a decrease in mean drop sizes and an increase in axial velocity for both standard and alternative fuels. The effect of the surface tension on the mean drop size was observed to be dominated over the effect of viscosity. The effect of fuel injection pressure was observed to have no significant on the drop size and drop velocity. The comparison of spray full cone angles estimated from high-speed shadowgraph images showed that the effect of fuel injection pressure, pressure drop, and fuel property was minimal.

- The spray characteristics of Jet-A and JP-5 (A-2 and A-3) and an alternative fuel (C-3) were investigated using a HPSA atomizer at engine cold start conditions defined as P_{vessel} = 1.07 bar, T_{fuel} = 239 K, and T_{gas} = 239 K. The effect of swirler pressure drop on the mean drop size and drop velocity was found to be significant, with increasing the pressure drop, resulting in decreased mean drop sizes and increased axial velocities for both the standard and alternative aviation fuels (A-2, A-3, C-3). No definite trend was observed with the viscosity on drop size. Although the surface tension seemed to dominate the

effect of viscosity, its drop size variation was not significant due to such a small difference in surface tension value among fuels.

- The effect of operating conditions (LBO and cold start) was observed to be significant on the mean drop size. Larger mean drop sizes were observed at cold start compared to those at LBO conditions. This is attributed to the combined effects of higher viscosity and surface tension at lower fuel temperature, resulting in a greater restorative force of the droplet and viscous damping effect, and lower ambient pressure at the cold start compared to LBO conditions. The drop velocities near the spray edge for LBO condition was observed to be slightly higher than those for cold start condition. This attributed to the lower gas temperature at cold start condition, resulting the kinetic energy of the gas molecule decreases; thereby less kinetic energy transferred to droplets.

- The effect of ambient pressure on the spray characteristics of Jet-A (A-2) and alternative fuel (C-5) was investigated using PDA and simultaneous PLIF and Mie imaging techniques at near LBO conditions. A significant reduction in mean drop sizes was observed with increasing ambient pressure from 1 bar to 9.5 bar. This is attributed to higher ambient gas density causing a greater inertial force on the liquid sheet and ligament resulting in smaller droplets. However, the effect of ambient pressure on the drop size diminished with a further increase in ambient pressure. Furthermore, the spray tends to have a monodisperse droplet across the radial locations at higher ambient pressure. The A-2 fuel were observed to form larger drop sizes than C-5 fuel due to the higher viscosity and surface tension of the A-2 fuel. The axial drop velocity was observed to be similar for all ambient pressures, but droplets near the spray edge were observed to slow down with increasing pressure. The spray cone angle was observed to be independent of ambient pressure for both A-2 and C-5 fuels at $z = 6$ and 25.4 mm. However, the cone angle at $z = 18$ mm was observed to increase with increasing ambient pressure due to entrainment of smaller droplet at higher ambient pressure.

- A greater number of smaller droplets resulted in higher ambient pressure. The Mie scattering images and PDA data indicated that these droplets tended to recirculate into

the hollow-cone region. These increased smaller droplets led to increased in the number of scattered events. Thus, both PLIF and Mie signals were observed to increase with increasing the ambient pressure. Moreover, the smaller droplets near the spray edge tended to follow the gas flow.

- Laser Sheet Drop Sizing (LSD) technique showed a limitation to estimate the D_{32} map of the spray in this application. The Mie and LIF signals were deviated from the D^2 and D^3 proportionality respectively due to multiple scattering and high aromatic concentration in fuel. Therefore, the ratio of LIF and Mie was not able to represent the ratio of D^3/D^2, which is the Sauter Mean Diameter. Structured Illuminated Laser Planar Imaging (SLIPI) is suggested to surpress the multiple scattering, and seeding fluorescent dye in the liquid is suggested to have a control of dye concentration.

- A semi-empirical model based on phenomenological three-step atomization sub-models was developed, including pressure-swirl spray droplet formation, droplet impingement and film formation, and aerodynamic breakup. The model predicted the drop size as function of ALR, atomizing gas velocity, surface tension, density, and ligament length and diameter within $\pm 15\%$ of error for LBO and cold start conditions and $\pm 20\%$ for high ambient pressure conditions. Furthermore, the model successfully demonstrated the drop size trend with viscosity, surface tension, and ambient pressures.

BIBLIOGRAPHY

[1] Climate Change, ICAO Environment, 2019, www.icao.int/environmental-protection/pages/climate-change.aspx

[2] Garcia, M., "Air Travel Projected To Double In 20 Years, But Protectionism Poses Threat," Forbes Magazine, October 24, 2018. https://www.forbes.com/sites/marisagarcia/2018/10/24/iata-raises-20-year-projections-to-8-2-billion-passengers-warns-against-protectionism/?sh=7a041f6150fb.

[3] Air Transport Bureau (Economic Development), "Effect of Novel Coronavirus (COVID-19) on Civil Aviation: Economic Impact Analysis.", Montreal, Canada, 2021.

[4] Hileman, J.I., and Stratton, R.W., "Alternative Jet Fuel Feasibility", *Transport Policy*, Vol. 34, pp. 52-62, 2014. https://doi.org/10.1016/j.tranpol.2014.02.018

[5] Colket, M., Heyne, J., Rumizen, M., Gupta, M., Edwards, T., Roquemore, W.M., Andac, G., Boehm, R., Lovett, J., Williams, R., Condevaux, J., Turner, D., Rizk, N., Tishkoff, J., Li, C., Moder, J., Friend, D., and Sankaran, V., "Overview of the National Jet Fuels Combustion Program," *AIAA Journal*, Vol. 55, No. 4, April 2017, pp. 1087-1104. doi:10.2514/1.J055361

[6] Lefebvre, A.H., McDonell, V.G., "Atomization and Sprays," *Hemisphere Publishing Corporation*, 2nd Ed., New York, March 2017, pp. 1–178. doi:10.1201/9781315120911

[7] Boyce, M.P., "Gas turbine engineering handbook," Butterworth-Heinemann, 4th ed., 2011

[8] Mansour, A., Benjamin, M., Burke, T., Odar, A., and Savel, B., "Hybrid Atomizing Fuel Nozzle," U.S. Patent 6547163 B1, April 2003. https://patents.google.com/patent/US6547163B1/en

[9] Batarseh, F.Z., Roisman, I.V., Tropea, C., "Characterization of a Spray Generated by an Airblast Atomizer with Prefilmer," *Atomization and Sprays*, Vol. 20, No. 10, November 2010, pp. 887-903. doi:10.1615/AtomizSpr.v20.i10.50

[10] Chin, J.S., Rizk, N.K., Razdan, M.K., "Effect of Inner and Outer Airflow Characteristics on High Liquid Pressure Prefilming Airblast Atomization," *Journal of Propulsion and Power*, Vol. 16, No. 2, March 2000, pp. 297-301. doi:10.2514/2.5568

[11] Ma, R., Dong, B., Yu, Z., Zhang, T., Wang, Y., Li, W., "An Experimental Study on the Spray Characteristics of the Air-Blast Atomizer," *Applied Thermal Engineering*, Vol. 88, September 2015, pp. 149-156. doi:10.1016/j.applthermaleng.2014.11.068

[12] Custer, J.R., Rizk, N.K., "Influence of Design Concept and Liquid Properties on Fuel Injector Performance," *Journal of Propulsion and Power*, Vol. 4, No. 4, July 1988, pp. 378–384. doi:10.2514/3.23077

[13] Hsiang, L.P. and Faeth, G., 1992, January. Secondary drop breakup in the deformation regime. In 30th Aerospace Sciences Meeting and Exhibit, pp. 110. https://doi.org/10.2514/6.1992-110

[14] Rizkalla, A.A., and Lefebvre, A.H., "Influence of Liquid Properties on Airblast Atomizer Spray Characteristics," *Journal of Engineering for Power*, Vol. 97, No. 2, April 1975, pp. 173-177. doi:10.1115/1.3445951

[15] Chrigui, M., Roisman, I.V., Batarseh, F.Z., Sadiki, A., and Tropea, C., "Spray generated by an airblast atomizer under elevated ambient pressures," *Journal of Propulsion and Power*, Vol. 26, No. 6, Nov.-Dec. 2010, pp. 1170-1183. doi:10.2514/1.47833

[16] Zheng, Q.P., Jasuja, A.K., and Lefebvre, A.H., "Structure of airblast sprays under high ambient pressure conditions," *ASME Turbo Expo 1996: Power for Land, Sea*, and Air, Vol. 3, No. 96-GT-131, June. 1996, pp. V003T06A022. doi:10.1115/96-GT-131

[17] Becker, J. and Hassa, C., "Experimental investigation of spatial and temporal aspects of the liquid fuel placement in a swirl cup at elevated pressure," *ASME Turbo Expo 2004: Power for Land, Sea*, and Air, Vol. 1, No. GT2004-53524, June. 14-17, 2004, pp. 351-360. doi:10.1115/GT2004-53524

[18] Corber, A., Rizk, N., Chishty, W.A., "Experimental and Analytical Characterization of Alternative Aviation Fuel Sprays under Realistic Operating Conditions," *GT2018-75574.*, 2018, doi.org/10.1115/GT2018-75574

[19] Chaussonnet, G., Gepperth, S., Holz, S., Koch, R., and Bauer, H., "Influence of the ambient pressure on the liquid accumulation and on the primary spray in prefilming airblast atomization," *Journal of Fluid Mechanics*, 2019.

[20] Jasuja A. K., "Airblast Atomization of Alternative Liquid Petroleum Fuels under High Pressure Conditions," *ASME Journal of Engineering for Power*, Vol.103, No.3, 1981, pp. 514-518, DOI:10.1115/1.3230751

[21] Chin, J.S., Rizk, N.K., Razdan, M.K., "Study on Hybrid Airblast Atomization," *Journal of Propulsion and Power*, Vol. 15, No. 2, March 1999, pp. 241-247. doi:10.2514/2.5418

[22] Tareq, M. M., Dafsari, R. A., Jung, S., Lee, J., "Effect of the Physical Properties of Liquid and ALR on the Spray Characteristics of a Pre-Filming Airblast Nozzle," *International Journal of Multiphase Flow*, Vol. 126, May 2020, 103240. https://doi.org/10.1016/j.ijmultiphaseflow.2020.103240

[23] Edwards, T., Moses, C., Dryer, F., "Evaluation of Combustion Performance of Alternative Aviation Fuels,"AIAA 2010-7155, July 2010. AFRL-RZ-WP-TR-2010-2134 and AFRL-RQ-WP-TR-2013-0223 (limited distribution).

[24] Rizk, N. K., and A. H. Lefebvre. "The influence of liquid film thickness on airblast atomization,"*ASME. J. Eng. Gas Turbines Power*, Vol. 102, No. 3, July 1980, pp. 706-710. https://doi.org/10.1115/1.3230329

[25] Rizk, N. K., and Lefebvre, A. H. (July 1, 1984). "Spray Characteristics of Plain-Jet Airblast Atomizers." *ASME. J. Eng. Gas Turbines Power*, Vol. 106, No. 3, July 1984, pp. 634–638. https://doi.org/10.1115/1.3239617

[26] Lefebvre, A.H., and X.F. Wang., "Mean Drop Sizes from Pressure-Swirl Nozzles," *Journal of Propulsion and Power*, Vol. 3, No. 1, January 1987, pp. 11-18.doi:10.2514/3.22946

[27] Chen, S.K., Lefebvre, A.H., Rollbuhler J., "Factors Influencing the Effective Spray Cone Angle of Pressure-Swirl Atomizers," *Journal of Engineering for Gas Turbines and Power*, Vol. 114, No. 1, January 1992, pp. 97-103.doi:10.1115/1.2906313

[28] Edwards, T., "Reference Jet Fuels for Combustion Testing," AIAA Paper 2017-0146, 2017.doi:10.2514/6.2017-0146

[29] Das Sudhaker, "Fluid Dynamic Study of Hollow Cone Sprays," SAE Technical Paper Series 2018-01-0131, 2008. doi:10.4271/2008-01-0131

[30] Dodge, L. G., and Biaglow, J. A., "Effect of Elevated Temperature and Pressure on Sprays From Simplex Swirl Atomizers." ASME. J. Eng. Gas Turbines Power. January, Vol. 108, No. 1, 1986, pp. 209–215. https://doi.org/10.1115/1.3239873

[31] Senecal, P. K., Schmidt, D. P., Nouar, I., Rutland, C. J., and Reitz, R. D., "Modeling High Speed Viscous Liquid Sheet Atomization," *International Journal of Multiphase Flow*, Vol.25, Issues 6–7, September 1999, pp. 1073-1097. doi.org/10.1016/S0301-9322(99)00057-9

[32] Squire, H.B., "Investigation of the instability of a moving liquid film," *Brit. Journal of Applied Physics*, Vol. 4, No. 6, June 1953. doi.org/10.1088/0508-3443/4/6/302

[33] Dombrowski, N. and Johns, W.R., "The Aerodynamic Instability and Disintegration of Viscous Liquid Sheets," *Chemical Engineering Science*, Vol. 18, No. 3, March 1963, pp. 203-214. doi.org/10.1016/0009-2509(63)85005-8

[34] Reitz, R.D., and Bracco, F.V., "Mechanism of Atomization of a Liquid Jet," *Physics of Fluids* Vol. 25 No. 10, 1983, pp. 1730-1742. doi.org/10.1063/1.863650

[35] Dombrowski, N., Hooper, P.C., "The Effect of Ambient Density on Drop Formation in Sprays ," *Chemical Engineering Science* Vol. 17 No. 4, 1962, pp. 291-305. doi.org/10.1016/0009-2509(62)85008-8

[36] Moon, Y., Kim, D., and Yoon, Y., "Improved Spray Model for Viscous Annular Sheets in a Swirl Injector," *Journal of Propulsion and Power* Vol. 26, No. 2, March-April 2010, pp. 267-279. doi.org/10.2514/1.45010

[37] Dombrowski, N., Hooper, P.C., "The Break-up of Liquid Jets, Zeit schrift fur Angewandte Mathematik und Mechanik," *Journal of Applied Mathematics and Mechanics* Vol. 11, 1931, pp. 136-154. doi.org/10.1002/zamm.19310110207

[38] Naber, J.D., and Reitz, R.D., "Modeling Engine Spray/Wall Impingement," *Journal of Engines*, Vol. 97, No. 6, 1988, pp. 118-140. https://www.jstor.org/stable/44547362

[39] Ibrahim, E.A., and Przekwas, A.J., "Impinging Jets Atomization," *Physics of Fluids A: Fluid Dynamics*, Vol. 3, No. 12, August 1991. doi.org/10.1063/1.857840

[40] Stanton, D.W., and Rutland, C.J., "Modeling Fuel Film Formation and Wall Interaction in Diesel Engines," *SAE International* Vol. 105 No. 3, 1996, pp. 808-824. doi.org/10.4271/960628

[41] Hasson, D., and Peck, R.E., "Thickness Distribution in a Sheet Formed by Impinging Jets," *A.I.Ch.E. Journal* Vol. 10 No. 5, September 1964, pp. 752-754. doi:10.1002/aic.690100533

[42] Sterling, A.M., and Sleicher, C.A., "The Instability of Capillary Jets," *Journal of Fluid Mechanics*, Vol. 68, No. 3, April 1975, pp. 477-495. doi.org/10.1017/S0022112075001772

[43] Sforzo, B., Kastengren, A.L., Matusik, K.E., del Campo, F.G., and Powell, C.F., "X-Ray Phase Contrast Imaging of Liquid Film and Spray Development Inside an Aircraft Engine Swirler," *Journal of Engineering for Gas Turbines and Power*, December 2019, Vol. 141, No. 12, GT2019-1387. doi.org/10.1115/1.4045217

[44] Lefebvre, A.H., "Energy Considerations in Twin Fluid Atomization," *Journal of Engineering for Gas Turbines and Power*, Vol. 114, No. 1, Jan. 1992, pp. 89-96. doi.org/10.1115/1.2906311

[45] Beck, J.E., and Lefebvre, T.R., "Liquid Sheet Disintegration by Impinging Air Streams ," *Atomization and Sprays* Vol. 1 Issue. 2, 1991, pp. 155-170. doi.org/10.1615/AtomizSpr.v1.i2.20

[46] Knoll, K.E., and Sojka, P.E., "Flat-Sheet Twin-Fluid Atomization of High Viscosity Fluids. Part I: Newtonian Liquids," *Atomization and Sprays* Vol. 2 Issue. 1, 1992, pp. 17-36. doi.org/10.1615/AtomizSpr.v2.i1.20

[47] Wang, X.F., and Lefebvre, A.H., "Influence of Fuel Temperature on Atomization Performance of Pressure-Swirl Atomizers," *Journal of Propulsion and Power*, Vol. 4, No. 3, May 1988, pp. 222-227. doi:10.2514/3.23052

[48] Kannaiyan, K., Sadr, R., "Experimental Investigation of Spray Characteristics of Alternative Aviation Fuels," *Energy Conversion and Management*, Vol. 88, December 2014, pp. 1060–1069. doi:10.1016/j.enconman.2014.09.037

[49] Wang, X.F., and Lefebvre, A.H., 1987, "Influence of Ambient Air Pressure on Pressure-Swirl Atomization," *Proceedings of the ASME 1987 International Gas Turbine Conference and Exhibition, 3: Coal, Biomass and Alternative Fuels; Combustion and Fuels; Oil and Gas Applications; Cycle Innovations*. Anaheim, California, USA. May 31–June 4, 1987. V003T06A003. ASME. https://doi.org/10.1115/87-GT-55

[50] Durdina, L., Jedelsky, J., and Jicha, M., "Investigation and Comparison of Spray Characteristics of Pressure-Swirl Atomizers for a Small-Sized Aircraft Turbine Engine", *International Journal of Heat and Mass Transfer*, Vol. 78, November 2014, pp. 892–900. doi:10.1016/j.ijheatmasstransfer.2014.07.066

[51] Corporan, E., Edwards, T., Stouffer, S., Hendershott, T., DeWitt, M., Klingshirn, C., West, Z., Bruening, C., and Striebich, R., "Impacts of Fuel Properties on Combustor Performance, Operability, and Emissions Characteristics," AIAA Paper 2017-0380, 2017. doi:10.2514/6.2017-0380

[52] Esclapez, L., Ma, P.C., Mayhew, E., Xu, R., Stouffer, S., Lee, T., Wang, H., Ihme, M., "Fuel Effects on Lean Blow-out in a Realistic Gas Turbine Combustor," *Combustion and Flame*, Vol. 181, July 2017, pp. 82-99. https://doi.org/10.1016/j.combustflame.2017.02.035

[53] Albrecht, H.E., Borys, M., Damaschke, N., and Tropea, C., "Laser Doppler and phase Doppler measurement techniques," *Springer-Verlag Berlin Heidelberg*, 2003, pp. 169–523. doi.org/10.1007/978-3-662-05165-8

[54] Rodrigues, N.S., Kulkarni, V., Gao, J., Chen, J., and Sojka, P.E., "An Experimental and Theoretical Investigation of Spray Characteristics of Impinging Jets in Impact Wave Regime," *Experiments in Fluids*, Vol. 56, No. 3, February 2015. doi:10.1007/s00348-015-1917-7

[55] Kline, S. J., and McClintock, F. A., "Describing Uncertainties in Single Sample Experiments," *Mechanical Engineering*, Vol. 75, No. 1, 1953, pp. 3–8. https://doi.org/10.1007/s00348-015-1917-7

[56] Mugele, R.A., and Evans, H.D., "Droplet Size Distribution in Sprays", *Industrial and Engineering Chemistry*, Vol. 43, No. 6, pp.1317-1324, 1951, https://doi.org/10.1021/ie50498a023

[57] Edwards, C.F. and Marx, K.D., "Multipoint Statistical Structure of the Ideal Spray. Part I: Fundamental Concepts and the Realization Density," *Atomization and Sprays*, Vol. 5, No. 4 and 5, 1995, pp. 435-455. 10.1615/AtomizSpr.v5.i45.50

[58] Edwards, C.F. and Marx, K.D., "Multipoint Statistical Structure of the Ideal Spray. Part II: Evaluating Steadiness Using the Interparticle Time Distribution," *Atomization and Sprays*, Vol. 5, No. 4 and 5, pp. 457-505, 1995. 10.1615/AtomizSpr.v5.i45.60

[59] Luong, John., "Unsteadiness in Effervescent Sprays," *Atomization and Sprays*, Vol. 9, No. 1, 1999, pp 87-109. doi: 10.1615/AtomizSpr.v9.i1.50

[60] Shin, D., Bokhart, A, J., Rodrigues, N. S., Sojka, P., Gore, J. P., and Lucht, P. R., "Non-Reacting Spray Characteristics for Alternative Aviation Fuels at Near Lean Blowout Conditions," *Journal of Propulsion and Power*, 2019. https://doi.org/10.2514/1.B37712

[61] Hanson, R., K., Seitzman, J., M., and Paul, P., H., "Planar Laser-Fluorescence Imaging of Combustion Gases," *Appl. Phys. B*, Vol.50, 1990, pp. 441-454. https://doi.org/10.1007/BF00408770

[62] Fansler, T.,D., Reuss, D.,L., Sick, V., and Dahms R.,N., "Invited Review: Combustion instability in spray-guided stratified-charge engines: A review", *International Journal of Engine Research*, Vol. 16, No.3, 2015, pp.260-305. doi:10.1177/1468087414565675

[63] Ordain, M., Baranger, P., Ledier, C., Apeloig, J., Grisch, F., 2014, "Fluorescence Spectroscopy of Kerosene Vapour at High Temperatures and Pressures: Potential for Gas Turbines Measurements", *Appl. Phys. B*, Vol. 116, p2014, pp. 729-745, doi:10.1007/s00340-013-5756-z

[64] Suto, M., Wang, X., Shan, J., and Lee, L., C., "Quantitative Photoabsorption and Fluorescence Spectroscopy of Benzene, Naphthalene, and Some Derivatives at 106–295 nm," *J. Quant. Spectrosc. Radiat. Transfer*, Vol. 48, No.1, 1992, pp. 79-89, https://doi.org/10.1016/0022-4073(92)90008-R

[65] Yeh, C.N., Kosaka, H., Kamimoto, T., "A Fluorescence/Scattering Imaging Technique for Instantaneous 2-D Measurements of Particle Size Distribution in a Transient Spray," *Proc. 3rd Congr. on Opt. Part. Sizing*, Yokohama, Japan, 1993, pp. 355 - 361.

[66] Sankar, S. V., Maher, K. E., Robart, D. M., and Bachalo, W. D. ,"Rapid Characterization of Fuel Atomizers Using an Optical Patternator." *ASME. J. Eng. Gas Turbines Power*, Vol.121, No.3, 1999, pp.409–414. https://doi.org/10.1115/1.2818488

[67] LeGal, P, Farrugia, N., Greenhalgh, D. A., "Laser Sheet Dropsizing of Dense Sprays," *Optics Laser Technol*, Vol.31, 1999, pp.75-83. https://doi.org/10.1016/S0030-3992(99)00024-9

[68] Charalampous, G., and Hardalupas, Y., "Method to Reduce Errors of Droplet Sizing based on the Ratio of Fluorescent and Scattered Light Intensities (laser-induced fluorescence/Mie technique)," *OSA Applied Optics*, Vol.50, No.20, 2011, pp. 3622-3637. https://doi.org/10.1364/AO.50.003622

[69] Zaller, M., Locke, R.J. Anderson, R.C., "Comparison of Techniques For Non-Intrusive Fuel Drop Size Measurements in a Subscale Gas Turbine Combustor," *Journal of Visualization*, Vol.2, 2000, pp. 301–308 https://doi.org/10.1007/BF03181446

[70] Domann, R., and Hardalupas, Y., 2001, "A Study of Parameters that Influence the Accuracy of the Planar Droplet Sizing (PDS) Technique," *Particle Particle Systems Characterization*, Vol.18, No.1, 2001, pp. 3-11, https://doi.org/10.1002/1521-4117(200102)18:1<3::AID-PPSC3>3.0.CO;2-%23

[71] Domann, R., and Hardalupas, Y., "Quantitative Measurement of Planar Droplet Sauter Mean Diameter in Sprays using Planar Droplet Sizing," *Particle Particle Systems Characterization*, Vol.20, 2003, pp. 209-218, https://doi.org/10.1002/ppsc.200390027

[72] Berrocal, E., Kristensson, E., Richter, M., Linne, M., Aldén, M., "Application of Structured Illumination for Multiple Scattering Suppression in Planar Laser Imaging of Dense Sprays", *Optics Express*, Vol.16, No.22, 2008, pp. 17870-17881, https://doi.org/10.1364/OE.16.017870

[73] Powell, J.W., Lee, C.F., "An Investigation of Multiple Scattering in a Hollow-Cone Spray", *SAE Paper 2007-01-0648*, 2007, https://doi.org/10.4271/2007-01-0648

[74] Richard Viskup, 2020, "Diesel and Gasoline Engines", IntechOpen, Chap.5. ISBN: 978-1-78985-447-3, DOI: 10.5772/intechopen.75259

[75] Pastor, J.V., Lopez, J.J., Juliá, J.E., Benajes, J.V., "Planar Laser-Induced Fluorescence Fuel Concentration Measurements in Isothermal Diesel Sprays," *Optics Express*, Vol.10, No.7, 2002, pp.309-323

[76] Mishra, Y., N., Kristensson, E., and Berrocal, E., "Reliable LIF/Mie Droplet Sizing in Sprays using Structured Laser Illumination Planar Imaging," *Optical Society of America*, Vol.22, No.4, 2014, pp. 4481-4492, doi:10.1364/OE.22.004480

[77] Mishra, Y., N., Kristensson, E., Koegl, M., Jonsson, J., Zigan, L., and Berrocal, E., "Comparison between Two-Phase and One-Phase SLIPI for Instantaneous Imaging of Transient Sprays," *Exp. Fluids*, Vol.58, No.110, 2017, pp. 1-17 doi 10.1007/s00348-017-2396-9

[78] Kulkarni, A., P., Chaudhari, V., D., Bhadange, S., R., and Deshmukh, D., "Planar Drop-Sizing and Liquid Volume Fraction Measurements of Airblast Spray in Cross-Flow Using SLIPI-based Techniques," *International Journal of Heat and Fluid Flow*, Vol.80, 2019, https://doi.org/10.1016/j.ijheatfluidflow.2019.108501

[79] Ordain, M., Baranger, P., Rossow, B., and Grisch, F., "Fluorescence Spectroscopy of 1,2,4-trimethylbenzene at High Temperatures and Pressures: Application to Temperature Measurements", *Appl. Phys B*, Vol.100, 2010, pp. 945-952, doi:10.1007/s00340-010-3967-0

[80] Shin, D., Rodrigues, N. S., Bokhart, A, J., Sojka, P., Gore, J. P., and Lucht, P. R., "Spray Characteristics of Standard and Alternative Aviation Fuels at Cold Start Conditions," *AIAA Journal*, 2020, submitted

[81] DeCorso, S.M., "Effect of ambient and fuel pressure on spray drop size," *Journal of Engineering for Power*, Vol.82, No.1, 1960, pp. 10-18.

[82] Jermy, M., Greenhalgh, D., "Planar dropsizing by elastic and fluorescence scattering in sprays too dense for phase Doppler measurement," *Appl Phys B*, Vol.71, 2000, pp.703–710. https://doi.org/10.1007/s003400000404

[83] Stojkovic, B., Sick, V., "Evolution and impingement of an automotive fuel spray investigated with simultaneous Mie/LIF techniques," *Appl Phys B*, Vol.73, 2001, pp.75–83. https://doi.org/10.1007/s003400100598

[84] Kannaiyan, K., Banda, M., V., K., Vaidyanathan A., "Planar Sauter Mean Diameter measurements in Liquid centered Swirl Coaxial Injector Using Laser Induced Fluorescence, Mie scattering and Laser Diffraction Techniques," *Acta Astronautica*, Vol.123, 2016, pp. 257-270, 10.1016/j.actaastro.2016.03.011

[85] Andersson, M., Warnberg, J., Hemdal, S., Dahlander, P., 2011, "Evaporation of Gasoline-Like and Ethanol-Based Fuels in Hollow-Cone Sprays Investigated by Planar Laser-Induced Fluorescence and Mie Scattering," *SAE Technical Paper 2011-01-1889*, https://doi.org/10.4271/2011-01-1889.

[86] Linne, M., "Imaging in the Optically Dense Regions of a Spray: A review of Developing Techniques," *Progress in Energy and Combustion Science*, Vol.39, No.5, 2013, pp.403-440. https://doi.org/10.1016/j.pecs.2013.06.001

[87] Zelina, J., Rodrigue, A., "Fuel Injector Characterization using Laser Diagnostics at Atmospheric and Elevated Pressures," *AIAA-98-0148*, 1998, DOI: 10.2514/6.1998-148

[88] Dodge, L. G., and Biaglow, J. A., 1986, "Effect of Elevated Temperature and Pressure on Sprays From Simplex Swirl Atomizers." ASME. J. Eng. Gas Turbines Power. 108(1), pp.209–215. https://doi.org/10.1115/1.3239873

[89] Canny, J., 1986, "A Computational Approach to Edge Detection," in IEEE Transactions on Pattern Analysis and Machine Intelligence, Vol.PAMI-8, No.6, pp.679-698, doi: 10.1109/TPAMI.1986.4767851.

[90] Laufer, G., 1996, "Properties of Electromagnetic Waves. In Introduction to Optics and Lasers in Engineering", Cambridge: Cambridge University Press., pp.87-121. doi:10.1017/CBO9781139174190.006.

[91] Ronneberger, O., Fischer, P. and Brox, T., 2015, October. "U-net: Convolutional networks for biomedical image segmentation.", In International Conference on Medical image computing and computer-assisted intervention (pp. 234-241). Springer, Cham. doi:10.1007/978-3-319-24574-4-28.

VITA

Dongyun (Daniel) Shin was born in Daegu, South Korea. In 2007, he came to the United States as part of an exchange student program and attended high school in Kansas. After the exchange student program was ended, he moved to South Dakota and graduated from O'gorman High School in 2009. Dongyun entered Virginia Tech in Blacksburg, Virginia, and received his Bachelor of Science degree in Aerospace Engineering in May 2015. Dongyun joined the Master's program in Aeronautical and Astronautical Engineering at Purdue University in August 2015. After two years of the Master's program, he started the Ph.D. program in Aeronautical and Astronautical Engineering at Purdue University.